Optical Manipulation Using Planar/Patterned Metallo-dielectric Multilayer Structures

Ling LIN

A thesis presented for the degree of

Doctor of Philosophy

in

Electrical and Electronic Engineering

at the

University of Canterbury

Christchurch, New Zealand

January, 2008

Abstract

Tailoring surface plasmon (SP) resonances using metallic nanostructures for optical manipulation has been widely investigated in recent years; and there are many puzzles yet to be solved in this relatively new area. This thesis covers the study of the interaction of light with SP-supporting planar/patterned metallo-dielectric multilayer structures. Two separate, but closely related subjects were investigated using such structures, which are: SP-assisted optical transmission and optical metamaterials.

The physical mechanisms of the SP-assisted transmission phenomenon were studied using planar/grating and planar/hole-array multilayer structures. Extraordinary light transmission has been demonstrated through experimental work and simulations for both arrangements; and the effects of different structural parameters on the transmission efficiencies of the structures were analyzed systematically. The interplays of the surface plasmon polaritons (SPPs) and localized surface plasmons (LSPs) in the extraordinary optical transmission (EOT) phenomenon were identified.

The potential of the planar/hole-array multilayer structures as optical magnetic metamaterials was evaluated using two independent electromagnetic simulation techniques. The ability of such structures to produce strong magnetic resonances from infrared down to visible side of spectrum was revealed. The methods of tuning the magnetic response of the

structures were suggested.

A novel design of optical metamaterial based on high-order multipolar resonances in a single-layer plasmonic structure was also proposed. Numerical results from two different computation methods indicate that a simultaneously negative permittivity and permeability can be achieved in such a structure.

Acknowledgements

First of all, I would like to thank my supervisor Prof. Richard Blaikie, for his support and professional guidance through out this study. Without his encouragement and enormous amount of patience, this thesis would not have been completed.

I would also like to thank Dr. Roger Reeves and his student Joon Koo (Scott) Choi, for their assistance in the laser lab in the Department of Physics; Dr. Matthew Arnold, who is now in the University of Technology Sydney, for the helpful discussion of different problems related to the simulation work carried out in this thesis.

I must also thank Helen Devereux and Gary Turner, for maintaining the microfabrication laboratory and for sharing their knowledge about the equipments and processing issues; Wei-Lun Chiu, for helping me out with a lot of training in the lab early on.

I would like to acknowledge the financial support from the MacDiarmid Institute for Advanced Materials and Nanotechnology.

For contributions of a less technical nature, I also have to thank Bernice Tyree, Ann Rogerson and Betty Barry, for their friendship and help over the years.

Finally, I would like to express my deepest thanks to my parents for their never-ending love and support.

Contents

List of Figures

List of Tables

§ 1. Introduction

For nearly forty years the semiconductor industry has experienced frenetic growth following Moore's Law, which states that the number of transistors on a silicon integrated circuit (IC) would double every two years due to advances in the engineering capability of device miniaturization [1]. For example, from 1971 to 2007, the average feature sizes of the transistors (length of the silicon channel between the source and drain) on commercially available microprocessors have decreased from 10 μm (Intel 4004) to 65 nm (Intel Core 2 Duo); correspondingly, the clock frequencies have increased from 108 kHz to 2 GHz.

Recently, some technological problems stemming from the device miniaturization, such as the heat production and R-C delay times [2] [3], have given rise to concerns to current electronics technology may hit its top in the near future. While many believe that optics could potentially offer solutions to these problems [4] [5] [6], constructing highly integrated opto-electronic nano-devices is a rather difficult task. This is because the diffraction limit of light [7] has imposed a constraint on the size of the optical devices to about $\lambda/2n$ (λ is the wavelength of light and n is the refractive index of the host medium), resulting in the substantial size mismatch between optical and electronic components.

The diffraction limit of light not only imposes design challenges

in device miniaturization, but also places economic barriers to device manufacturing. A crucial technique in mass production of high-density integrated semiconductor devices is optical lithography, through which mask patterns are transferred to silicon by exposing photosensitive material (photoresist) coated wafers. Since the resolution of an optical system is directly related to the wavelength of the light source, a conventional solution is to use light sources with shorter wavelength to transfer patterns with smaller features. However, as the wavelength becomes shorter, the lithography system also becomes more complex and expensive. For instance, the cost of a 193 nm exposure tool is approximately $12M and the price for a 157 nm exposure tool is expected go up to $20M [8].

The technological and economic challenges currently facing high-tech industry require new technology and materials to be developed in order to overcome these barriers to maintain its frenetic growth pace. Fortunately, the traditional law of diffraction has recently been challenged by a number of researchers. For example, the discovery of extraordinary light transmission through subwavelength metallic apertures showed that nanoscale holes could be effective optical emitters [9]. In their letter to Nature, Ebbesen and coworkers concluded that the exceptional transmission was attributable to excitation of surface plasmons (SPs) on the metal film. This report has attracted a great deal of attention within scientific community and forms a vital part of an active and growing field of research called *Plasmonics*, which refers to surface-plasmon-based subwavelength optics.

SPs arise from the interaction of light with a dielectric/metal interface. Under certain conditions the free electrons near the metal surface can oscillate in resonance with the incident light and induce surface electromagnetic waves on the metal. SP waves have the same frequency as the incident light but

with a much shorter wavelength, which provides the possibility to confine and channel light using metallic subwavelength structures without the constraint of the optical diffraction limit. The field of plasmonics offers several research opportunities which could be used to solve some problems currently facing the semiconductor industry, such as developing nanoscale plasmon based optical interconnects for VLSI circuits, plasmonic circuits with capability of carrying both optical and electronic signals on the same chip, as well as low cost nanolithography systems.

The properties of SPs have been well known for many years [10]; for example, the development of surface plasmon resonance (SPR) sensing technique has been receiving attention since late 1970s [11]. Thanks to the advanced micro/nano fabrication and analysis techniques, the structures of interest for plasmonics – artificially patterned metallic and metallo-dielectric systems – can now be constructed at the nanometre scale, which opens opportunities to tailor the properties of SPs for specific applications. A wide range of plasmon-based nanophotonic devices have been demonstrated to date, including mirrors, beam splitters, lenses and waveguides [12] [13] [14]. Since the optical manipulation is achieved through metallic nanostructures, plasmonic devices also have potential of carrying both electric and optical signals. The promising future of using plasmonic devices to bridge the gap between optical and electronic devices, as well as the prospect of all-plasmonic chips for future integrated circuits, have come into view in many recent review articles [15] [16] [17].

In addition to nanophotonic devices, the potential applications of SPs have also been explored in the areas of optical data storage, near-field microscopy, bio-sensors and light generation [18] [19] [20]. Specifically, great efforts have been devoted to engineering negative-index metamaterials

(NIMs) at optical wavelengths, which was inspired by Pendry's suggestion of perfect imaging using negative refractive index material [21].

Pendry's suggestion has opened up an exciting prospect of achieving deep-subwavelength imaging without the constraint of the diffraction limit, which is particularly appealing for optical nanolithography. Because there are no naturally formed materials that possess negative refractive indices, the opportunity of accessing such materials only lies on so called *metamaterials*, which refer to artificially engineered composites. In such materials, the required properties are obtained from the structural units in addition to the material compositions. Since the first experimental demonstration of double-negative (simultaneously negative permeability and permittivity) metamaterials at microwave wavelengths using bulk split-ring-resonator/wire structures in 2000 [22], several approaches have been considered to construct NIMs, including photonic crystals, transmission lines and plasmonic resonance structures [23]. On account of electromagnetic (EM) properties of the metals and the dimensions of constituent units for optical NIMs, plasmon resonance is considered to be an effective tool for the designs of NIMs at optical frequencies [24].

As described above, the potential of plasmonics in future nanotechnology have been widely recognized within the scientific community in recent years. Nevertheless, while SPs on bulk metals have been studied for many decades, controlling the properties of SPs using metallic nanoparticles/nanostructures is still a rather new field. There are many puzzles yet to be solved in the area of fundamental studies and application development.

The aims of this thesis are to gain understanding of light-SP interactions within metallo-dielectric subwavelength structures, as well as to to explore the potential applications. It contains experimental

and computational studies of surface-plasmon-assisted optical transmission through planar/patterned multilayer structures; and new designs for optical metamaterials, including optical magnetism in planar/patterned plasmonic multilayer system and double-negative optical metamaterials via single-layer plasmonic structures.

The remainder of this thesis is structured as follows. Chapter 2 provides the background for the topics important to this thesis, including: a brief history of SPs, basic physics and common techniques for optical excitation and detection of SPs. Chapter 3 reviews the applications of plasmonics in the field of sensing technology and nano-optical device development; recent research activities in SP-enhanced optical transmission are also included.

Chapter 4 reports the study SP-mediated light transmission through planar/grating multilayer structures, including the experimental procedure, the simulation techniques and the results revealing the important roles of SPs in the extraordinary transmission properties of the structures. Chapter 5 details the optical properties of planar/hole array multilayer structures and gives an in depth analysis of the physical mechanisms of SP-assisted transmission through planar metal films.

Chapter 6 provides the background for the study of metamaterials, including the homogenization techniques and electromagnetic parameter retrieval methods. The current status in developing optical metamaterials are outlined. Chapter 7 presents the numerical study of two new designs of metamaterials operating in optical region: magnetic metamaterials using planar/patterned multilayer structure and double-negative metamaterials using single-layer plasmonic structures.

Finally, Chapter 8 concludes the main points of this thesis and outlines the directions for future work.

Aspects of the work described in this dissertation have been published and presented as follows:

Articles

- L. Lin, R. J. Blaikie and R. J. Reeves, "Surface-plasmon-enhanced optical transmission through planar metal films", Journal of Electromagnetic Waves and Applications, **19**, 1721-1728 (2005).

- L. Lin, R. J. Reeves and R. J. Blaikie, "Surface-plasmon-enhanced light transmission through planar metallic films", Physical Review B, **74**, 155407 (2006).

- L. Lin and R. J. Blaikie, "Negative permeability using planar-patterned metallic multilayer structures", Journal of Optics A: Pure and Applied Optics, **9**, 385-388 (2007).

- J. C. Sharpe, J. S. Mitchell, L. Lin, N. Sedoglavich and R. J. Blaikie, "Gold nanohole array substrates as immunobiosensors", accepted for publication in Analytical Chemistry (2008).

Conference presentations (**presenter in bold**)

- **L. Lin**, R. J. Reeves and R. J. Blaikie, "Transmission enhancement of planar metal films through resonant coupling of surface plasmons", Third International Conference on Advanced Materials and Nanotechnology (AMN-3), 11-16 February 2007, Wellington, New Zealand. Oral presentation.

- **L. Lin** and R. J. Blaikie, "Negative permeability in planar/patterned metallic multilayer structures", Third International Conference on Advanced Materials and Nanotechnology (AMN-3), 11-16 February 2007, Wellington, New Zealand. Poster presentation.

- **L. Lin** and R. J. Blaikie, "Negative permeability using planar patterned metal multilayers", First European Topical Conference on Nanophotonics and Metamaterials (NANOMETA2007), 8-11 January 2007. 8 -11 January 2007, Tirol, Austria. Poster Presentation.

- **R. J. Blaikie**, L. Lin and R. J. Reeves, "Enhanced optical transmission through planar metallic films via excitation of surface plasmons", International Conference on Nanoscience and Nanotechnology (ICONN2006), 3-7 July 2006, Brisbane, Australia. Oral presentation.

- **L. Lin**, R. J. Blaikie and R. J. Reeves, "Plasmon-enhanced optical transmission through planar metal films", Progress in Electromagnetics Research Symposium (PIER2005), 22-26 August 2005, Hangzhou, China. Oral presentation.

- **L. Lin**, S. J. Drake, R. J. Reeves and R. J. Blaikie, "Control of the optical transmission of metal films via excitation of surface plasmons", Second International Conference on Advanced Materials and Nanotechnology (AMN-2), , 6-11 February 2005, Queenstown, New Zealand. Poster presentation

§ 2. Background

2.1 Introduction

In physics and chemistry, the word "plasma" typically refers to an *ionized gas* with equal amounts of positive and negative charges. In view of that, free electrons and positive ion cores within a metal can also be considered as a plasma. In the presence of external excitation the density of the electrons may fluctuate locally; subsequently, the local charge neutrality could be restored by the Coulomb force existing between electrons and positive ion cores. The continuous process of sustaining local charge equilibrium results in a longitudinal charge density oscillation in the metal, which is referred to as a *plasma oscillation*(or plasma wave). The oscillation frequency ω_p can be derived as [10]:

$$\omega_p = \sqrt{\frac{4\pi n_e q_e^2}{m}} \qquad \text{in Gaussian units} \ , \tag{2.1}$$

or

$$\omega_p = \sqrt{\frac{n_e q_e^2}{m\varepsilon_o}} \qquad \text{in SI units} \ , \tag{2.2}$$

where n_e is the density of electrons, q_e is the charge of electron, m_e is the effective mass of the electron and ε_o is the permittivity of free space. We will use SI units throughout the remainder of this thesis.

The "plasmon" is the quasiparticle resulting from the quantization of plasma oscillations, with an energy of $E = \hbar\omega_p$. Surface plasmons (SPs) refer to those plasmons that are confined to surfaces of the metals. Depending on the excitation conditions, SPs can be classified into two main categories [25]: *surface plasmon polaritons* (SPPs) and *localized surface plasmons* (LSPs). The former often exist on planar metal surfaces and the latter generally can be found on metallic nanoparticles/nanovoids, as shown in Fig. 2.1 below.

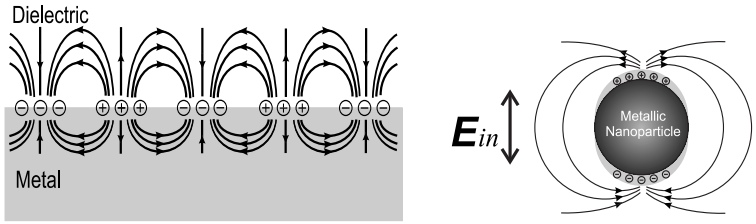

Figure 2.1: Electric field lines of: surface plasmon polaritons on a plane metal surface (left) and localized surface plasmons on a metallic nanoparticle surface (right).

This chapter provides background information relating to SPs, which are the fundamentals of the two main topics studied in this thesis, namely SP-assisted optical transmission and optical left-handed metamaterials. Both of these studies are based on the excitation of SP resonances, although their focuses are somewhat different.

2.2 A Brief History of Surface Plasmons

The history of using metallic nanoparticles to modify the optical properties of a material can be traced back to the time of Rome, when colloidal copper, gold and silver were used as decorative pigments for glasswares. A famous example is Lycurgus cup (4th century AD). The cup shows different colours when viewed in reflected and in transmitted light, as

seen in Fig. 2.2. Recent investigation has revealed that the unusual colour change is caused by the excitation of LSPs on the small amount of gold (Au) and silver (Ag) nanoparticles embedded in the glass.

Figure 2.2: The Lycurgus Cup: it appears opaque green when viewed in reflected light (left) and turns glowing red color when light is transmitted through it (right). The unusual optical properties are caused by the tiny amount of colloidal gold and silver embedded in the glass.

However, it was not until the beginning of the twentieth century when the scientific studies in SPs started out through the investigation of particle-light scattering and surface electromagnetic (EM) waves on conductors. In 1908, Mie developed a mathematical description of light scattering by spherical particles based on Maxwell's equations [26], which has now been extensively used to calculate plasmon resonance frequency of metallic nanoparticles. Around the same time, Zenneck [27] and Sommerfeld [28] theoretically revealed the existence of surface EM waves at the boundary of one lossy and one loss-free medium at radio frequencies.

In 1941, Fano [29] proposed that the anomalous intensity drop in the spectral of light reflected from metallic gratings reported by Wood in 1902 [30] – commonly known as Wood's anomalies – were related to the coupling of surface EM waves and light.

The concept of plasma oscillation and the term "plasmon" were introduced by Pines in 1950s through the studies of electrons' energy losses when scattered by a thick metallic foil [31] [32]. The existence of plasmons near metal surface was later discovered by Ritchie [33] and Powell [34] in the investigations of electron energy losses in a thin metal film.

The connection between light and SPs was uncovered in late 1960s. Teng and Stern [35] constructed a SP dispersion curve of aluminium (Al) by observing the reflection dips of an Al coated grating and the emission peaks through electron bombardment of same grating in 1967. The following year Ritchie *et al.* revealed that Wood's anomalies were related to the optical excitation of SP resonances on the grating surface. About the same time, methods of optical excitation of SPs via attenuated total reflection were presented by Otto [36] and by Kretschmann and Raether [37], which provided researchers practical tools for understanding the properties of SPs. Two years later, links between SPs and optical properties of metallic nanoparticles were revealed by Kreibig *et al.* [38] through the experimental studies of optical colloid extinction of Ag and Au. These fundamental studies later led to a series of successful developments of SP device applications in between early 1980s to early 1990s, including: surface-enhanced Raman spectroscopy [39], surface plasmon microscopy [40] and surface plasmon resonance sensors [11].

Most recently, SPs have received considerable attention for their potential in optical manipulation at the nanoscale. In 1998, Ebbesen *et al.* reported the observation of extraordinary light transmission through thin metallic films perforated with sub-wavelength hole arrays and suggested that the unusual phenomenon was related to excitation of SPs on the metal films [9]. In 2000 Pendry proposed "perfect lens" concept and suggested the link between the focusing action of a thin metallic film and the existence of well-defined surface

plasmons [21]. These works have sparked enormous interest in rediscovering properties as well as potentials of SPs. A detailed review of the recent activities relating to SPs will be presented in Chapter 3 and Chapter 6.

2.3 Basic Physics of Surface Plasmons

2.3.1 Interaction of Electromagnetic Waves with Metals

In this section we relate the optical properties of metals to the interaction of EM waves with metals, which can be derived from Maxwell's equations at the macro scale, or be described by a Drude model at an atomistic scale.

2.3.1.1 Wave Propagation in Metals

The propagation of the EM waves in a material medium can be described by Maxwell's equations, which are (SI units):

$$\nabla \times \mathbf{H} = \frac{\partial \mathbf{D}}{\partial t} + \mathbf{j}_f \tag{2.3}$$

$$\nabla \times \mathbf{E} = -\frac{\partial \mathbf{B}}{\partial t} \tag{2.4}$$

$$\nabla \cdot \mathbf{D} = \rho_f \tag{2.5}$$

$$\nabla \cdot \mathbf{B} = 0 \tag{2.6}$$

where $\mathbf{E}, \mathbf{D}, \mathbf{H}$ and $\mathbf{B}$ are electric field density, electric flux density (electric displacement), magnetic field density and (magnetic induction) and magnetic flux density, respectively.

Equations (2.3) to (2.6) describe the fields due to free current density $\mathbf{j}_f$ and free charge density ρ_f. In order to determine the field vectors inside a medium, the material equations that describe the behaviour of the medium in

the given fields (also called *constitutive equations*) are necessary. For metals these equations are:

$$\mathbf{D} = \varepsilon\mathbf{E} \tag{2.7}$$

$$\mathbf{B} = \mu\mathbf{H} \tag{2.8}$$

$$\mathbf{j} = \sigma\mathbf{E} \tag{2.9}$$

where $\varepsilon = \varepsilon_r\varepsilon_o$ and $\mu = \mu_r\mu_o$ with ε_o and μ_o being the permittivity and the permeability of free space, respectively; ε_r is the relatively permittivity including the effects of both vacuum and metal core polarization; μ_r is the relatively permeability of the material; and σ is the conductivity of the material.

Combining Equations (2.3) and (2.4) with material Equations (2.7) to (2.9) we have a *differential wave equation* for the **E**-field in the metal:

$$\nabla^2\mathbf{E} = \varepsilon\varepsilon_o\mu\mu_o\frac{\partial^2\mathbf{E}}{\partial t^2} + \mu\mu_o\sigma\frac{\partial\mathbf{E}}{\partial t}\,. \tag{2.10}$$

A solution for Equation (2.10) has the form

$$\mathbf{E}(\mathbf{r},t) = \mathbf{E}_o e^{i(\mathbf{k}\cdot\mathbf{r}-\omega t)} \tag{2.11}$$

where $\mathbf{k}$ is called the propagation vector of the waves and $\mathbf{k} = [k_x, k_y, k_z]$; $\mathbf{r}$ is the position vector, $\mathbf{r} = [x, y, z]$.

Substituting Equation (2.11) into Equation (2.10) and using $\mu_r = 1$ for non-magnetic metals at optical frequencies, the propagation constant $k = |\mathbf{k}|$ of the wave in the metal can be expressed as:

$$k^2(\omega) = \varepsilon_o\mu_o\omega^2\left(\varepsilon_r(\omega) + i\frac{\sigma(\omega)}{\varepsilon_o\omega}\right). \tag{2.12}$$

The bracketed term is the effective dielectric constant of the metal, which includes the contribution from both bound electrons and conduction

electrons. However, it is common to assume that the valency electrons and the corresponding ions are tightly bound, consequently, they have no considerable contribution to the polarization of the metal (i.e., metal core polarization due to an incident EM wave is zero). Therefore, the effective dielectric constant of the metal is often expressed as:

$$\varepsilon_{eff} = 1 + i\frac{\sigma(\omega)}{\varepsilon_o \omega} \tag{2.13}$$

The propagation constant in Equation (2.12) can also be expressed as:

$$k^2 = (k' + ik'')^2 = \frac{\omega^2}{c^2}(n + i\kappa)^2 \tag{2.14}$$

where k' represents the real part of k (it describes how the waves propagate in the metal); k'' is the imaginary part of k (it tells how the waves attenuate while propagating in the metal); $c = 1/(\varepsilon_o \mu_o)$ is the speed of light in free space; and $(n + i\kappa)$ is the *complex refractive index* of the material.

The time averaged field intensity in the metal follows the relation $I \propto \langle |\mathbf{E}(\mathbf{r}, \mathbf{t})|^2 \rangle = |\mathbf{E}_o|^2 e^{-2k''|\mathbf{r}|} = |\mathbf{E}_o|^2 e^{-\alpha|\mathbf{r}|}$, where $\alpha = 2k''$ is the *absorption coefficient* and the quantity $1/\alpha$ is known as the *skin depth* or *penetration depth* of the metal which is the propagation distance at which field intensity drops by a factor of $1/e$. The skin depth for metal is usually a very small number. For instance, the skin depth of Ag at $\lambda = 188nm, 548nm$ and $1215nm$ are $12.3nm$, $12.2nm$ and $11.0nm$, respectively[1].

2.3.1.2 Drude Model

The Drude model describes the response of free electrons in a metal to the incident electric fields at the atomistic scale; it was initially developed by P. Drude in 1900, based on the results of classical mechanics and EM theory

[1] Optical constants of Ag are taken from [41]

at that time [7]. The model treats free moving electrons in the metals as classical particles whose motion obeys Newton's Second Law ($F = ma$). In addition to the driving force from the incident E-field, they endure a drag force due to collisions with other particles (electrons and ions). With this in mind, the model gives the conductivity of the metal due to an oscillating electric field $E(t) = E_o e^{-i\omega t}$, which is:

$$\sigma(\omega) = \frac{n_e q_e^2}{m_e} \frac{1}{(1/\tau - i\omega)} = \frac{\sigma_o}{1 - i\omega\tau} \,, \tag{2.15}$$

where τ is called the *relaxation time* which corresponds to average time between collisions, and $\sigma_o = (n_e q_e^2 \tau)/m_e$.

Correspondingly, Equation (2.13) can be rearranged in terms of plasma frequency of the metal, that is:

$$\varepsilon_{eff}(\omega) = 1 - \frac{\omega_p^2}{\omega^2 + i\Gamma\omega} \,, \tag{2.16}$$

where $\Gamma = 1/\tau$ is called the damping rate (or scattering frequency) of the electrons.

Equation (2.16) is well-known as Drude model for a good metal, which sufficiently models the optical properties of metals at frequencies up to the visible region of the EM spectrum. Clearly, the key parameters describing the optical properties of a solid metal are ω_p and τ. For many metals $\omega_p \gg \omega \gg \Gamma$ in the optical region. Therefore, at the frequencies below the plasma frequency for metals ε_{eff} is complex and often written as $\varepsilon = \varepsilon' + i\varepsilon''$ with $\varepsilon' < 0$, $\varepsilon'' > 0$ and $|\varepsilon'| \gg \varepsilon''$. At frequencies above the plasma frequency ε' becomes positive and metals appear to be transparent at these frequencies.

2.3.2 Surface Plasmon Polaritons (SPPs) on Planar Interfaces

SPs are collective charge density oscillations existing on dielectric/metal interfaces, which arise from the interaction of light with free electrons near a metal surface. This section provides the theoretical descriptions of properties of SPs excited on the continuous metal surface(s) – also known as SPPs.

2.3.2.1 Dispersion Relations of SPPs at the Interface of Metal-dielectric Half-space

To understand the phenomenon of SPP resonance, it is instructive to examine the EM-waves at the interface of a metal-dielectric half-space. First we consider TM polarized light incident on a planar interface of two media whose dielectric constants are ε_1 and ε_2 respectively, as illustrated in Fig. 2.3. Assuming the interface plane is at $z = 0$, the fields in two media can be described as:

$$\mathbf{E}_1 = (E_{x_1}, 0, E_{z_1}) e^{i(k_{x1}x + k_{z1}z - \omega t)} \tag{2.17}$$

$$\mathbf{H}_1 = (0, H_{y1}, 0) e^{i(k_{x1}x + k_{z1}z - \omega t)} \tag{2.18}$$

$$\mathbf{E}_2 = (E_{x2}, 0, E_{z2}) e^{i(k_{x2}x - k_{z2}z - \omega t)} \tag{2.19}$$

$$\mathbf{H}_2 = (0, H_{y2}, 0) e^{i(k_{x2}x - k_{z2}z - \omega t)} \tag{2.20}$$

Solving Maxwell's equations with appropriate boundary conditions leads to the implicit dispersion relation for EM waves existing at the interface, which is

$$\frac{k_{z1}}{\varepsilon_1} + \frac{k_{z2}}{\varepsilon_2} = 0\,. \tag{2.21}$$

For EM waves to be localized to the interface, both k_{z1} and k_{z2} must be positive imaginary numbers, which follows that ε_1 and ε_2 must have opposite

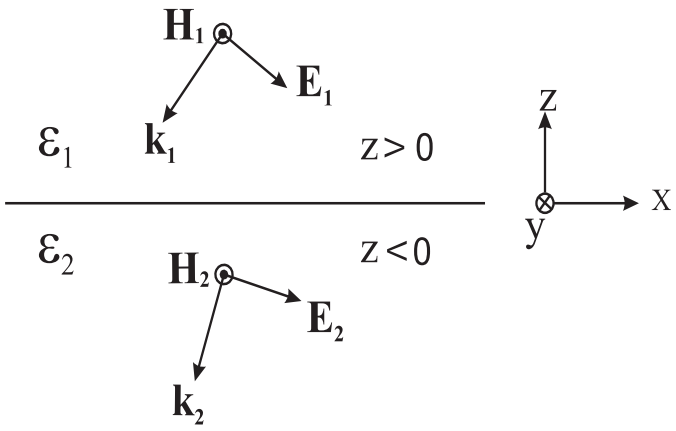

Figure 2.3: Scheme of the interface between two media.

signs.

Combining Equation (2.21) with the relation

$$\varepsilon_i \left(\frac{\omega}{c}\right)^2 = k_x^2 + k_{zi}^2 \quad (i = 1, 2), \tag{2.22}$$

the dispersion relation for surface EM waves at the interface can be expressed as:

$$k_x = \frac{\omega}{c}\sqrt{\frac{\varepsilon_1 \varepsilon_2}{\varepsilon_1 + \varepsilon_2}} \quad , \tag{2.23}$$

which indicates that in addition to the requirement of $\varepsilon_1\varepsilon_2 < 0$ for EM waves existing at the interface, $\varepsilon_1 + \varepsilon_2 < 0$ is essential for waves to propagate along the interface (x-direction), i.e., the real part of k_x is positive. At optical frequencies these two conditions can be fulfilled simultaneously if one medium is a dielectric and the other one is a metal. In the literature, surface EM waves that satisfying above descriptions are often termed as *surface plasmon polaritons* (SPPs) to manifest their plasma oscillation and EM wave propagation hybrid nature.

Assuming $\varepsilon_1 > 0$ and $\varepsilon_2 = \varepsilon_2' + i\varepsilon_2''$ with $\varepsilon_2' < 0$ and $|\varepsilon_2'| > \varepsilon_1$, the real

and imaginary parts of k_x can be expressed as [10]

$$\{k_x\}_{Re} = \frac{\omega}{c}\sqrt{\frac{\varepsilon_1\varepsilon_2'}{\varepsilon_1+\varepsilon_2'}} \tag{2.24}$$

and

$$\{k_x\}_{Im} = \frac{\omega}{c}\sqrt{\left(\frac{\varepsilon_1\varepsilon_2'}{\varepsilon_1+\varepsilon_2'}\right)^3}\frac{\varepsilon_2''}{2(\varepsilon_2')^2}\,. \tag{2.25}$$

Equation (2.24) is generally referred to as the explicit dispersion relation of the SPPs, in which $\{k_x\}_{Re}$ is often replaced by the notation k_{sp}. Since $\varepsilon_1 < |\varepsilon_1+\varepsilon_2'| < |\varepsilon_2'|$, the SPP dispersion curve is situated below the dispersion curve of light in the dielectric medium, as illustrated in Fig. 2.4. This shows that the in-plane wavevector of the SPPs is always larger than that of the light at same frequency, therefore light-SPPs interaction cannot occur spontaneously on a flat metal surface due to the fact that the energy and momentum conservation cannot be satisfied simultaneously in such system.

Equation (2.24) also implies that the wavevector k_{zi} ($i = 1,\ 2$) are pure imaginary as $k_{sp} > \frac{\omega}{c}$, which indicates that SPP waves are evanescent waves whose field intensity peaks at the interface ($z = 0$) and decreases exponentially away from the interface. Owing to the Ohmic loss of the metal (ε_2''), the field intensity also attenuates exponentially while SPs propagate along the interface ($x-$direction). The $1/e$ intensity decay length along the x-direction, which is known as the *propagation length* of the SPPs, is given by $L = (2\{k_x\}_{Im})^{-1}$. At an Ag/air interface this is about 22 μm at $\lambda = 514$ nm and 500 μm at $\lambda = 1060$ nm [10].

The E-field component E_{zi} (i=1,2) at the interface can also be obtained by solving Maxwell's equations with appropriate boundary conditions, which leads to

$$\frac{E_{z1}}{E_{z2}} = \frac{\varepsilon_2}{\varepsilon_1}\,. \tag{2.26}$$

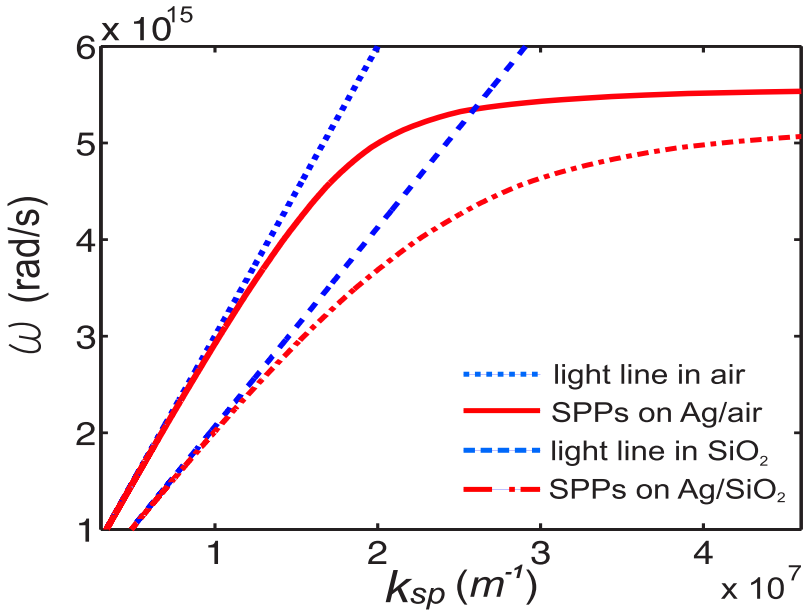

Figure 2.4: Dispersion relations of light line in air (dotted line) and in SiO_2 (dashed line), and that of surface plasmon polaritons on Ag/air interface (solid line) and on Ag/SiO_2 interface (dash-dot line). Optical constants of Ag are taken from [41].

This indicates that within two different media, both amplitude and phase of SPPs can be different at the interface. Since the dielectric constant of the metal is generally greater than that of the dielectric, the amplitude of the SPP field at the dielectric side of the interface is usually larger than that at the metal side of the interface. The *penetration depth* of the SPPs, which refers to $1/e$ intensity decay length in the direction normal to the interface (z-direction), is given by $z_i = (|k_{zi}|)^{-1}$, is also different in the two media. For example, at $\lambda = 600$ nm the penetration depth of the SPPs at an Ag/air interface is 24 nm in Ag and 390 nm in air.

It is also worth noting that for a very large k_{sp}, the group velocity and phase velocity of SPP waves both approach zero. In this case, the waves resemble electrostatic surface waves, that is, a non-propagating fluctuation

of the electron plasma near the metal surface; and the frequency of this collective oscillation can be express as:

$$\omega_{sp} = \frac{\omega_p}{\sqrt{\varepsilon_d + 1}} \,. \tag{2.27}$$

Recently, this particular subclass of SPPs have been extensively used in super-resolution planar lenses [21] [42] [43].

Finally, we note that for TE polarized light, the fields in two media in Fig. 2.3 becomes:

$$\mathbf{E}_1 = (0, E_{y1}, 0)e^{i(k_{x1}x + k_{z1}z - \omega t)} \tag{2.28}$$

$$\mathbf{H}_1 = (H_{x_1}, 0, H_{z_1})e^{i(k_{x1}x + k_{z1}z - \omega t)} \tag{2.29}$$

$$\mathbf{E}_2 = (0, E_{y2}, 0)e^{i(k_{x2}x - k_{z2}z - \omega t)} \tag{2.30}$$

$$\mathbf{H}_2 = (H_{x2}, 0, H_{z2})e^{i(k_{x2}x - k_{z2}z - \omega t)} \tag{2.31}$$

Solving Maxwell's equations with appropriate boundary conditions leads to

$$k_{z1} + k_{z2} = 0 \,, \tag{2.32}$$

which implies that k_{z1} and k_{z2} can not be simultaneously positive, i.e., not localized surface EM waves can be excited under TE polarized incident light.

2.3.2.2 Dispersion Relations of SPPs on a Thin Metal Film

Figure 2.5 illustrates a system consisting of a thin metal film (ε_m) sandwiched between two dielectric media (ε_1 and ε_2). In such system, both surfaces of the metal film can support SPP modes.

If there are considerable differences between ε_1 and ε_2, the dispersion relations of the SPPs on each interfaces simply follow Equation (2.24). However, if ε_1 and ε_2 have similar values, SPP waves of the same frequency on the two interfaces of the metal film will interact with each other, resulting

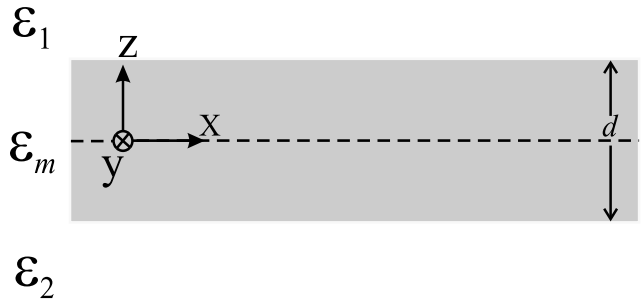

Figure 2.5: A metal film (ε_m) of thickness d sandwiched between two dielectric media (ε_1 and ε_2). The center of the metal film situates at the plane $z = 0$.

in a pair of degenerate SPPs modes [44] [45] with film-thickness-dependent frequency separation. The dispersion relations of these two modes are [10]:

$$\omega^+ : \quad \varepsilon_m k_{zd} + \varepsilon_d k_{zm} \tanh\left[\frac{k_{zm} d}{2i}\right] = 0 \tag{2.33}$$

$$\omega^- : \quad \varepsilon_m k_{zd} + \varepsilon_d k_{zm} \coth\left[\frac{k_{zm} d}{2i}\right] = 0\,, \tag{2.34}$$

where $\varepsilon_d = \varepsilon_1 = \varepsilon_2$; and k_{zm} and k_{zd} are wavevectors in the metal and the dielectric with direction normal to the interface, respectively. Clearly, the dispersion relations of these SPPs modes are not only related to the dielectric constants of metal and the adjacent dielectrics, but also affected by the metal film thickness, as illustrated in Fig. 2.6.

The surface charge distribution of the high frequency mode (ω^+) is symmetric to the plane $z = 0$, and the surface charge distribution of the low frequency mode (ω^-) is asymmetric to the plane $z = 0$, as shown in Fig. 2.7. These imply that the electric field lines for ω^+ mode are essentially parallel to the surfaces of the metal film while those of ω^- are predominantly normal to the surfaces. Since the Ohmic loss (internal damping) is proportional to the intensity of the E-field inside the metal, the ω^+ mode suffers less attenuation than the ω^- mode while propagating along the metal surfaces. Therefore, ω^+

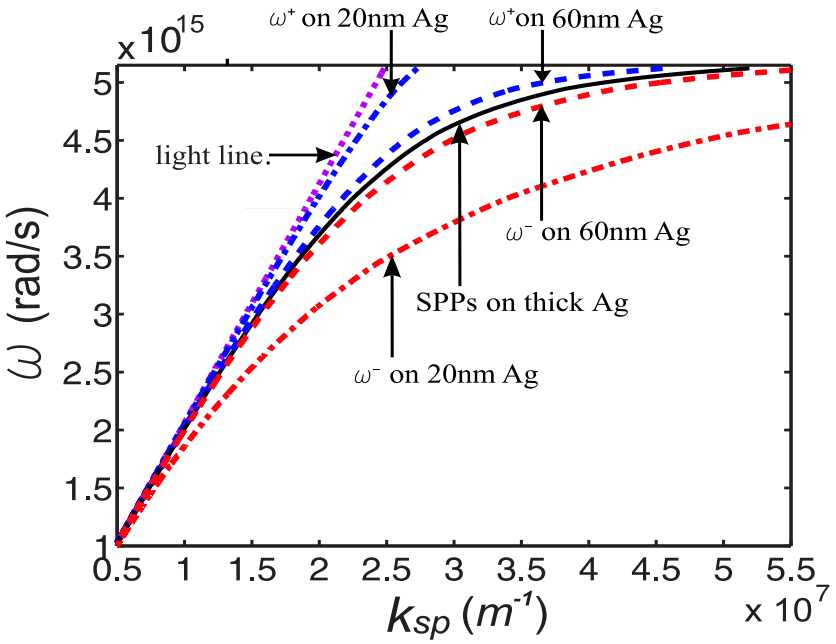

Figure 2.6: Dispersion relation of a thin Ag film surrounded by SiO_2 on both sides. SPP modes on two Ag/SiO_2 interfaces interact with each other and split into a high frequency mode (ω^+) and a low frequency mode (ω^-). The frequencies of these two modes are related to the thickness of the metal film.

and ω^- modes are often called *long range surface plasmon polariton* (LRSPP) and *short range surface plasmon polariton* (SRSPP), respectively.

Furthermore, because the **H**-field of the ω^+ mode exhibits a phase reversal inside the metal film (i.e., the field distribution is asymmetric to the plane $z = 0$), this mode is also referred to as *asymmetric mode* in the literature; in opposition, the ω^- mode maintains the phase of the **H**-field across the metal film (i.e., the field distribution is symmetric to the plane $z = 0$), hence it is termed as *symmetric mode*.

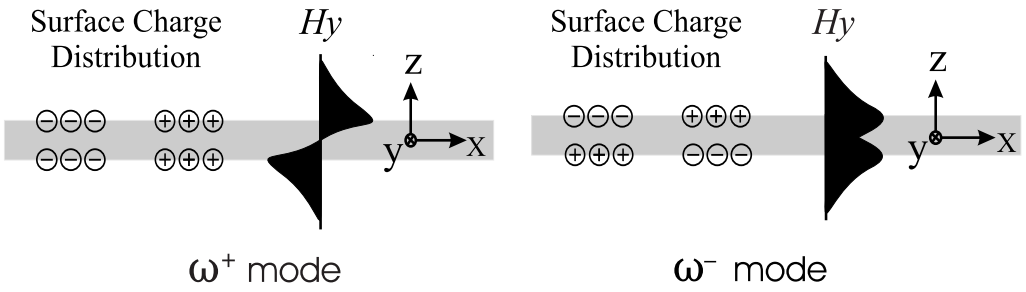

Figure 2.7: Surface charge distribution and **H**-field distribution of the high frequency SPP mode (ω^+) and the low frequency SPP mode (ω^-) on a thin metal film.

2.3.3 Localized Surface Plasmons (LSPs) on Bounded Geometries

Localized surface plasmons (LSPs) arise from collective oscillation of free electrons in metallic nanoparticles and metallic nanostructures. LSPs are also called EM surface shape resonances, particle plasmons, gap plasmons, etc. [19]. As opposed to propagating SPPs, LSPs are non-propagating modes that are confined to bounded geometries.

Mie [26] was the first to quantitatively describe the EM response of nanoparticles. By applying Maxwell's equations with appropriate boundary conditions, he obtained the solutions of the multipole oscillations (dipole, quadrupole, etc.) for the extinction and scattering cross section of spherical particles. He then interpreted the color of stained glass using those results by assuming that the dielectric constants of bulk metals could also be applied to small metal spheres.

For a particle with dimensions much smaller than the wavelength of the incident light in the surrounding medium, a quasistatic analysis is commonly used to describe the plasmon resonance on the metallic nanoparticle, which assumes that the incident EM field is constant over the particle and only the

dipole absorption contributes to the extinction of the particle. This approach gives the particle polarizability α of the metallic nanoparticle as [46]

$$\alpha = \frac{4}{3}\pi V \frac{\varepsilon_m - \varepsilon_d}{\varepsilon_d + L_i(\varepsilon_m - \varepsilon_d)} \qquad (\sum_{i=1}^{3} L_i = 1)\,, \tag{2.35}$$

where V is the volume of the particle; ε_m and ε_d are the dielectric constants of metal and the surrounding medium, respectively; and L_i is the depolarization factor that links to the particle dimensions along the three coordinate axes: for a sphere $L_i = 1/3$.

Equation (2.35) indicates that resonance (excitation of a surface mode) can occur at the frequencies where the denominator of α varnishes, i.e.,

$$\frac{\varepsilon_d}{\varepsilon_m} = -\frac{1 - L_i}{L_i}\,. \tag{2.36}$$

Clearly, besides the influence of the dielectric constants of the metallic particle and the surrounding medium, the characteristics of the resonance (strength, linewidth, etc.) also depend on the size and shape of the nanoparticle. Fig. 2.8 shows the effects of particle size on the optical properties of spherical Au nanoparticles of sizes ranging from 30 nm to 90 nm.

As the size of the particle increases, the incident light cannot polarize the particle homogeneously and the retardation effects produce a gradient of the EM field, which results in the higher order (quadrupole and higher) resonances becoming more dominant in the spectral response of the particle. These effects will shift the plasmon resonance (absorption maxima) to longer wavelengths. In general, the spectral position of the LSPs ω_l can be approximated via [25]:

$$\omega_l = \omega_p \sqrt{\frac{l}{\varepsilon_d(l+1) + l}} \qquad l = 1, 2, 3 \ldots\,, \tag{2.37}$$

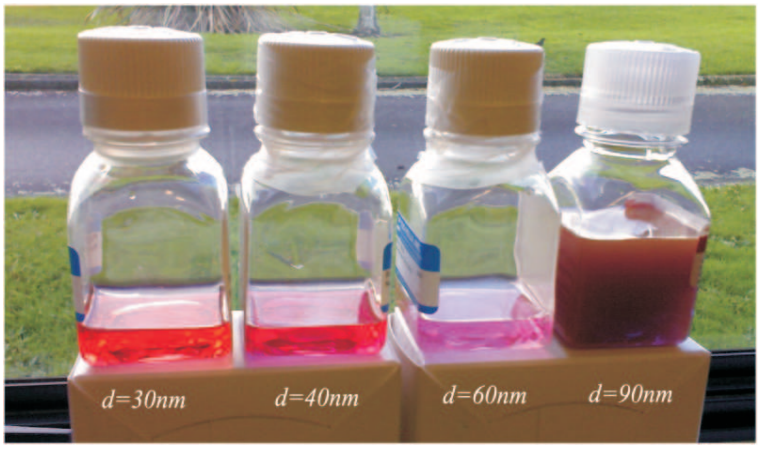

Figure 2.8: Spherical Au nanoparticles with diameters from 30 nm to 90 nm show different shades of red colors (courtesy of J. Sharpe, HortResearch, New Zealand).

where l is related to the order of the resonances. For small particles with dipole-active excitation, the value of l is 1. For a very large sphere, $l \to \infty$ and ω_l approaches the value of $\omega_p/\sqrt{\varepsilon_d + 1}$, which is the same as the non-propagating SPPs in Equation (2.27).

In addition to metallic nanoparticles, LSPs can also be excited on voids of various topologies. In this case, the LSP frequencies of a void in a bulk metal can be estimated through the LSP frequencies of a metallic particle of the same shape via relation [25]

$$\omega_{particle}^2 + \omega_{void}^2 = \omega_p^2. \tag{2.38}$$

Equations (2.35), (2.36) and (2.37) are valid for estimating the EM-responses of a single particle or system with low concentration of nanoparticles, as they are based on the assumption of non-interaction between particles. For closely-spaced nanoparticles, the effect of the interactions between the LSPs on neighboring particles can cause the shift of resonance frequencies [47].

2.4 Optical Excitation and Detection of Surface Plasmons

Just like any other processes in the physical world, light-SP coupling processes during the optical excitation and detection of SPs must obey the laws of conservation of energy and momentum. As discussed in the previous section, the formulation of the dispersion relation of free propagating light and that of surface bound SPs are somewhat different. Therefore, in order to excite or detect SPs optically, techniques to achieve light-SP coupling are usually required.

2.4.1 Optical Excitation of Surface Plasmons

The dispersion relations of SPPs on a planar metal/dielectric interface given by Equation (2.24) imply that at a given frequency, the in-plane wavevector of the SPP is always larger than that of the incident light. This means in general SPPs and light do not interact with each other because the energy and/or momentum mismatches. Therefore, it is not possible to excite SPPs on a flat metal surface by just illuminating it, nor can SPPs spontaneously decay into photons in such system.

There are several methods to couple light and SPPs, including attenuated total reflection (ATR) [36] [37], grating or surface roughness coupling [10] and end-fire coupling [48] [49].

The ATR method is also known as *prism coupling*; it employs an optically dense medium (e.g., prism) in the vicinity of the planar metal surface to generate an evanescent optical field near the metal via total internal reflection. This evanescent optical field increases the wavevector of the light in the direction parallel to the metal surface to match the wavevector of the

SPPs, resulting in SPP excitation on the planar metal surface. If the SPPs are excited on the interface of a dielectric medium with dielectric constant ε_d and a metal with dielectric constant $\varepsilon_m = \varepsilon'_m + i\varepsilon''_m$, the condition for light-SPP coupling becomes

$$k_x = \frac{\omega}{c}\sqrt{\varepsilon_p}\sin\phi = k_{sp} = \frac{\omega}{c}\sqrt{\frac{\varepsilon_d \varepsilon'_m}{\varepsilon_d + \varepsilon'_m}}\,, \tag{2.39}$$

where k_x is the vector of light in the direction parallel to the metal/dielectric interface; ϕ is the angle of incident of the light inside the prism; ε_p is the dielectric constant of prism and $\varepsilon_p > \varepsilon_d$.

Figure 2.9 below illustrates two ATR based arrangements: the Otto configuration and the Kretschmann-Raether configuration. These schemes have been extensively used for studying the dispersion relation of SPPs and for measuring the dielectric constant of metals since the late 1960s. The occurrence of light and SPP coupling is captured by monitoring the spectral reflectance, using light of different wavelengths at a fixed angle of incidence or vice versa. A distinct, sharp dip appears in the reflection spectrum where light is coupled to SPPs. Close to 100% coupling efficiency can be achieved in these systems.

On the other hand, grating or surface roughness coupling methods utilize diffracting elements to provide additional transverse momentum to the photons for light-SPP interaction, such as shown in Fig. 2.10. In this case, the following dispersion relation is satisfied:

$$k_x = \frac{\omega}{c}\sqrt{\varepsilon_d}\sin\theta + \Delta k_x = k_{sp} = \frac{\omega}{c}\sqrt{\frac{\varepsilon_d \varepsilon'_m}{\varepsilon_d + \varepsilon'_m}}\,, \tag{2.40}$$

where θ is the incident angle of the light; and Δk_x represents the contribution to the in-plane wavevector due to diffracting elements. For grating coupling,

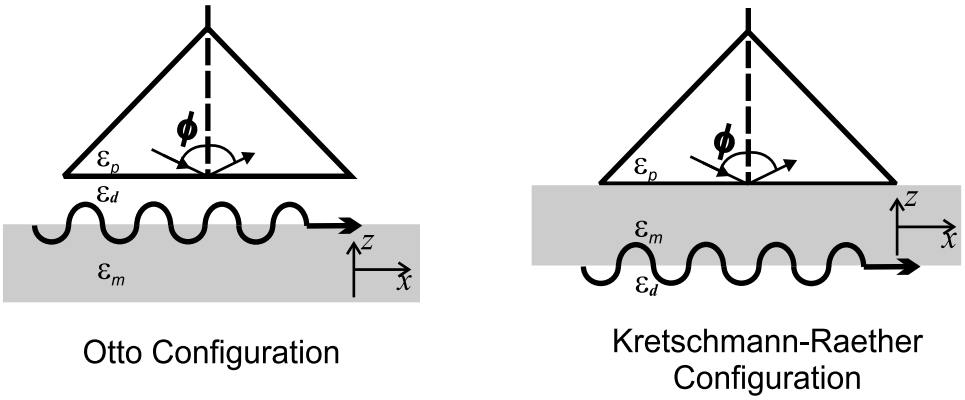

Figure 2.9: Two ATR based arrangements. In Otto configuration the evanescent optical field couples with the SPPs on the inner metal surface; in Kretschmann-Raether configuration, the evanescent optical field couples with the SPPs on the outer metal surface. Here ε_p, ε_m and ε_d refer to prism, metal and air.

Δk_x is the grating vector, which is defined as

$$k_g = m\frac{2\pi}{P} \qquad (m = \pm 1, \pm 2, \pm 3, \dots), \tag{2.41}$$

where m is the diffraction order and P is the grating period. For surface roughness coupling, Δk_x is the roughness Fourier spectrum of the metal/dielectric interface.

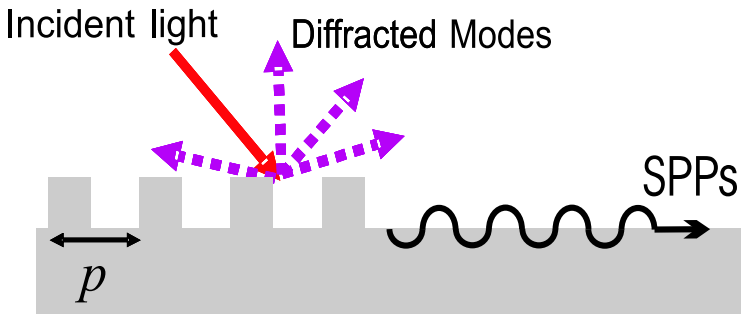

Figure 2.10: A grating coupling configuration for optical excitation of SPPs.

In addition, corrugated metal surfaces were used together with the ATR method (Otto configuration) to decouple SPPs to free propagating light

in the early studies of SPPs [10]. Such systems generally consist of a prism, a photoresist grating prepared on the hypotenuse face of the prism and a thin metal film deposited on top of the grating surface. Recently, grating coupling has been extensively used in SP based applications due to its desirable compact arrangement. Thanks to the advanced micro/nano fabrication techniques, the periodic structures used for light-SPs coupling are no longer limited to the corrugated metal films. A wide variety of structures have been proposed to achieve light-SP interaction, such as metal films with subwavelength hole arrays [9], single apertures surrounded by periodic textures [50], metallic gratings with subwavelength slots [51] and planar/patterned multilayer systems [52] [53]. In this thesis, the grating coupling method was employed to achieve light-SPPs coupling.

The prism coupling and the grating coupling are both based on matching the in-plane wavevector component of the incident light to that of the SPPs. Conversely, the end-fire coupling method excites SPPs along a metal/dielectric interface by focusing light onto the end face of the metal-dielectric system that is normal to the interface [48], as illustrated in Fig. 2.11. The operation is based on overlapping the profile of the incident beam and the SPP field distribution on the end-face of the system, and the maximum SPP generation efficiency occurs when the width of the incident beam equals the penetration depth of SPPs at $x = 0$ plane. This scheme is considered to be an effective method to excite SPPs in SPP waveguides [54] [55] [49] [56].

It should be emphasized that, as opposed to the SPPs, optical excitation of LSPs does not require any special arrangement. As indicated by Equations (2.35) and (2.36), the momentum mismatch between SPPs and light does not exist at LSP resonances. Therefore, LSPs can be resonantly excited by light

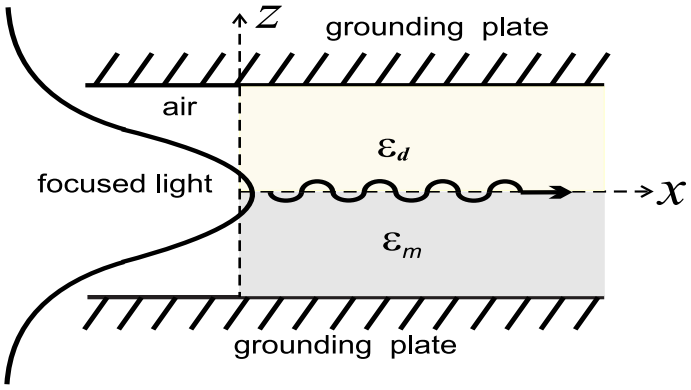

Figure 2.11: Arrangement for optical excitation of SPPs by end-fire coupling.

with appropriate polarization and wavelength, irrespective of the wavevector of incident light; they also can decay to freely propagating light naturally.

2.4.2 Surface Plasmons Detection Techniques

When an incident light is coupled to SPPs on a metal/dielectric interface, the energy of the light is transferred to the SPP waves. If there is no back-converting mechanism presented in the system, the energy carried by the photons is trapped in the metal. Consequently, the intensity of light reflected from the metal surface will go through a minimum when the coupling occurs. This phenomenon is frequently used to determine the occurrence of SPP resonance on smooth metal surfaces [10]. Conversely, extinction spectra are often used for the recognition of LSP excitation. The event of light-LSP resonance is identified from the appearance of an extinction maximum in the spectrum.

While far-field spectral measurements are useful to identify the occurrence of SP excitation, they provide very limited information about SP field profiles. To obtain these, several far-field and near-field microscopic techniques have been developed for SP imaging. Far-field microscopy is

mainly used for imaging SPP propagation. In this scheme the mapping of the SPP field is achieved by utilizing either physical (e.g., surface corrugation on metal film) or chemical (e.g., fluorescence molecules) convertors to transfer evanescent SPP fields into propagating optical fields, and subsequently capturing them in conventional optical microscopes [57].

Far-field microscopy provides a fast and relatively simple method for imaging SPP propagation. However, due to the use of conventional microscopes, the resolution of this technique suffers from diffraction limits. Therefore, near-field microscopy is required for mapping SP field distributions in complex nanostructures. The tool of choice is the so-called photon scanning tunnelling microscope (PSTM) [58], which is a near-field scanning optical microscope (NSOM) operating in the collective mode. A schematic view of a PSTM set up is shown in Fig. 2.12. The operation principle behind PSTM for mapping SP fields is as follows. A sharp tip at the end of an optical fibre serves as a near-field probe. When the tip is placed in an optical near field, a small amount of this near field, proportional to the field intensity at the position of the tip, is collected by the tip and converted into a waveguide mode which travels to the photodetector at the other end of the fibre. By driving the tip along a meandering path at a given height (usually less than one wavelength) above a plasmonic structure and recording the detected intensity at each point, a near-field optical image of the SPs can be constructed pixel by pixel.

PSTM has led to a breakthrough in SP studies since light-SP interaction can be investigated directly on the surface. SP propagation on planar films [59] and along nanoparticle arrays [60], scattering from rough surfaces [61], as well as the interference pattern [62] have been visualized. Fig. 2.13 illustrates a PSTM image of an intensity profile of a SPP field excited on a thin Ag film

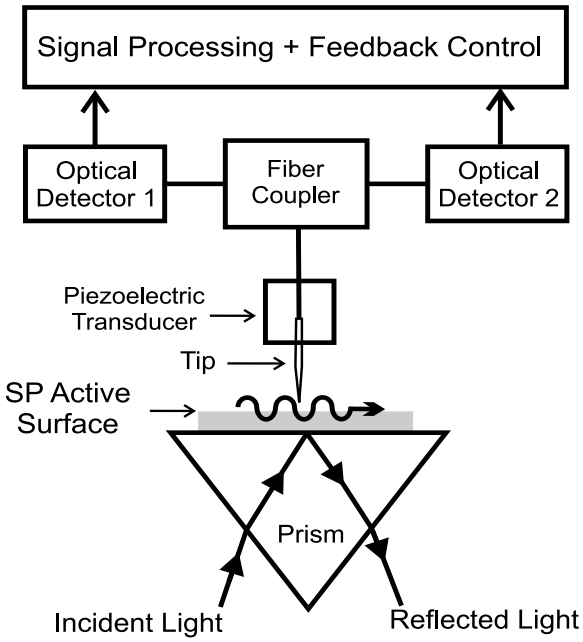

Figure 2.12: Schematic view of PSTM set up.

by Kretschmann-Raether configuration [59].

2.5 Summary

SPs are surface bound EM waves existing on a metal/dielectric interface; they can be localized (LSPs) or delocalized (SPPs) in nature, depending on the geometries of the structures on which they are excited. Their dispersion relations imply that it generally requires a special technique to achieve light-SPP coupling, whereas light-LSP coupling can occur spontaneously at the appropriate wavelengths. The commonly used techniques for the detection of the SP excitation include: spectral reflection or extinction measurements, far-field and near-field microscopies. The former has been widely used for the detection of SP excitation; the latter has been extensively employed to study SP-field distribution in plasmonic structures in recent years.

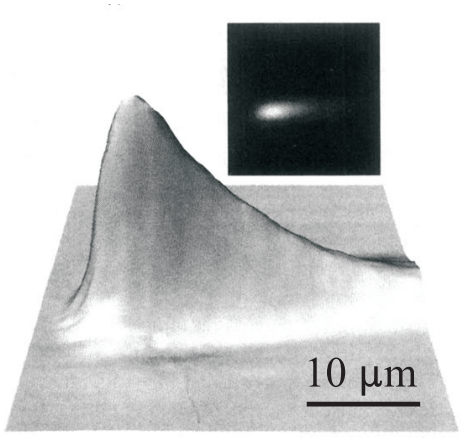

Figure 2.13: PSTM image of a SPP field on a 53-nm-thick planar Ag film surface [59]. SPP excitation is via Kretschmann-Raether configuration. Inset: 2-D version of image.

§ 3. Plasmonic Applications and Recent Research Activities

Following the fundamental studies of light-metal interaction in the early days (late 1950s to late 1960s), SPs have been extensively explored in thin film characterization, chemical sensing and biodetection since late 1970s. In recent years interest in SPs has expended from sensing technology to a wide range of fields, including subwavelength optics, nanophotonics, information storage, nanolithography, light generation and engineering left-handed metamaterials at optical wavelengths, etc. The reformed interest was stimulated by the recent progress in electromagnetic simulations, micro/nanofabrication and characterization techniques, which provide the necessary tools to revive and exploit remarkable properties of SPs in the domains of both fundamental physics and application development. The dynamic growth of the field of plasmonics is clearly reflected in the fact that since 1990 the annual number of publications on SPs has doubled every five years [63].

3.1 Surface Plasmon Resonance Based Sensors

A great deal of work in SP applications has been done in the exploitation of surface plasmon resonance (SPR) sensing for physical [64], chemical [65] and biological detection [66]. The simplest form of SPR sensing is based on reflectivity measurement, which was pioneered by Nylander and co-workers in the early 1980s for gas detection and biosensing [67] [68]. In recent years SPR sensing has become a leading technology for affinity-based biosensing, owing to its label-free, noninvasive real-time analysis nature. At present about 50% of all publications on SPs involve the use of plasmons for biodetection [63], covering fields as diverse as molecular engineering, cell biology, proteomics, clinical diagnosis, drug discovery and environmental monitoring [69].

The working principle behind the SPR sensing technique is that the SPP's resonance conditions, such as wavelength and penetration depth, are highly sensitive to the immediate environment of the metal/dielectric interface, as indicated in Equations (2.24) and (2.25). A SPR sensing system generally involves four elemental modules: an optical system comprising a light source and an optical detector; a flow system for sample delivery; a sensor surface formed by a SPP-active metal film (normally 50 $\sim$ 100-nm-thick Au or Ag); and an electronic system for data processing. All these elements vary depending on the intended application.

Figure 3.1 shows the operation of a SPR device for biosensing, in which the Kretschmann-Raether configuration is used for SPP generation. The sensor chip is a glass slide coated with a Au film, on which the specific protein binding molecules (e.g., antibody) are immobilized to form the transducer surface. The glass slide is optically coupled to the prism through an index-

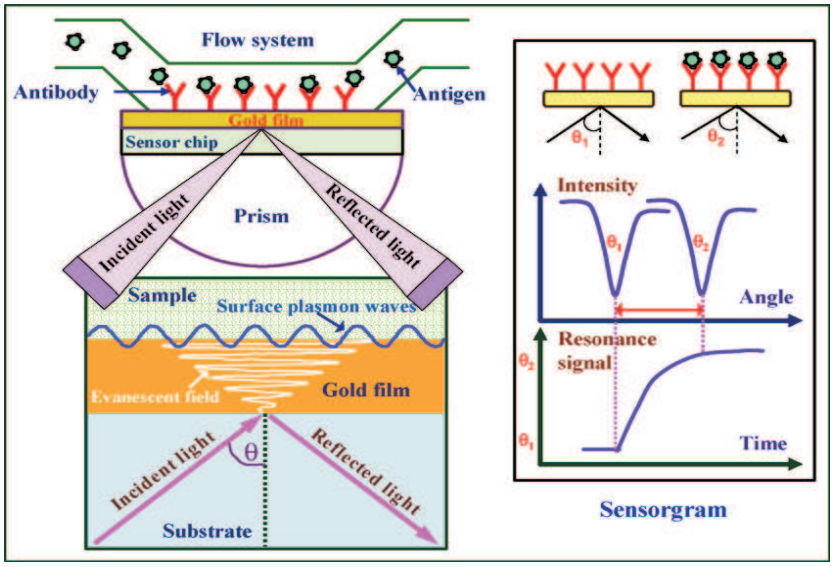

Figure 3.1: A scheme of the principle and operation of SPR biosensing using Kretschmann-Raether configuration [69].

matching fluid with top sensor surface interconnects to the flow system. The excitation of SPPs on the Au surface is monitored by the occurrence of a reflectivity minimum against the angle of incidence through a detector. When the analyte (e.g. antigen) in solution passes through the flow system, these molecules can be bound to the antibody on the Au surface and subsequently alter the local dielectric properties of the thin overlayer that is in contact with the Au film. The binding process is observed as shifts of resonance angle in real time and recorded in a sensorgram. Such a system can yield information including the active concentration of analyte, binding strength of analyte for antibody (affinity), as well as the on and off rates between analyte and antibody (kinetics).

Subsequent to the prism-coupler-based SPR sensor, grating-coupler-based system [70] and optical-waveguide-based systems [71] [72] have also been introduced. However, the Kretschmann-Raether configuration is still the most widely used geometry in SPR sensors [11]. The scheme has been

successfully developed into commercial sensing instruments by BIAcore since the early 1990s [73]. Currently there are several manufacturers offering a wide variety of commercial SPR biosensors [74], which has made it possible for potential users to choose the appropriate system according to the specific requirements, such as sensitivity, selectivity, speed, portability and price.

The conventional SPR sensors predominantly apply continuous metallic films for SPP generation. Recently, there has been an increasing interest in utilizing metallic nanostructures as the sensing platform, such as metal film with periodic nanohole/slit arrays [75] [76] [77] , metallic nanoparticle arrays [78], single nanoparticles [79] and single nanometric holes [80]. These nanostructured systems mostly rely on the excitation of a localized surface plasmon resonance (LSPR). As shown in Fig. 3.2, they operate on a similar principle as the conventional SPR sensors: biochemical interactions near nano metallic structures change the dielectric constants of the medium in contact with metal, which in turn shifts LSPR resonance wavelengths.

There are several important advantages of using nanostructured systems when compared to the conventional reflection-based SPR sensors. First, they can operate on transmission or scattering modes, which is suitable for the development of simple, lightweight, low-cost equipment. Second, the sensing surface has much smaller pixel size (20 to 50 times smaller than the conventional SPR sensors), this is particularly attractive for realizing massively parallel, array-based, high throughput sensing systems. Third, the geometries (e.g. size and shape) of the nanostructures can be adapted to the composition of the sample to achieve signal optimization, which in turn dramatically reduces the required sample volume for achieving a measurable response. For instance, it has been predicted that single-nanoparticle LSPR could approach single-molecule limit of detection for large biomolecules [79].

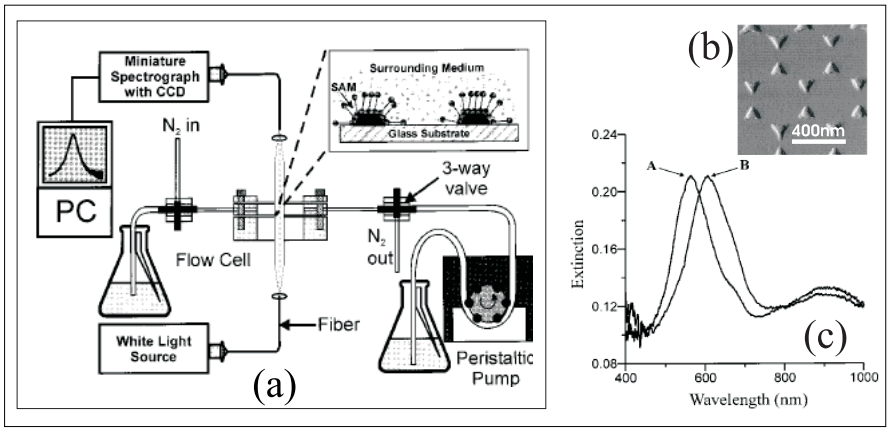

Figure 3.2: (a) A scheme of the operation of LSPR sensing configuration that operates on the transmission mode. The inset shows nanoparticles modified with a functionalized self-assembled monolayer (SAM) in a surrounding medium, either solvent, buffer or gas (controlled by the flow cell). (b) A tapping mode AFM image of Ag nanoparticle array on glass substrate. (c) UV-visible extinction spectra of Ag nanoparticle arrays on glass in a N_2 environment, in which curve A is before chemical modification of nanoparticles and curve B is after modification of nanoparticles with 1-Hexadecanethiol [78].

It should be noted that while the above discussion is focused on SPR and LSPR sensor developments, the applications of surface plasmons in the field of optical sensing technology are not limited to these. In fact, for over thirty years SPs have also been extensively used as signal amplification tools in various surface-enhanced spectroscopic measurements (Raman, luminescence, phosphorescence and fluorescence) for substances identification [81] [82] [83], and this still remains a center of interest in SP-based detection [84] [85] [86]. Moreover, a recent trend in SP-based sensing is the development of high-resolution microscopy and measurement [87]. Nevertheless, these are beyond the scope of the purpose of this thesis.

3.2 Surface-plasmon-based Two-dimensional Optics

Recent resurgence of interest in SPs is not only limited to sensing technology. SPs have also attracted increasing attention as useful tools for the construction of deep subwavelength optical and photonic devices.

It is well known that the spatial confinement of free propagating waves is limited to about $\lambda_o/2n$, that is, about half of the wavelength in the medium. This so-called "diffraction limit" of light is the primary factor that limits the minimum sizes of optical elements in conventional far-field optics and has imposed a major challenge in the development of highly integrated optical devices. The origin of the diffraction limit lies in the three-dimensional nature of the free propagating waves, i.e., k_x, k_y, k_z of the wavevector $\mathbf{k}$ of these waves are all real. Since $|\mathbf{k}|^2 = k_x^2 + k_y^2 + k_z^2$, there is an upper limit on $k_i (i = x, y, z)$ such that $k_i \leqq |\mathbf{k}|$. According to the uncertainty relation of Fourier transforms, this spatial frequency upper limit leads directly to the lower limit in the variation of the wave in real space as $d_i \geqq \lambda_o/2n$.

However, if one (or more than one) component(s) of $\mathbf{k}$ become purely imaginary (e.g., an evanescent wave), then $k_i > |\mathbf{k}|$ can be achieved. This thus provides a means to conquer the diffraction limit. Depending on the number of real components in $\mathbf{k}$, EM waves can be defined as 3-D (three real components in $\mathbf{k}$), 2-D (two real, one pure imaginary components in $\mathbf{k}$), 1-D (one real, two pure imaginary components in $\mathbf{k}$) and 0-D (no real components in $\mathbf{k}$) waves [88]. In this sense, SPPs propagating along planar metal surfaces or metallic nanowires surfaces can be classified as a 2-D or 1-D waves, respectively; and LSPs confined on the metallic nanoparticles or nanovoids can be considered as 0-D waves. Clearly, while 3-D waves suffer

from conventional diffraction limits, 2-, 1-, and 0-D waves have the ability to provide one-, two-, and three-dimensional field confinements in real space without such constraints.

3.2.1 Surface Plasmon Waveguides

Interest in exploiting SPs for opto-electronic device applications is happening at a time when continuous miniaturization of integrated electronic circuits is approaching fundamental limitations. For example, ever since the semiconductor industry entered the sub-100 nm technology nodes, there has been growing concerns over the issues associated with electronic interconnects [3] [5], such as signal delay and heat generation. While conventional fibre-optic interconnects offer speed-of-light propagation, large band-width and low power consumption, the dimensions of these dielectric components are generally at the microscale. This has severely limited their applications in nanoscale integrated electronics circuits.

In contrast to the free propagating light, SPs can be sustained and guided by nanoscale metallic structures without the constraint of the diffraction limits. In 1997 Takahara and co-workers first proposed the use of metallic nanowires to guide 1-D optical beams with nanometer diameter [88]. They suggested that in visible and near-infrared ranges the negative dielectric constants of metal removes the constraints of conventional dielectric waveguides:

$$\begin{aligned} 0 < \varepsilon_{clad} < \varepsilon_{core} \\ \beta, k_x, k_y, \kappa_x, \kappa_y \leq \omega\sqrt{\varepsilon_{core}\mu_o} \end{aligned} \tag{3.1}$$

where ε_{clad} and ε_{core} are the dielectric constants of the core and cladding; β is the wavevector component along the propagation direction (z-direction);

k_x and k_y are the transverse components of the wavevector inside the core and κ_x and κ_y are those in the cladding. As k_x and k_y become imaginary in metallic nanowires, the beam diameter is free from the limitation of the wavelength. Simulation [88] reveals that for the lowest order TM mode β increases as the core radius decreases and no transmission cut off in the core size.

The concept of nanoscale 1-D metallic waveguides has motivated many new researches in the field of plasmonics. However, currently realizing such structures still presents an engineering challenge. On the other hand, various 2-D SPP waveguides (waveguides of 2-D SPP waves) have been experimentally demonstrated in recent years, including: metallic stripes [55] [57] [89] [16] and wedges [90] [91] (insulator-metal-insulator configuration), metallic gaps [92] [93] and grooves [56] (metal-insulator-metal configuration), etc. Moreover, some complex SPP waveguiding elements based on the principle of straight waveguides, such as S-bent waveguides, four-port coupler, Y-splitter and coupler have also been reported [94].

Figure 3.3 illustrates light transport through SPP waveguides [16]. The device used for SPP waveguiding is shown in Fig. 3.3a; it consists of an array of 50-nm-thick varying width Au stripes attached to a large Au area, from which optical waves are converted to SPPs and launched onto Au stripes (2-D SPP waveguides) via a prism coupler. Photon scanning tunnelling microscope(PSTM) images of SPPs excited at $\lambda = 780$ nm and propagating along 3.0 μm, 1.5 μm, and 0.5 μm wide Au stripes are shown in Fig. 3.3b, 3.3c and 3.3d, respectively. It is clear that the propagation distance of SPPs decreases with decreasing stripe width. The losses are mainly due to the intrinsic resistance of the metal leading to resistive heating and wave decay. The losses of stripe waveguides embedded in symmetric environments are

considerably lower than that in asymmetric environments because the former support long range SPP excitation. It has been reported that the attenuation lengths in such arrangement can be as long as 13.6 mm when operated with light at $\lambda = 1550$ nm [89].

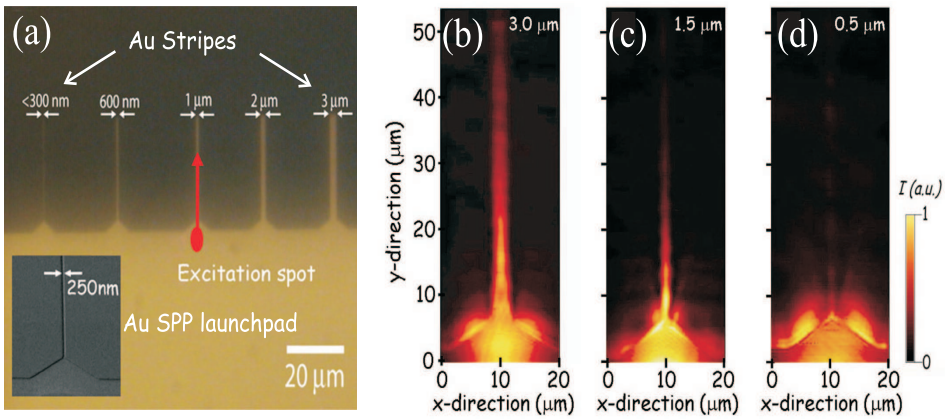

Figure 3.3: (a) A SPP waveguide consisting of an arrays of Au stripes attached to a large Au launchpad. (b)–(d) PSTM images of SPPs excited at $\lambda = 780$ nm and propagating along 3.0 μm, 1.5 μm, and 0.5 μm wide Au stripes, respectively [16]

.

An alternative approach for SP guiding is to use metallic nanoparticle arrays. It was initially proposed by Quinten *et al.* [95] that a linear chain of spherical metal nanoparticles can be used as a subwavelength-sized light guide in which light is transmitted by the coupling of interparticle plasmon oscillations. The subwavelength light confinement in metallic nanoparticle arrays was first verified by Krenn *et al.* [60] through collective excitation of LSPs on the arrays of nanoparticles, as shown in Fig. 3.4; and the EM energy transport along the nanoparticle waveguides was later demonstrated by Maier *et al.* through local spot excitation of Ag nanoparticle arrays interspersed with dye molecules via near-field scanning optical microscope (NSOM) tip pumping [96]. The trade-off between the field confinement lever and the

propagation loss also exists in nanoparticle waveguides. However, as LSP-fields are highly concentrated in the space between metallic nanoparticles rather than on the metallic structures in nanoparticle waveguides, they generally produce the tighter field confinement and lower Ohmic losses when compared to SPP waveguides [60] [15].

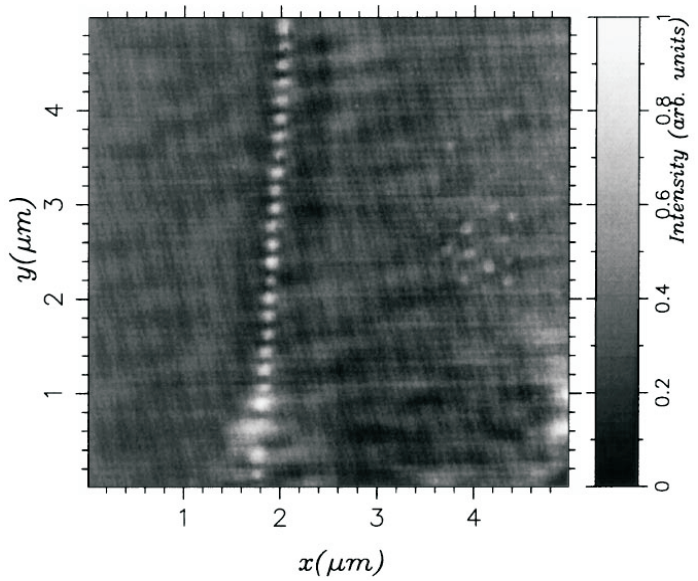

Figure 3.4: Constant height PSTM image of optical near-field intensity above a chain of Au particles on an ITO substrate, illuminated at $\lambda = 633$ nm. The individual particle size is $100 \times 100 \times 40$ nm^3) and the separation between particles is 100 nm. The PSTM tip to Au particles distance is less than 45 nm [60].

.

Recently, a 2-D fibre-accessible metallic nanoparticle waveguide, with measured light coupling efficiency to be as high as 75%, has been reported [14], which could offer the solution to the coupling problem between 3-D optical signals and low-dimensional SP modes. The structure consists of Au nanoparticles whose sizes are gradually decreased from the centre of the waveguide to the edge of the waveguide, as illustrated in Fig. 3.5, which

allows EM energy to be highly confined to the middle of the guide.

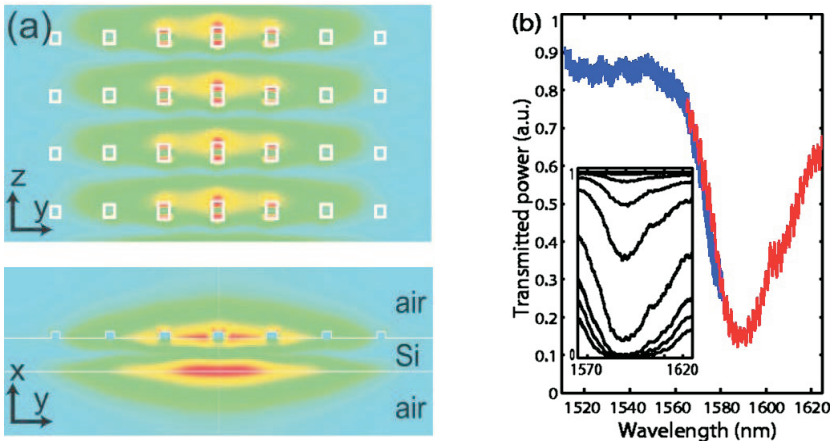

Figure 3.5: Finite-difference time-domain (FDTD) simulation of electric field in a 2-D fibre-accessible metallic nanoparticle waveguide. To enhance lateral field confinement, the sizes of the Au particles vary across the waveguide [14].

.

SP waveguides offer opportunities for future integrated optical or photonic devices, although currently propagation losses and coupling problems are still major challenges for their implementation. In the parallel development of SP waveguides, a variety of 2-D optical elements and devices for SP manipulation have also been demonstrated recently, which are discussed in the next section.

3.2.2 Two-dimensional Optical Elements for Surface Plasmon Manipulation

Controlling the propagation of SPs is of fundamental important to achieve SP-based subwavelength optics. The concept of using 2-D optical elements for SP manipulation was published in the same year as the metallic nanowire waveguide was proposed. When Smolyaninov *et al.* investigated SP scattering by surface defects, they suggested the design of subwavelength

mirrors or lenses for SPP focusing [97]. The experimental demonstration of SP optical elements came in 2002; Ditlbacher and co-workers [12] reported the manipulation of SPP propagation a 70-nm-thick Ag film by introducing various nanoscale optical elements through height modulation on the film. The influence of these elements on the SPP field distribution were detected through fluorescence imaging.

Figure 3.6 summarizes the basic 2-D subwavelength optical elements presented in Ref. [12]. First, a nanowire (a quasi infinite long surface modulation on the Ag film with a crossection of 160×70 nm^2) acts as a SPP source where SPPs were locally excited by focusing a laser beam onto it. Second, nanoparticles (dotted surface modulations with diameter 140 nm and separation 220 nm) arranged in five parallel lines (line spacing 350 nm) serve as a Bragg mirror to redirect the propagation of SPPs. Third, a linear row of nanoparticles (dotted surface modulations with diameter 140 nm and separation 280 nm) functions as a beam splitter to separate the SPPs reflected from the Bragg mirror into two paths.

The demonstration of using properly designed nanostructures to control SP propagation opens up the feasibility of nanoscale optical and photonic devices. For use in the future integrated opto-electronic circuits, miniaturized light-SP conversion devices (also called plasmonic couplers) are needed. The couplers must have high conversion efficiency, along with a transmission length longer than the optical wavelength to avoid the direct coupling of free propagating light to the metallic nanostructures inside the integrated circuits. Whilst 2-D nanoparticle waveguides have been suggested as potential plasmonic couplers [14], the designs based on the combination of nanoparticle/nanohole focusing arrays and waveguide have also been demonstrated [98] [99] as promising candidates.

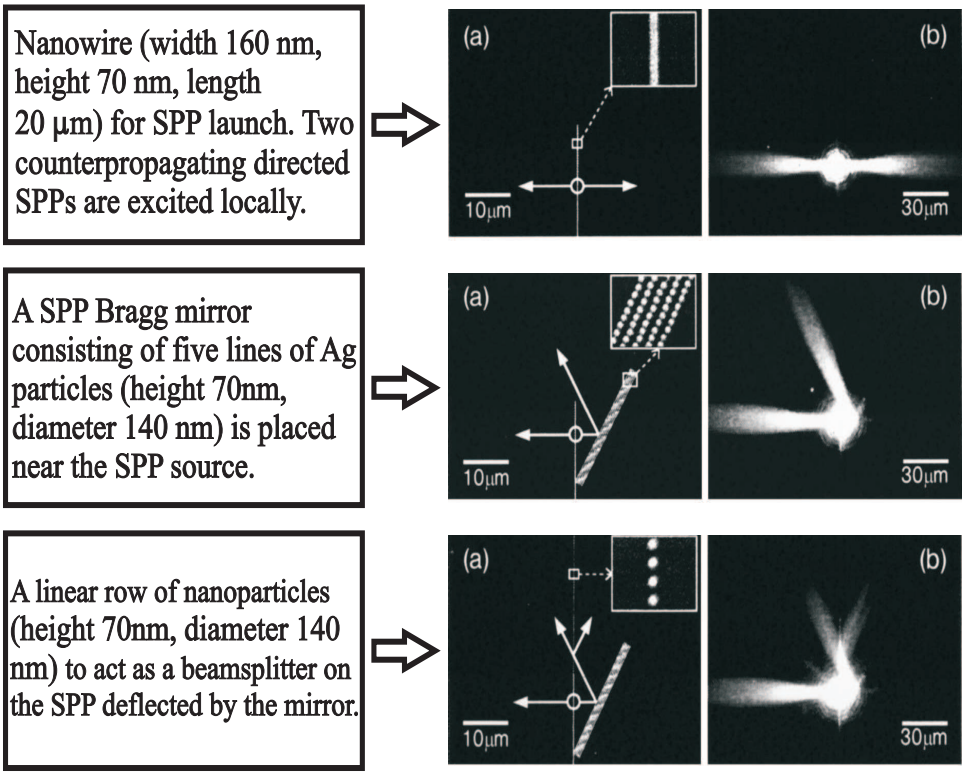

Figure 3.6: Demonstration of 2-D optical elements for SPP manipulation by Ditlbacher *et al.* [12]. The graphs labelled by (a) show the scanning electron microscope images of SPP source (top), mirror (middle) and beamspliiter (bottom), on which the positions of local SPP excitation is defined by the circuit and the directions of SPP propagation are indicated by the arrows; the insets show the magnified images of the area marked by rectangular boxes on each graphs. The corresponding fluorescence images of SPP propagation under the influences of each element are shown in (b)s.

.

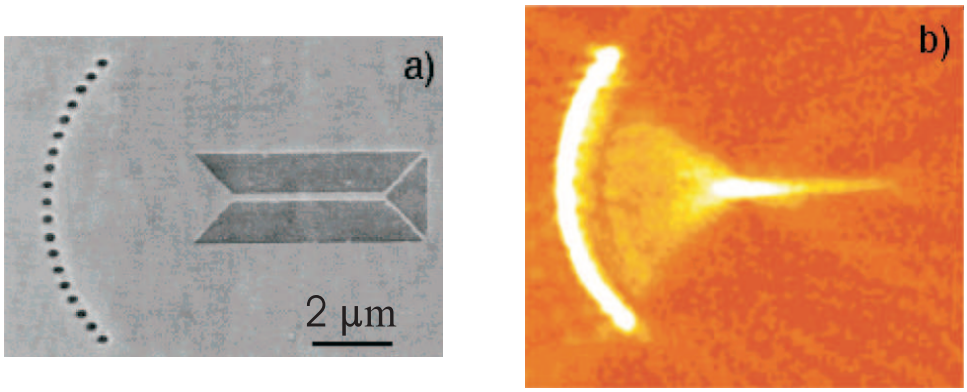

Figure 3.7: (a) SEM image of the focusing nanohole array coupled to a 250-nm-wide Ag stripe waveguide. The light grey color represents the area covered with Au. (b) NSOM image of the SPP intensity showing focusing and guiding [99].

.

Figure 3.7a shows a scanning electron microscope (SEM) image of a plasmonic coupler consisting of a thin Au film pierced with nanometric (diameter 200 nm) holes arranged on a quarter circle (radius 5 μm) and a strip waveguide (width 250 nm, length 4 μm) [99]. When illuminated by a laser beam, each individual hole serves as a SPP point source, and the coherent superposition of these point sources leads to an intense SPP focal spot of subwavelength width located at the center of the circuit. By positioning the input port of the waveguide at this focal point, SPP waves are coupled to the waveguide and delivered to the integrated nanophotonic circuits at the output port. A NSOM image of the SPP intensity, revealing focusing and guiding, is shown in Fig. 3.7b.

On the other hand, components for active control of SP propagation are also being investigated. For example, plasmonic switches and modulators utilizing thermally or optically induced change of the physical properties (dielectric constants, structural phase) of the constituent materials have been

reported [100] [101] [102]. Although not yet fully optimized, these early demonstrations strengthen the prospect for all-plasmonic circuits/devices.

3.3 SPs and Extraordinary Optical Transmission (EOT) Phenomenon

As well as the ability of guiding light on subwavelength scale, SPs have the capability of concentrating/channeling light through subwavelength apertures. In 1998, Ebbesen *et al.* [9] published a paper showing extraordinary light transmission through subwavelength hole arrays in a metallic film. This discovery has received tremendous attention from scientific community and has since stimulated many fundamental studies as well as application-driven research.

Figure 3.8a shows a zero-order transmission spectrum of an Ag hole array (array period: 900 nm, hole diameter: 150 nm, on a 200-nm-thick Ag film) reported by Ebbesen and coworkers [9]. Fig. 3.8b is a focused ion beam image of a hole array with the same geometry arrangement produced by the same group [103]. From Fig. 3.8a, it is clear that sharp peaks in transmission appear at wavelengths as large as ten times the diameter of the holes and the absolute transmission efficiency, calculated by dividing the fraction of light transmitted by the fraction of surface area occupied by the holes, is $\gg 2$ at the maxima. This result is rather contradictory from the aperture theory in conventional optics, which predicts the absolute transmission coefficient η of a subwavelength hole in an infinitely thin and perfect conductor screen as [104]

$$\eta = \frac{64}{27\pi^2}(kr)^4 \tag{3.2}$$

where $k = 2\pi/\lambda$ and r is the radius of the hole. Equation (3.2) indicates that

η scales as $(r/\lambda)^4$; accordingly, the expected η for a hole of 150-nm-diameter under 1370 nm incident light is on the order 10^{-3}.

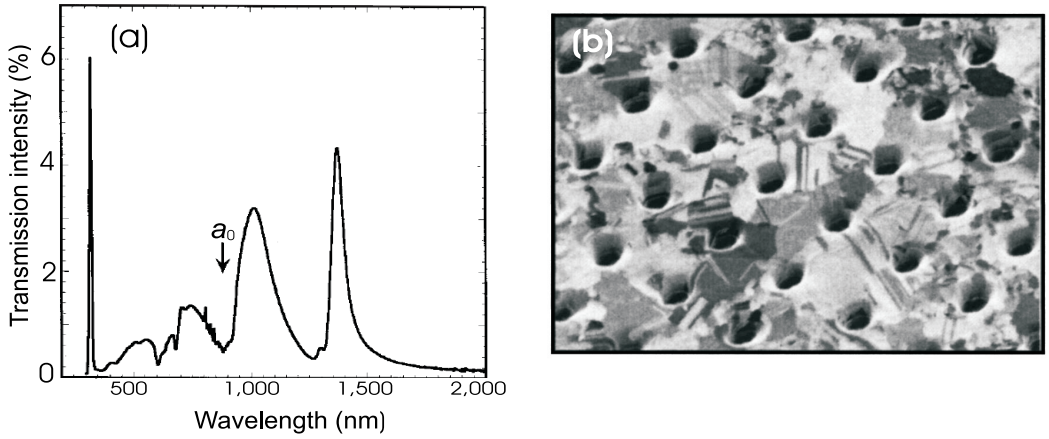

Figure 3.8: (a) Zero order transmission spectrum of an Ag hole arrays (array period a_o = 900 nm, hole diameter d = 150 nm, Ag film thickness t = 200 nm). The absolute transmission efficiency of each individual hole is $\gg 2$ at the maxima (λ = 1370 nm) [9]. (b) A focused ion beam image of an hole array with the same geometry arrangement produced by the same group [103].

.

Based on the experimental investigation on the dependence of the transmission spectra on all possible variables, such as hole diameter, periodicity, film thickness, type of the metal and illumination condition, Ebbesen *et al.* suggested that the extraordinary optical transmission (EOT) phenomenon was attributed to the coupling of light with SPPs at two surfaces of the metal film [9] [103]. A few years later, experimental results showing exclusive dependence of EOT on the in-plane surface dielectric constants of the hole arrays was reported [105], which further strengthen this initial suggestion. Moreover, it was shown [106] [50] that by creating a circular corrugation around a single subwavelength aperture in a metal film, light can be transmitted through the aperture in a well defined direction; the

transmission boost from patterning the surface of the metal film can be an order of magnitude at the resonant wavelength. Besides the subwavelength hole(s) structures, EOT has also been observed on metallic gratings with very narrow slits [107], as well as continuous metal films with periodic surface corrugation [108] in a similar time period.

The early experimental evidence in EOT was consistent with the involvement of SPs rather than conclusive about their involvement. Subsequently, many different theoretical approaches have since been adopted to interpret this surprising findings. Soon after Ebbesen's report of EOT, Schröter and Heitmann [109] calculated the near-field intensity profile at a transmission peak using a one-dimensional metallic grating model, and confirmed the involvement of SPPs in EOT. Porto *et al.* [110] then proposed that in addition to SPPs excitation, the fundamental waveguide resonance (TEM mode) with no cut-off frequency within the slits of the gratings could also give rise to EOT. This has led to a debate about the relative role of two different resonances in EOT. The importance of waveguide resonance has been put forward by papers investigating EOT in subwavelength lamellar gratings, among which the inclusive dependence of EOT on waveguide modes [111] [112] [113], and EOT due to mixed modes from coupling between SPPs and waveguide resonances [114] [115], have been proposed. Conversely, it has been pointed out that the interpretation favoring waveguide resonances can not be used to explain EOT through hole arrays structures as such modes do not exist in metallic films with sub-half-wavelength hole arrays [116] [117]. Some authors [118] [119] also explained EOT in terms of the constructive interference of diffracted evanescent waves from subwavelength structure, regardless of the presence of SPs. Of those that lobby for positive role of SPs in EOT, many have proposed SP-assisted photon tunneling as a possible

mechanism [120] [121] [122] [123]. Extending this further, some authors have suggested that a smooth metal film with dielectric ridges could provide EOT [124] [125].

More recently, the experimental investigation of the influence of the hole-shape on the transmission properties of perforated metal films shows that the presence of LSPs on the aperture ridges adds another factor in EOT [126] [127] [128] [129]. The analytical study on this issue [130] then suggests that coupling between the LSPs on the top and bottom edges of the hole increases the cut-off wavelength of light propagating through the hole and leads to EOT.

The controversy surrounding the transmission mechanism is due to the fact that the subwavelength features can support diverse EM responses depending on the geometry of structures; consequently, the coexistence of these modes in the same film tends to confound the analysis somewhat. Hence it is difficult to draw a direct conclusion. Most recently, several different groups (including ourselves) have studied multilayer systems composed of a patterned metallic layer, such as subwavelength dots [131] [132], gratings [133] [53] and hole arrays [52], closely coupled to a planar metal film. The major advantage of the multilayer system is that it allows the direct observation of *controlled* excitation/coupling of different resonances within the structure. A point of view commonly expressed in these studies is that coupling between LSPs and SPPs can produce a strong field enhancement as compared to the field intensity of LSPs or SPPs alone, which is reflected as extinction or transmission enhancement on the far-field spectra. In particular, our experimental observation of transmission enhancement through planar metal films without any surface modulation [133] [52] confirmed that SP-assisted photon tunnelling is attributable to

EOT. This is one of the major topic covered in these thesis (Chapters 4 and 5).

The finding of the EOT phenomenon not only attracted a great deal of attention concerning its underlying physics, but also stimulated great interest in rediscovery of the properties of the SPs. For example, EOT has been explored in THz and microwave region of the spectrum where SPs are not considered to exist by tradition [134] [135]. Nevertheless, research effects in this field are not limited to these fundamental studies; SP-assisted extraordinary light transmission has been exploited in the fields of enhancing performance of light-emitting devices (LEDs) [136] [137] [138], obtaining nanolithography at deep subwavelength scale [139] [140], studying quantum and atom optics [141] [142] [143], as well as developing miniaturized SPR sensors [75] [76] [77]. As the properties of the SPs can be tailored by adjusting the structural and/or materials parameters the holes, EOT could provide a new means to allow more efficient coupling between freely propagating light and SP-based subwavelength optical elements. For example, it has been suggested [13] that the convex-shaped metallic lenses consisting of a nanoslit array can provide beam shaping (focusing or collimating) functions that resembles conventional refractive optical lenses, without being restricted by the constraints of conventional optics.

3.4 Summary

Recent research activities in plasmonics, including the fundamental studies and application developments, are highlighted in this chapter. With the knowledge and understanding gained from theoretical and numerical analysis, assisted by the advanced fabrication and

characterization techniques, a wide variety of SP-based applications have been proposed/demonstrated in the past decade. SP sensing has become a leading technology for affinity-based biosensing with its focus currently shifting from the conventional SPR sensing to LSPR sensing. SP-based subwavelength optics has achieved widespread recognition as a promising candidate for future nanooptics and nanophotonics. Nevertheless, there is much more to be done to fully realize the potential of SPs.

§ 4. EOT Through Planar Metal Films Coupled to Metallic Gratings

4.1 Introduction

The discovery of extraordinary optical transmission (EOT) through thin metallic films with periodic subwavelength structures [9] has received considerable attention from scientific community. According to the aperture theory in conventional optics, the transmission efficiency of a subwavelength aperture scales as $(r/\lambda)^4$ [104], where r is the radius of the aperture and λ is the wavelength of the incident light. Therefore, there was a common belief that subwavelength apertures could only transmit very small amounts of light. Nevertheless, the observed transmission efficiency (when normalized to the surface area of the holes) is orders of magnitude greater than predicted by the conventional theory [9].

As discussed in Section 3.3, the finding of EOT has provoked many searches for its underlying physics. While it is generally accepted that surface plasmons (SPs) play an important role in the EOT, there also exists an ongoing debate over the detailed mechanisms involved in this phenomenon,

because most studies have been focused on perforated metal films. As the subwavelength features can also support diverse EM responses, the coexistence of the SPs and the subwavelength features that generate them on the same film tends to confound the analysis somewhat.

In this chapter we study the EOT through a multilayer system consisting of a subwavelength metallic grating layer closely coupled to a planar metal film. A schematic of the system is shown in Fig. 4.1. Here the primary role of the grating layer is to provide a coupling mechanism for light-SP interaction on the planar metal/dielectric interfaces underneath. By varying the geometry and the material property of each individual component within the system, we have a direct control of the excitation/coupling of different resonances, which allows us to easily identify the origins of the assorted spectral responses of the system.

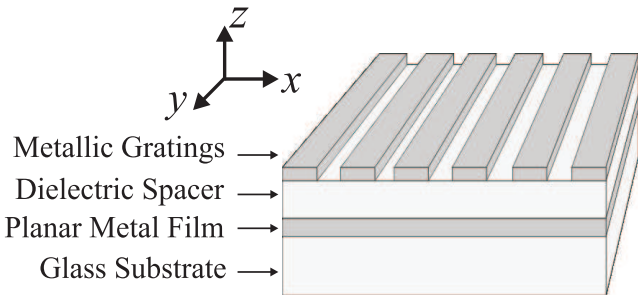

Figure 4.1: A schematic diagram of the multilayer structure studied in this chapter.

The chapter is organized as follows. Section 4.2 describes the experimental study of the EOT through planar metal films coupled to metallic gratings, including sample fabrication process, optical characterization techniques and transmission measurement results. Section 4.3 gives a brief overview of the Rigorous Coupled-Wave Analysis (RCWA) technique that is employed for far-field spectral simulations in this study,

as well as the variables used in the simulations. A detailed exploration of the transmission properties of the structure is then presented in Section 4.4. Section 4.5 is devoted to the analysis of the near-field distributions within the structures using Finite Element Method (FEM) based modelling. A summary of the results presented in this chapter is given in Section 4.6.

4.2 Experimental Procedure and Results

4.2.1 Sample Fabrication

The fabrication of structures such as shown in Fig. 4.1 involves the following processes: vacuum deposition of thin films, grating pattern definition by interference lithography (IL), grating pattern metallization via dry etching (reactive ion etching (RIE)) and lift-off. The schematic of the main steps involved are shown in Fig. 4.2; the details for each step are as follows.

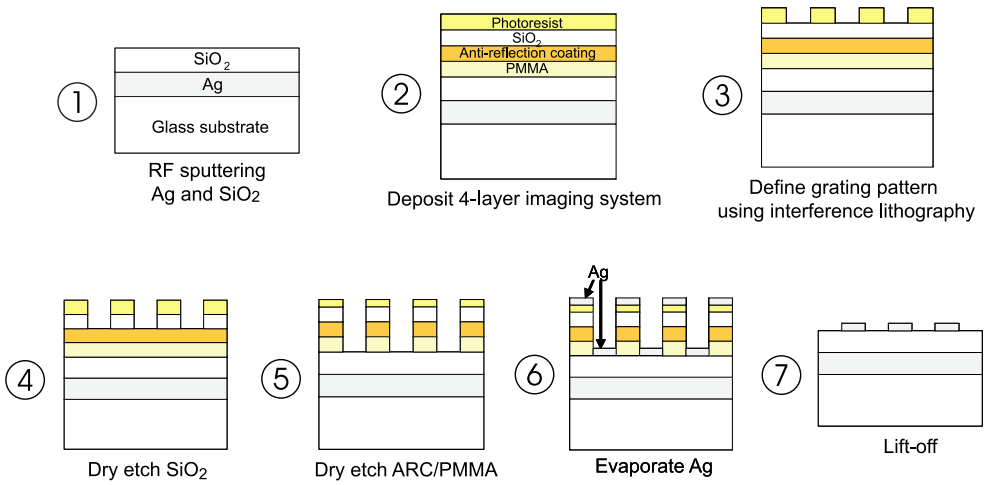

Figure 4.2: Schematic of the main steps in the sample fabrication process.

Step 1: Deposit thin Ag film and SiO_2 layer by sputtering.

The samples are prepared on BK7 glass substrates (microscope cover slips 20 mm × 20 mm × 0.20 mm). After solvent cleaning (acetone, methanol, and IPA), a layer of Ag, followed by a layer of SiO_2, are deposited on the substrates by means of radio frequency (RF) sputtering using an Edwards Auto-500 magnetron sputtering system in Ar^+ gas environment. The process parameters are shown in Table 4.1.

Table 4.1: Process parameters for RF sputtering of Ag and SiO_2

Target	Power	Rate	Temperature	Process Pressure
Ag(99.9%)	50W	0.1nm/s	$25^oC \sim 30^oC$	3×10^{-3}mBar
SiO_2 (99.995%)	200W	0.01nm/s	$25^oC \sim 65^oC$	6×10^{-3}mBar

The thickness of the deposited Ag films are 30 – 40 nm and the thickness of the SiO_2 layer ranges from 180 nm to 220 nm, depending on the structure design. The surface roughness of the films, characterized by the Atomic Force Microscope (AFM) (Digital Instruments 3100), is around 1 nm rms (root-mean-square) with a maximum peak-to-peak range of height under 10 nm. An AFM scan of a planar Ag film surface on glass substrate is shown in Fig. 4.3.

Step 2: Deposit a 4-layer imaging system.

A 4-layer imaging scheme, which is prepared for the late steps of grating pattern definition (lithography) and metallization (lift-off), is deposited on top of the SiO_2 after sputtering thin films. This involves:

1. deposition of a 100-nm-thick PMMA layer by first spin coating (3000rpm, 1 minute) a PMMA/Chlorobenzene solution (2.5% w/w) on the substrate, oven bake at 185^oC for 30 minutes, then cool down

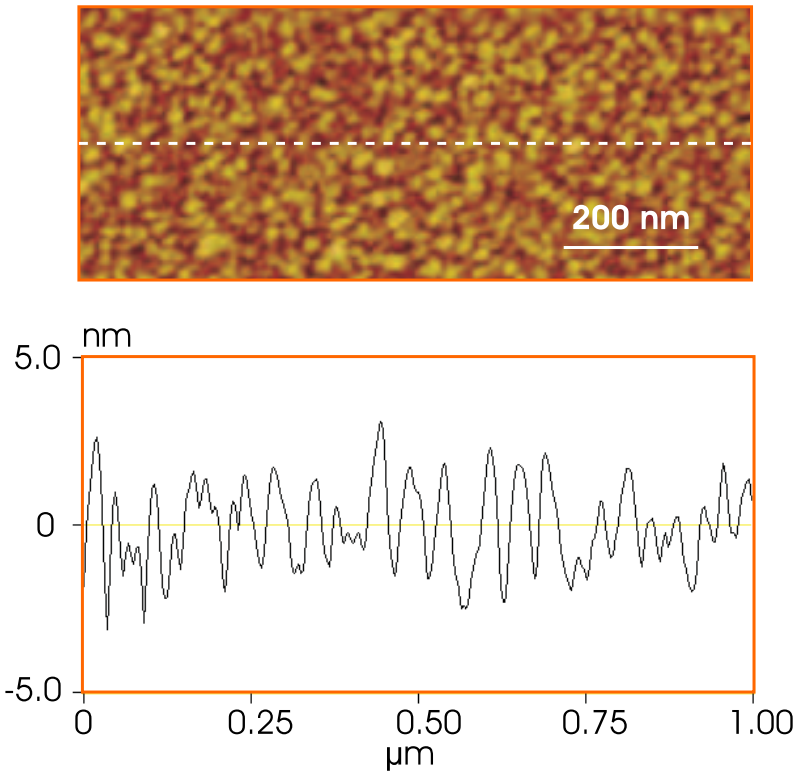

Figure 4.3: AFM scan of a planar Ag film surface (top) and the trace through the marked line (bottom).

to room temperature;

2. spin coating (5000rpm, 1 minute) of a 100-nm-thick bottom anti-reflection coating (ARC) material (Clariant AZ® BARLi® II);

3. RF sputtering of a 30-nm-thick SiO_2 film;

4. spin coating (3000rpm, 1 minute) of a 150-nm-thick i-line photoresist (Clariant AZ® HiR™ 1075 diluted 1:3 with methyl amyl ketone) layer on top.

The grating patterns are firstly defined onto the photoresist (PR) layer by IL; this then serves as a photomask for the subsequential metallization of the desired patterns (lift-off). For a successful lift-off, it is desirable to have an

undercut profile in the photomask. However, the sinusoidal intensity profile of the interference fringe patterns implies that this is difficult to achieve in a single layer resist. In addition, as there exists a highly reflective Ag layer on the substrate and a bottom ARC layer is necessary in order to suppress the light reflection during the IL process. Due to the above constraints, we choose the multilayer imaging system in the sample fabrication, in which the SiO_2 layer serves as a hard etch mask for pattern transfer from the top resist layer to the ARC/PMMA layers underneath. A hard mask is required because the chemical system used to etch ARC/PMMA also etches photoresist, resulting in the erosion of the resist during the opening of ARC layer. The purpose of the additional PMMA bottom layer over the conventional tri-layer system is for easy stripping of the ARC during the final lift-off process.

Step 3: Define grating pattern via interference lithography.

Interference lithography (IL) utilizes the interference of the coherent wavefronts to create periodic patterns. A schematic of the principle of the IL technique is illustrated in Fig. 4.4. The spatial period, P, of the fringe patterns is determined by the wavelength of light source λ and the half-angle of intersection of two coherent beams θ_i via

$$P = \frac{\lambda}{2 \sin \theta_i} \, . \tag{4.1}$$

The width of the grating lines defined on the resist layer is governed by the exposure dose (optical power $\times$ exposure time) onto the resist layer. In addition to the classical one-dimensional line structures obtained by a single exposure of photoresist, more complex two- and three-dimensional patterns can also be generated by using multi-exposure or multi-beam schemes [144] [145].

In this study, we used a custom-built IL system [146], which is based on a

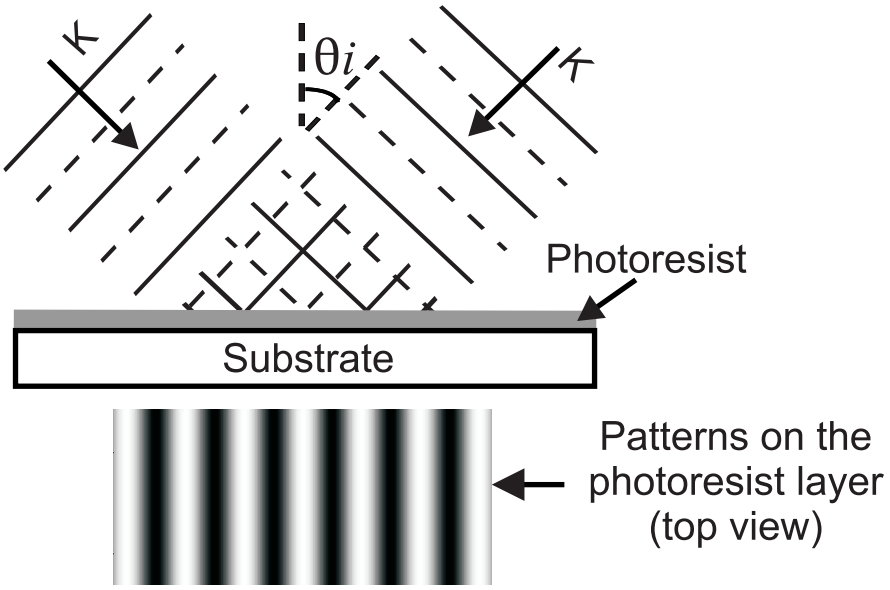

Figure 4.4: Schematic of the principle of the two-beam interference lithography technique.

Lloyd's mirror interferometer, to define the grating patterns. An Argon-ion laser (Spectra-Physics Beamlok 2080-25S) operating at the 364 nm spectral line is employed as the source. The intensity of the light incident on the substrate is 300 μW/cm^2. For grating patterns with periodicity of 450 nm to 550 nm and duty cycle of $40-60\%$, the required time of exposure ranges from 40 seconds to 50 second. After exposure, samples are developed in undiluted AZ® 300 MIF developer (2.18% tetra-methyl ammonium hydroxide (TMAH)) for 7 seconds. The pattern formed in the photoresist layer acts as a photomask in the followed steps. The AFM image of a 500 nm period grating in photoresist is shown in Fig. 4.5.

Step 4 & 5: Pattern transfer through SiO_2 and ARC/PMMA layers by RIE.

Grating patterns in the photoresist are transferred through the resist stack via two separate RIE process using an Oxford Instrument's Plasmalab

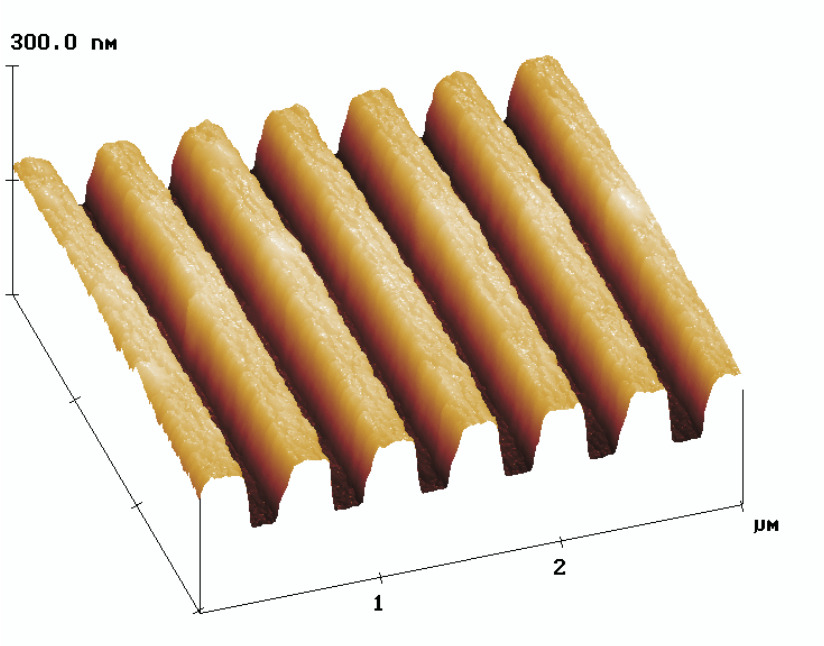

Figure 4.5: AFM image of a 500 nm period grating in photoresist

80 Plus etcher. The first stage uses CHF_3 to etch SiO_2, which produces a hard mask for the following O_2 plasma etch of ARC/PMMA.

The RIE process is a combination of ion bombardment and chemical reaction, from which a good control over etch profiles can be achieved through adjusting a number of the parameters, such as pressure, temperature, plasma power and etchant chemistry. For a successful lift-off, an anisotropic steep resist sidewall profile with slight undercut is essential. The process parameters for etching SiO_2 and ARC/PMMA are given in Table 4.2.

A SEM image showing the profile of the resist stack after the O_2 etch step for a 500 nm period grating is illustrated in Fig. 4.6, where the desired undercut profile has been achieved on the sample.

Step 6 & 7: Deposit Ag via thermal evaporation and lift-off.

Definition of the Ag grating involves two steps. Firstly, a Ag film is

Table 4.2: RIE recipes for pattern transfer through SiO_2 and ARC/PMMA layers (Sample area: 22 mm × 22 mm).

Material	Gas	Etch Rate (nm/min)	Pressure (Torr)	Gas Flow (sccm)	Temp.	RF Power
SiO_2	CHF_3	3.2	0.03	15	295 ^oK	150 W
ARC/PMMA	O_2	30	0.001	5	173 ^oK	100 W

deposited onto the sample by thermal evaporation; secondly, the resist and all metal not adhering directly to the SiO_2 spacer is removed with a solvent – called lift-off.

Thermal evaporation is a highly directional deposition process, i.e., the evaporant arrives at the sample is greatest on the horizontal surface and least on the vertical surface. Therefore, it is a preferred method for pattern metallization. The apparatus used in this process is a Balzers 510-A evaporator system. The process parameters for Ag evaporation are shown in Table 4.3.

Table 4.3: Process parameters for thermal evaporation of Ag.

Target	Power	Rate	Temperature	Process Pressure
Ag pelets(99.9%)	3.5 (on dial)	1nm/s	N.A.	4×10^{-3}mBar

After the thermal evaporation, the final step is to leave the sample in 60 ^{o}C acetone for 30 minutes to dissolve the remaining PMMA on the bottom of the imaging stack. This process removes all metal not adhering directly to the SiO_2 spacer from the the sample and the pattern in the image stack is

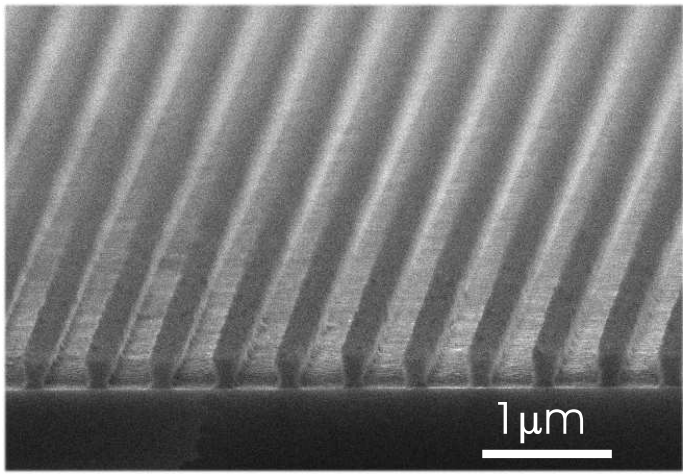

Figure 4.6: SEM image showing the profile the resist stack after ARC/PMMA etch step for a 500 nm period grating.

transferred into metallic gratings with an inverted profile. Fig. 4.7 shows a SEM image of a fabricated 500 nm period Ag grating on top of the sample. The AFM scan of the sample is displayed in Fig. 4.8.

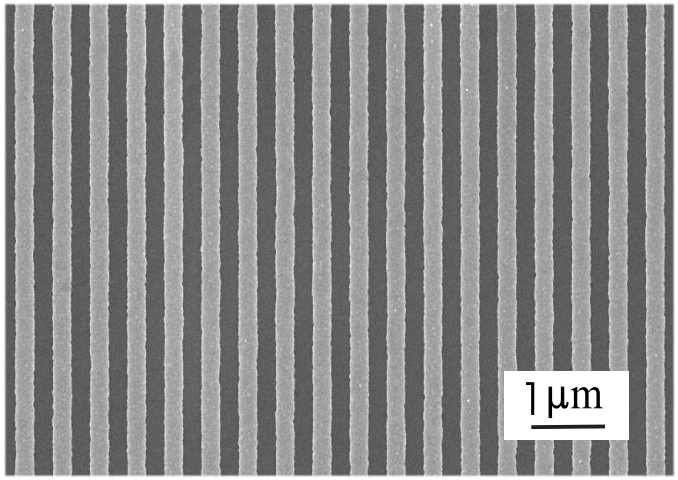

Figure 4.7: SEM image of a 500 nm period metallized grating.

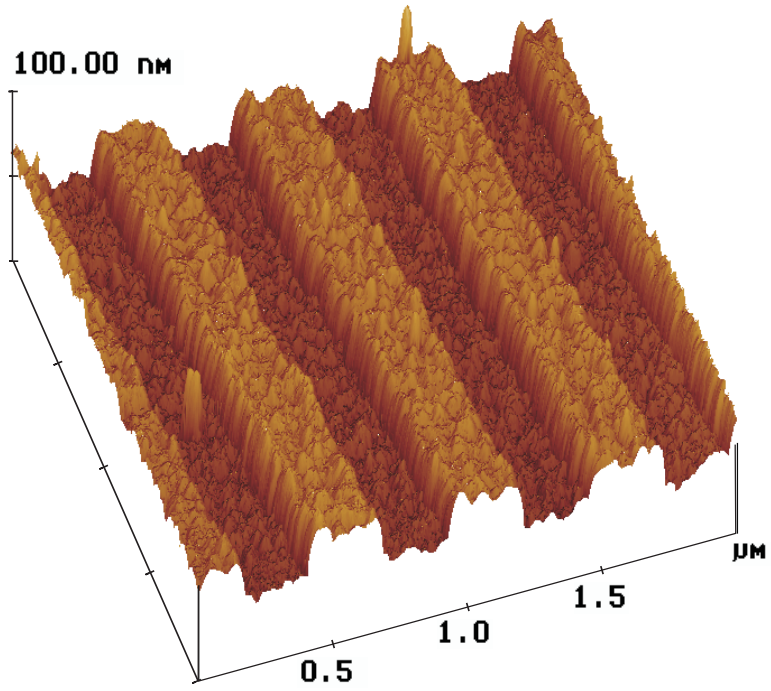

Figure 4.8: AFM scan of the fabricated Ag grating shown in Fig. 4.7.

4.2.2 Optical characterization

The transmission spectra of the samples were recorded in two different spectrophotometer systems. One was a Cary Spectrophotometer (model 14) available at the Department of Physics and Astronomy, the University of Canterbury. The other one was a custom-built spectrophotometer system available at the Measurement Standards Laboratory of New Zealand, which was built up based around a GCA/McPherson 1 metre focal length monochromator (Model 2051, GCA/McPherson Instrument Corp.) fitted with a prism predisperser. A halogen lamp was used as white light source. The spectral bandwidth of the system is adjustable from 0.1 nm up to 3 nm. The schematic diagram of the system set-up is shown in Fig. 4.9.

The monochromatic beam from the monochromator is collected,

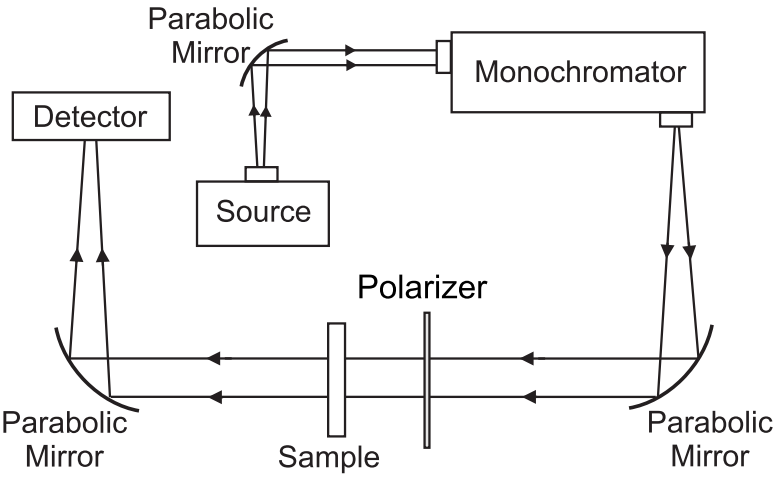

Figure 4.9: Schematic diagram of the custom spectrophotometer set-up used for optical transmission measurement.

collimated and focused onto the optical detector by a pair of off-axis parabolic mirrors. The sample is placed in the path of the collimated beam. The diameter of the incident light is 8 mm and its polarization state is controlled by the polarizer in the front the sample. The detector is a 10 mm^2 silicon photodiode. The measurements were made over the wavelength range 550 nm to 850 nm at 1 nm intervals with a bandwidth of 0.5 nm. The transmittance of the sample at each wavelength is obtained by averaging four transmission readings.

4.2.3 Transmission Measurement Results

Figure 4.10a shows the zeroth order transmission spectra of a fabricated sample under linear polarized light at normal incidence, recorded in the Cary Spectrophotometer. The sample consists of a 35-nm-thick Ag grating layer, a 200-nm-thick SiO_2 spacer and a 35-nm-thick planar Ag film on BK7 glass substrate. The period of the grating is 485 nm and the metallic linewidth of the grating is 265 nm. The dotted line presents the transmission under TE

polarized light (the electric field of the incident light is parallel to the grating); the solid line presents the transmission under TM polarized light (the electric field of the incident light is perpendicular to the grating). Fig. 4.10b shows the transmission calculated from a rigorous coupled-wave analysis (RCWA) [147] based commercial grating analysis tool – G-Solver [148]. The details of this simulation technique will be discussed in the following section. In the simulation, the refractive index of the glass substrate and that of the SiO_2 spacer are fixed to 1.512 and 1.454, respectively; the complex dielectric constants of the Ag are taken from Ref. [41].

Figure 4.10 illustrates that the transmission spectra of the sample are rather different under TE and TM polarized incident light, owing to the presence of the subwavelength metallic gratings within the structure. The measured TE-spectrum shows two broad features, which agrees with the simulation results. In contrast, the measured TM-spectrum exhibits three features: a 40 nm (FWHM) feature at 650 nm wavelength, a narrow feature ($<$ 10 nm FWHM) at 750 nm and a broad feature at 850 nm. All but this last one are similar to the simulations except for the transmission values. We are particularly interested in the EM response of the structure under TM excitation, as for the structure studied here the light-SPP interaction can only occur under TM excitation.

Figure 4.11a shows the zeroth order transmission spectra of three samples under TM polarized light at normal incidence, recorded using the high accuracy spectrophotometer at the Measurement Standards Laboratory of New Zealand. The dashed line is the transmission of the same sample used in Fig. 4.10a (P = 485 nm). The solid line is the transmission of another sample which has a 475 nm period grating on top; the thickness of the each individual layer on this sample is the same as the previous one; and the

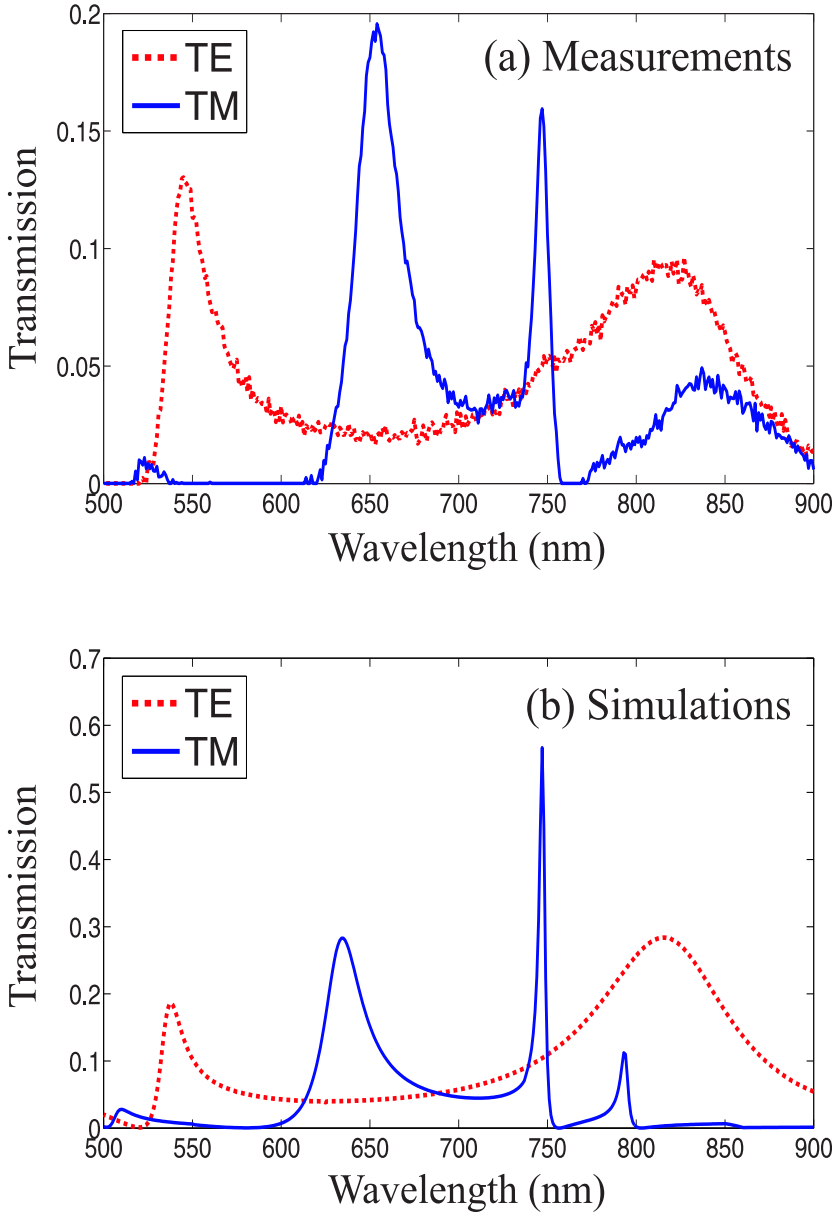

Figure 4.10: (a) Zeroth order transmission spectra of a fabricated sample under TE (dotted line) and TM (solid line) polarized light at normal incidence, measured in Cary Spectrophotometer; (b) the calculated spectra. The sample consists of a 35-nm-thick Ag grating layer, a 200-nm-thick SiO_2 spacer and a 35-nm-thick planar Ag film on BK7 glass substrate.; the period of the grating is 485 nm and the metallic linewidth of the grating is 265 nm.

width of the metallic lines of the grating is 260 nm. For comparison, we also fabricated a planar Fabry-Perot resonator sample consisting of a 200-nm-thick SiO_2 layer sandwiched between two 35-nm-thick planar Ag films on BK7 glass substrate, its transmission spectrum is shown in dotted line. The corresponding RCWA simulation results of these samples are shown in Fig. 4.11b.

In general the TM transmission spectrum of the grating/planar multilayer structure studied here consists three peaks, as indicated in Fig. 4.11. The spectral positions of the these peaks (wavelengths at which transmission maxima occur) obtained from measurements (simulations) for the sample are shown in Table 4.4. Here we observe an excellent agreement between the measurement and the simulation results in the spectral positions of peak 2s and peak 3s, although there is small discrepancies in the positions of the peak 1s.

Table 4.4: The spectral positions of three peaks obtained from measurements (simulations) for 2 fabricated samples with different period of gratings.

Grating Period	Peak 1	Peak 2	Peak 3
475 nm	612 nm (630 nm)	734 nm (734 nm)	779 nm (779 nm)
485 nm	609 nm (633 nm)	748 nm (746 nm)	795 nm (793 nm)

The discrepancies between the experimental and the simulation results in the amplitudes of the peak 2s and peak 3s are likely caused by the surface roughness of the planar Ag film, as well as the surface and line-edge roughness of the Ag gratings, which can be observed in Fig. 4.3 and Fig. 4.8, respectively. These roughnesses produce additional scattering losses in the structure, which have been excluded in the modelling, as the

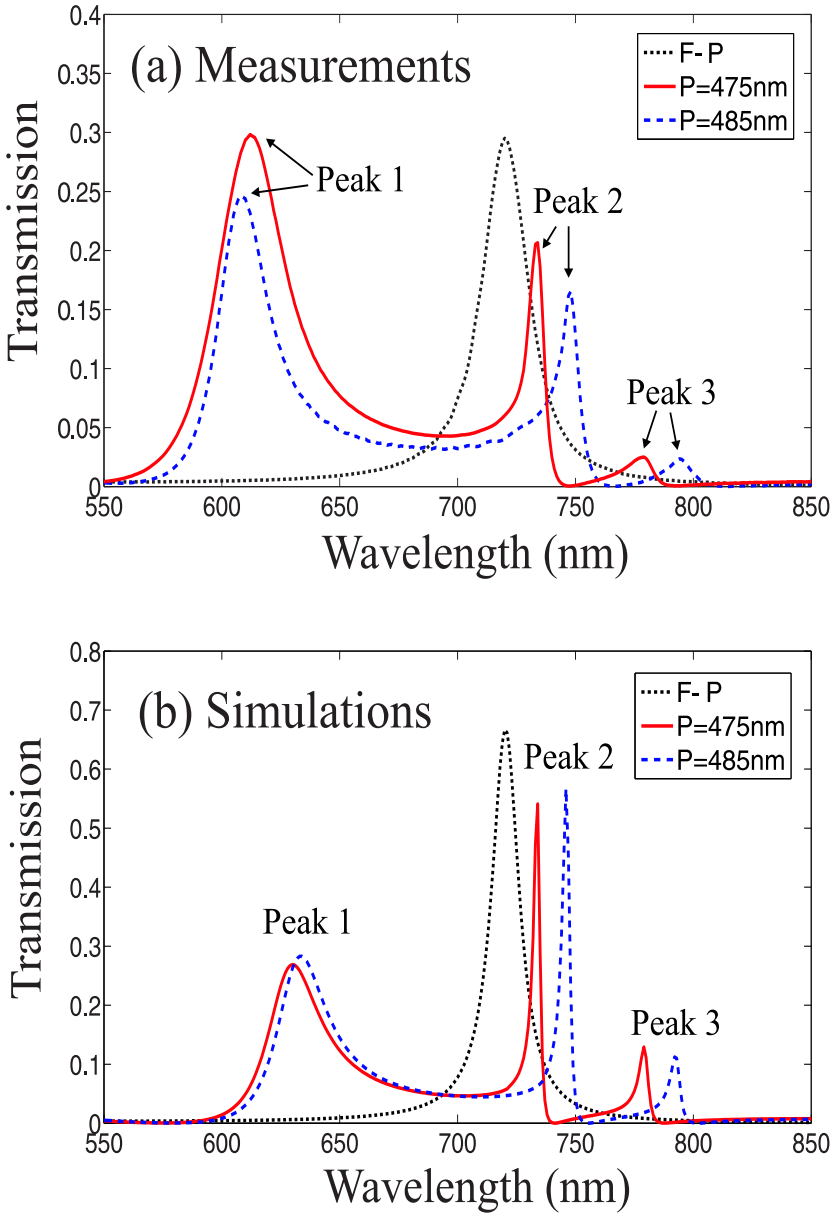

Figure 4.11: Zeroth order transmission spectra of the fabricated samples on BK7 glass substrate ($n = 1.512$) under TM polarized light at normal incidence: (a) measurements; (b) simulation results. The dotted line is the transmission of a Fabry-Perot (F-P) resonator consisting of a 200-nm-thick SiO_2 ($n = 1.454$) sandwiched between two 35-nm-thick planar Ag films; the solid line and the dashed line are the transmission of the samples with 475 nm and 485 nm period Ag gratings on top, respectively.

perfectly flat metal/dielectric films and the ideal rectangular transmission gratings are used in simulations. The negative effects of the scattering loss on the transmission efficiencies of the samples are not only shown on the patterned multilayer structures, but also reflected on the fabricated Fabry-Perot resonantor.

Figure 4.11 reveals that the pronounced, narrow band transmission peak (peak 2) appearing in the TM spectrum of the patterned multilayer structure does not arise from the Fabry-Perot resonance, as its spectral position, shape and linewidth are rather different from the peak produced by the planar Fabry-Perot cavity. Further, the position of this peak is fairly sensitive to the period of the grating. An in-depth analysis of the spectral responses of the structures suggest that this peak and the smaller peak following it are directly related to the SPP excitation on the planar film. After a brief discussion of the simulation technique in the following section, we will reveal this in detail in the simulation studies described in Sections 4.4 and 4.5.

4.3 Spectral Response Simulation Technique

Our current understanding of the optical properties of metallic nanostructures has benefited from the development and commercialization of powerful electromagnetic simulation tools. Simulations allow the relationships between the elements of a system to be analyzed in detail and multiple design options to be compared before implementation. In this section, we first give a brief introduction of the rigorous coupled-wave analysis (RCWA) technique that is used in the study of the far-field response of the planar/grating multilayer system, we then discuss the variables of the multilayer structures in the spectral response simulations.

4.3.1 Rigorous Coupled-Wave Analysis (RCWA)

The rigorous coupled-wave analysis (RCWA), also known as Fourier modal method, was formulated by Moharam and Gaylord to model the diffraction of EM waves by periodic 1-D and 2-D gratings [147]. It is a frequency-domain method based on expanding the fields and material permittivities inside the corrugated region in terms of (finite) Fourier series that are solutions to Maxwell's equations. Matching boundary conditions at the grating interfaces through the calculation of the eigenvalues and eigenvectors of the system equations gives field distributions inside and outside the grating region, which yields the desired complex diffraction efficiencies. The method gives rigorous results in sense that the full set of vector Maxwell's equations are solved with only two simplifying assumptions: 1) a piecewise-linear approximation to the grating construction and 2) a truncation parameter for the Fourier series representation of the permittivity within each grating layer.

The RCWA algorithm calculates the diffraction efficiencies of a stack of lamellar grating layers between two semi-infinite half spaces: the substrate and the superstrate. More complicated grating profiles can be constructed layer by layer so that the permittivity does not vary in the y-direction, as illustrated in Fig. 4.12. The accuracy of the calculation improves as the number of layers used in the step-like approximation increases, although this could result in increasing the computation time. When the model exactly matches the real grating profile, the accuracy is only limited by the number of the diffracted orders for which the diffraction efficiencies are calculated.

The RCWA method is considered to be the most efficient approach for lamellar gratings [149]. As the calculation essentially includes the zeroth order of diffraction, the technique can be used to analyze the optical responses

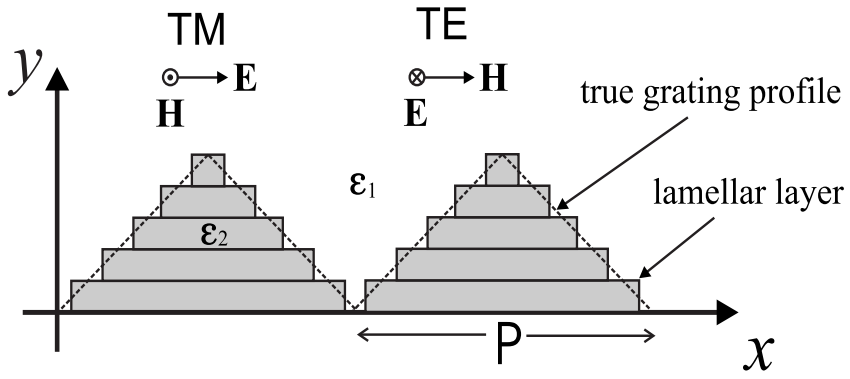

Figure 4.12: Schematic representation of a lamellar approximation to a triangular grating profile using the RCWA method. The linear polarizations TE and TM are also defined.

of the subwavelength gratings, which is particularly useful for the study of EOT phenomenon. It is also interesting to note that there has been some discussion in the literature regarding the convergence of the technique. In the TE-polarized case, the unknown functions are E_z and H_x, both of which are continuous across the grating surface for non-magnetic media. Thus the convergence of their Fourier representation is relatively fast. However, for TM polarization, E_x is discontinuous when crossing the corrugated surface. Therefore, to obtain convergence in the calculation, it requires a high number of Fourier components in expansion of the field for highly conducting grating materials [150], which generally involves long computation times and large memory. Subsequently, a reformulation of the eigenproblem of RCWA has been proposed by Lalanne and Morris [151] to improve convergence rates for TM polarization.

In this study, a RCWA-based commercial grating analysis software, called G-Solver [148], has been used for analyzing the spectral response of the multilayer structures. In addition to the classical two-dimensional gratings (e.g., lamellar, blaze, sinusoidal and triangular), GSolver also handles three-

dimensional grating (cross-gratings which have periodic diffraction structures along both x- and z-dimensions) cases, which is useful for the analyzing EM responses of the structures studied in this chapter and the following chapter (a planar metal film coupled to a hole-array layer).

4.3.2 Variables of the Structure

A major advantage of the multilayer system here is it allows the direct observation of the *controlled* excitation/coupling processes within the structure. Figure 4.13 shows the variables used in the simulations, which can be categorized into the following three groups: 1) illuminating conditions, including: polarization (TE or TM), wavelength λ and angle of incidence θ_i; 2) geometric parameters, including: the thickness of the Ag grating h_g, its period P and duty cycle DC ($DC = w/P$); the thickness of the dielectric spacer h_s; and the thickness of the planar Ag film h_{Ag}; 3) material parameters, including: the refractive index of the dielectric spacer n_d and that of the substrate n_s. By varying a single parameter at a time in each series of simulations and analyze the response of the structure, we can easily identify the origins of the different resonances within the structure.

Although several metals, such as Au, Ag, Cu and Al, can support SP excitation at optical wavelengths, Au and Ag are the most commonly used metals. Furthermore, SPP waves propagating along the surfaces of Ag are less attenuated and exhibits higher localization of electromagnetic field in the dielectric than SPPs supported by Au [11]. We therefore use Ag in our study of EOT. In the simulations, the complex dielectric constants of the Ag are taken from Ref. [41].

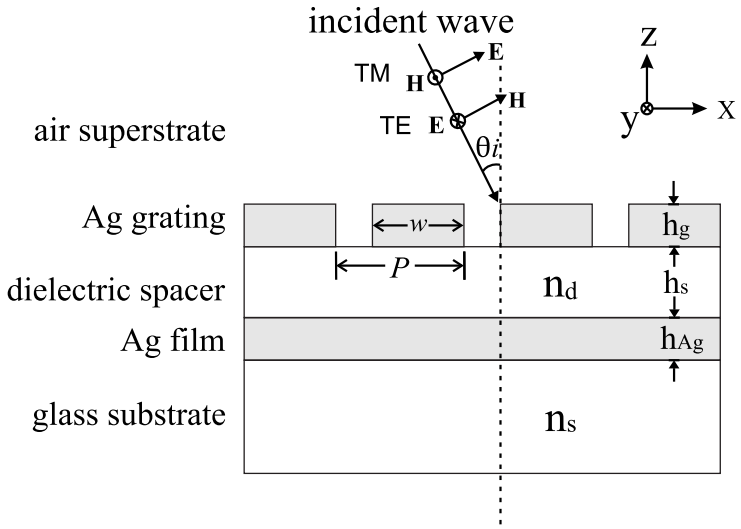

Figure 4.13: Variables of the planar-grating multilayer structure used in the spectral response simulations.

4.4 Spectral Properties of the Structures

To analyze the spectral response of the structure, several series of simulations have been carried out using G-Solver. Fig. 4.14 shows the simulated zeroth order transmission spectra of a Ag grating-dielectrics-Ag film multilayer structure under TE (dashed line) and TM (solid line) polarized light at normal incidence, where $P = 500$ nm, $DC = 0.6$, $h_g = 30$ nm, $h_s = 200$ nm, $h_{Ag} = 30$ nm and $n_d = n_s = 1.5$. For comparison, the transmission spectrum of a Fabry-Perot resonator consisting of a 200-nm-thick dielectric material ($n = 1.5$) sandwiched between two 30-nm-thick planar Ag films is also shown in Fig. 4.14 (dotted line).

The TM-spectra of the patterned structures generally consists of three peaks, whereas the TE-spectra usually contains two peaks. In particular, we notice that there is a pronounced, narrow band transmission peak appears in the TM-spectrum (peak 2, at around 770 nm in Fig. 4.14); in this case, the simulated transmission efficiency exceeds 60% with only 7 nm linewidth

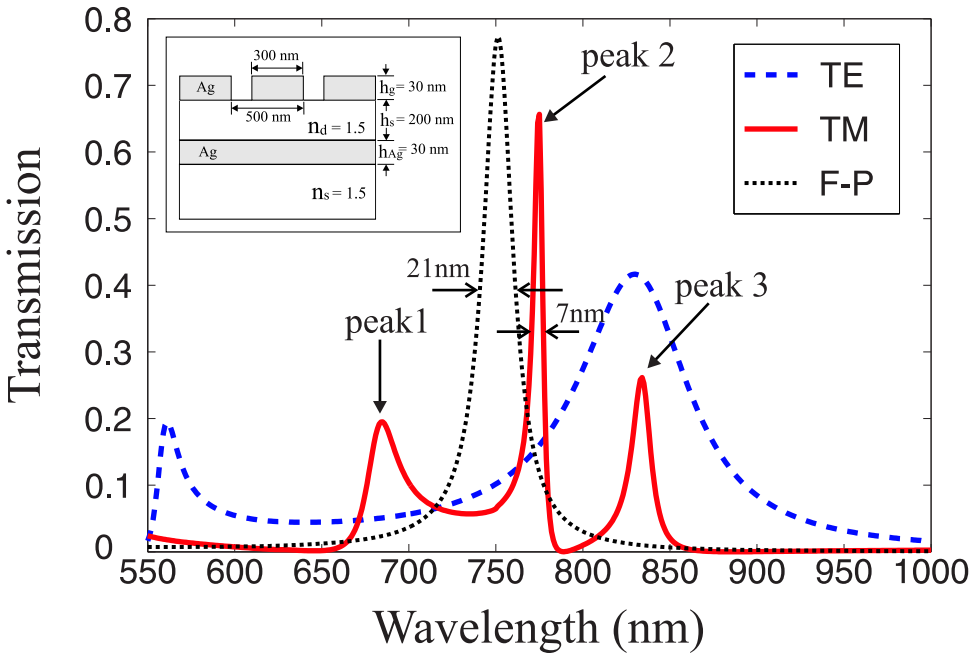

Figure 4.14: Zeroth order transmission spectra of a Ag grating-dielectrics-Ag film multilayer structure under TE (dashed line) and TM (solid line) polarized light at normal incidence. The structure parameters are shown in the insert. The transmission spectrum of a Fabry-Perot (F-P) resonator consisting of a 200-nm-thick dielectric material ($n = 1.5$) sandwiched between two 30-nm-thick planar Ag films is also shown as dotted line.

[full width at half-maximum (FWHM)], which is much narrower than that of the Fabry-Perot resonance (FWHM = 21 nm). The simulations reveal that this extraordinary transmission peak, along with the small peak that follows it (peak 3 in Fig. 4.14), originate from the excitation of SPPs on the planar Ag films. In the following discussions, we will reveal this by investigating the EM response of the patterned structure to the variation of the different parameters. We use the structure for Fig. 4.14 as the base structure, and only change a single parameter at a time in each series of simulations.

4.4.1 Effects of Grating Periods

To start with, we investigated the effects of the grating period on the spectral response of the multilayer structure. Fig. 4.15a and Fig. 4.15b show the zeroth order transmission spectra of the structures under TM and TE polarized light at normal incidence, respectively. The periods of the grating range from 450 nm to 550 nm, and the duty cycle is fixed at 0.6. Fig. 4.15c displays the spectral positions of the transmission peaks vs grating periods extracted from Fig. 4.15a and 4.15b, which shows that while the grating period affects the positions of all of the peaks in both TM- and TE-spectra in certain degrees, the parameter has more impact on peak 2 and peak 3 in the TM-spectrum than on the others.

Recall that the light-SPP interaction initiated by the grating coupler, as discussed in Section 2.4.1; at normal incidence the Equations (2.40) and (2.41) can be combined and rewritten as

$$k_{sp}^{\pm}(\omega) = \frac{\omega}{c}\sqrt{\frac{\varepsilon_d \varepsilon'_m(\omega)}{\varepsilon_d + \varepsilon'_m(\omega)}} = m\frac{2\pi}{P} \ , \tag{4.2}$$

where $k_{sp}^{\pm}(\omega)$ represents the wavevectors of two SPP modes (a high frequency mode ω^+ and a low frequency mode ω^-) existing on the interfaces of a thin metal film whose dispersion relation satisfy the Equations (2.33) and (2.34). With the aid of the following relationship

$$k_{xi}^2 + k_{zi}^2 = \varepsilon_{ri}\left(\frac{\omega}{c}\right)^2 \ , \tag{4.3}$$

$k_{sp}^{\pm}(\omega)$ can be solved numerically. Where $k_{xi} = k_{sp}^{\pm}$, k_{zi} is the wave vector in the metal or the dielectric along z-direction, and ε_{ri} represent the dielectric constant of the metal or dielectric.

Figure 4.16 shows the calculated ω^+ (solid line) and ω^- (dotted line) modes excited by the first order scattering process ($m = 1$) on a 30-nm-thick

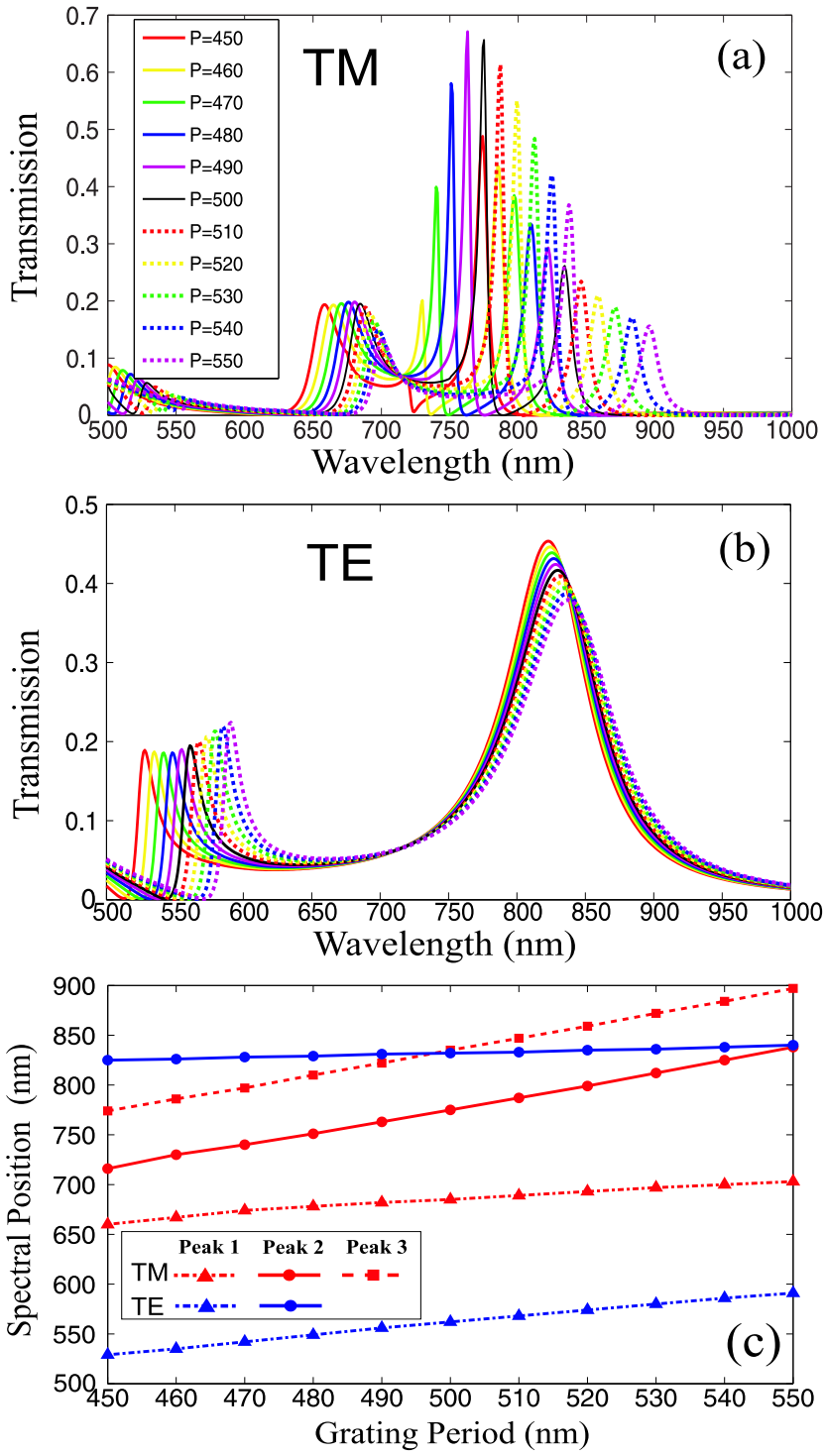

Figure 4.15: Effects of the grating period on the zeroth order transmission spectra of the multilayer structures under (a) TM and (b) TE polarized light at normal incidence, where $P = 450$ nm ~ 500 nm. The spectral positions of the peaks in (a) and (b) vs grating periods are displayed in (c).

Ag film surrounded by dielectric media of refractive index $n = 1.5$, as well as the simulated spectral positions of the peak 2s (circles) and the peak 3s (squares) in Fig. 4.15a. The experimental positions for the samples whose measurements are shown in Fig. 4.11 are also plotted as open circles and squares (note the difference between the Ag film thickness in Fig. 4.15a and in Fig. 4.11). We only consider the effects of the first order scattering process here as the wavelengths of the SPPs (particularly, the ω^+ mode) excited by the higher order scattering processes ($m > 1$) fall below the period of the grating coupler. Fig. 4.16 reveals that the trends in the spectral positions of peak 2 and peak 3 in TM-spectra vs the grating periods closely follow the dispersion relations of the ω^+ and ω^- SPP modes on the Ag film, even through there exist some mismatch between the spectral positions of these two peaks presented through the multilayer structures and the theoretical wavelengths of the SPP modes on a thin, isolated planar Ag film.

It is worth noting that the calculated dispersion relations of $\omega^\pm$ modes obtained from Equations (2.40) and (2.41) includes only the interaction between the two SPP modes on the surfaces of the planar Ag film; it does not consider any coupling effects between the SPPs and other resonances that might exist within the structure. In fact, these coupling effects also strongly affect the transmission efficiency of the structure. As observed in Fig. 4.15a, the high transmission efficiencies occur at the wavelengthes around 750 nm to 800 nm; outside this range, the transmittance is relatively low. The existing coupling effects within the structure will be revealed in Section 4.4.4.

4.4.2 Effects of Ag Film Thickness

The variable in the second series of simulations is the Ag film thickness. According to Equations (2.33) and (2.34), the dispersion relations of the

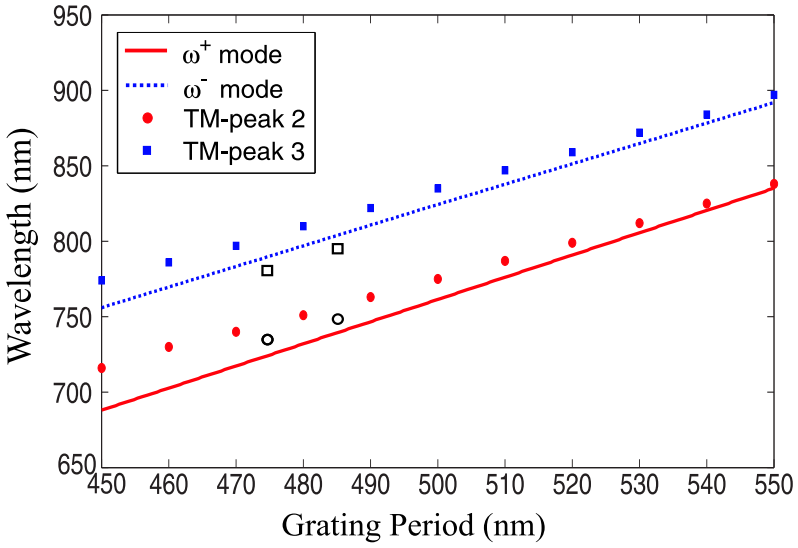

Figure 4.16: Dispersion relations of the ω^+ and ω^- mode excited by the grating couplers via the first order scattering process ($m = 1$) on a 30-nm-thick Ag film surrounded by dielectrics media ($n = 1.5$) and the spectral positions of the peak 2s and the peak 3s in Fig. 4.15a. The experimental positions for the samples ($h_{Ag} = 35$ nm) whose measurements are shown in Fig. 4.11 are also plotted as open circles and squares.

$\omega^{\pm}$ modes on a thin metal film vary as a function of the thickness of the planar metal layer. Fig. 4.17a and 4.17b, respectively, shows the zeroth order transmission spectra of the multilayer structures under TM and TE polarized light at normal incidence, in which h_{Ag} varies from 15 nm to 50 nm. Under TM-excitation, both spectral position and amplitude of the peak 1 in the transmission spectrum are barely affected by the variation in the Ag film thickness. The position of the peak 2 is also hardly changed and its amplitude exhibits a maximum at $h_{Ag} = 25$ nm. Conversely, the position of peak 3 shifts considerably ($\sim$ 100 nm decrease) as h_{Ag} increases from 15 nm to 50 nm. On the other hand, under TE-polarized light, the changes in the spectral positions of the peaks are relatively small ($\sim$ 25 nm shifts for both peaks as h_{Ag} increases from 15 nm to 50 nm) and the overall transmission

efficiencies of the structure decreases continually as the thickness of the planar Ag film increases.

The wavelengths of the $\omega^{\pm}$ modes excited on the planar Ag films of various thicknesses by a grating coupler of period 500 nm can be obtained by using the method described in the Section 4.4.1. The results are displayed in Fig. 4.17c, along with the spectral positions of the peak 2s and peak 3s extracted from Fig. 4.17a. Clearly, the movements of peak 2 and peak 3 as a function of the Ag film thickness closely match the trends in the theoretical curves for $\omega^{\pm}$ modes.

It has been reported [152] that the optical power coupled into the SPP modes on a continuous thin Ag film increases with increasing film thickness, so does the absorption in the metal. The competition between these two process results in an optimum film thickness at which SPP-assisted light transmission reaches the maximum. We observe a similar effects in the peak 2s of the TM-spectra, as shown in Fig. 4.18. The transmission maximum occurs at $h_{Ag} = 25$ nm; and decreasing h_{Ag} does not increase the transmission efficiency, even through this reduces the absorption in the metal. We would like to stress that we only consider the transmission efficiencies of the peak 2s here because the spectral positions of these peaks are fairly close, which ensures that the thickness of the planar Ag film is the *single key factor* that affects the transmission efficiency of the peak 2. The peak 3s do not fall into this category as there are the considerable variations in the spectral positions of these peaks.

4.4.3 Dielectric Constants of the Spacer and Substrate

The optical response of the structures to the variations of the grating period and the thickness of the planar Ag film under TE- and TM-polarized

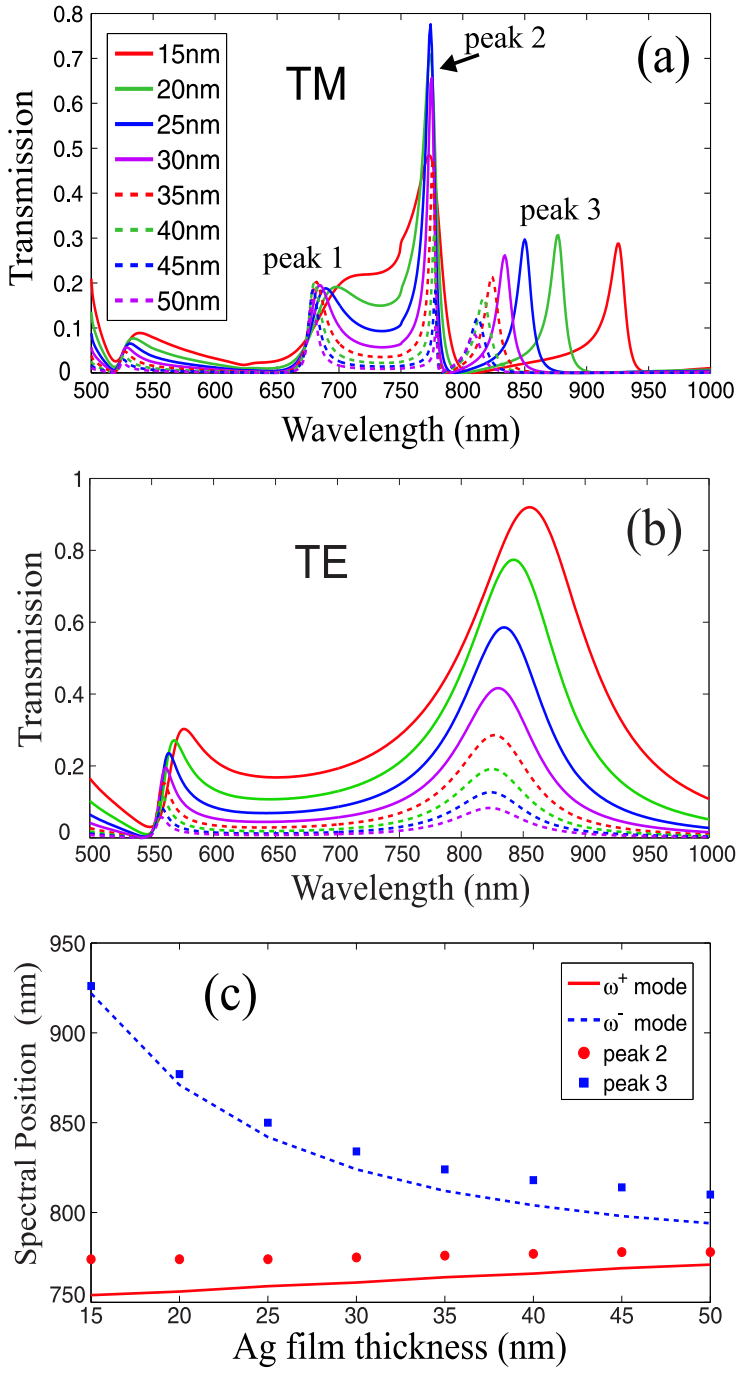

Figure 4.17: Effects of Ag film thickness on the zeroth order transmission spectra of the structures at normal incidence under (a) TM polarized light and (b) TE polarized light, where h_{Ag}= 15 nm $\sim$ 50nm. The theoretical values of SPP modes excited on the planar Ag films via a grating coupler (P = 500 nm), as well as the spectral positions of the peak 2s and peak 3s in (a) are displayed in (c).

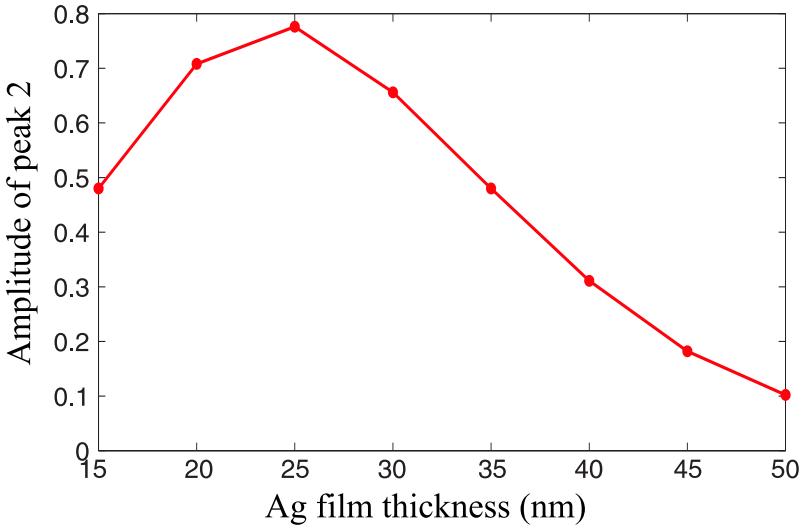

Figure 4.18: The amplitude of peak 2 in Fig.4.17a.

light strongly suggests that the peak 2 and peak 3 in the TM transmission spectrum of the structure are related to the excitation of SPPs on the planar Ag film. To further confirm this, we analyzed the effects of dielectric constants of the materials surrounding the planar Ag film. The dispersion relation of the SPPs on a metal/dielectric interface are determined by the dielectric constants of the metal and its adjacent dielectrics. This implies that the wavelengths of the $\omega^{\pm}$ modes on a thin metal films are highly sensitive to the optical properties of the dielectric materials on either side of the metal film as well.

Figure 4.19 illustrates the effects of changing n_d (refractive index of the dielectric spacer) and/or n_s (refractive index of the substrate) on the zeroth order transmission spectra of the structures under TM polarized light at normal incidence. It shows that peak 1 in transmission spectrum is influenced by n_d only; varying n_s has little effects on this peak. This suggests that peak 1 is related to a waveguide/cavity resonance in the dielectric spacer (further explored in the next section). On the other hand, the spectral positions of the

peak 2 and peak 3 are highly sensitive to both n_d and n_s. A relatively small variation ($\Delta n = 0.05$) in either of these parameters brings about noticeable changes in the positions of these two peaks, which agrees with the nature of the SPP excitations.

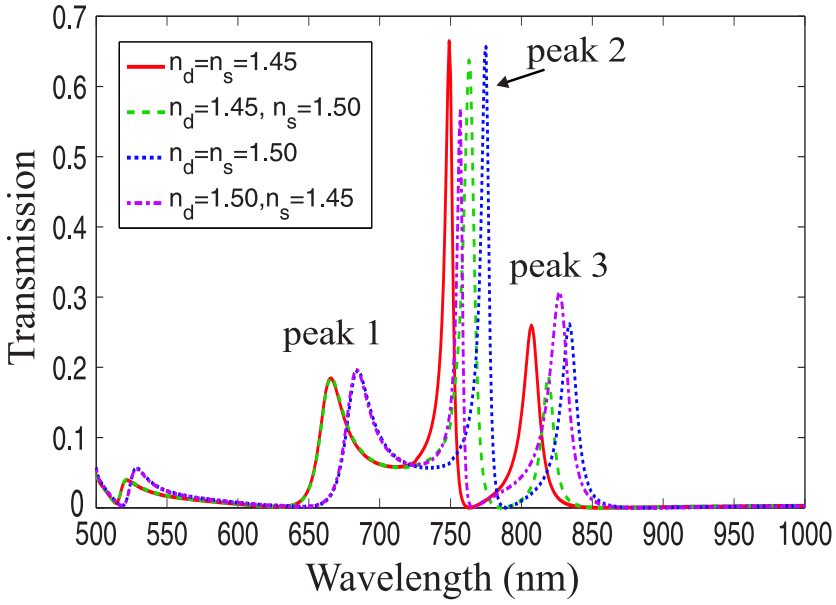

Figure 4.19: The zeroth order transmission spectra of the structures under TM polarized light at normal incidence, where the variables are the optical constants of the dielectric materials surrounding the planar metal films. n_d is the refractive index of the dielectric spacer and n_s is the refractive index of the substrate.

Another interesting feature shown in Fig. 4.19 is that for the asymmetric arrangements (i.e., $n_d \neq n_s$), switching the dielectrics on two sides of the planar Ag film causes observable variations in the amplitudes and the spectral positions of the both peak 2 and peak 3. This further confirms there exists other coupling effects existing within the structure, which cause the deviations in the wavelengths of peak 2 and peak 3 from the theoretical values, as observed in Fig. 4.16 and 4.17c.

4.4.4 Grating Layer Thickness, Grating Duty Cycle and Spacer Thickness

The optical responses of the planar-grating multilayer structures to the variation of the grating period, Ag film thickness and dielectrics surrounding the Ag film strongly suggest that the extraordinary sharp transmission peak (peak 2) presented in the TM-spectrum, as well the small peak that follows it (peak 3), are linked to the excitation of SPP modes on the thin planar Ag film. However, there are also other unresolved questions regarding the optical response of the structure, such as the origin of the broad peak appearing at the shorter wavelength side of the TM-spectrum (peak 1), other possible resonances affecting the spectral position and amplitude of the transmission peaks, and the mechanisms behind the high transmission properties of the structure. To investigate these, we analyze the influences of the thickness of the grating layer h_g, the duty cycle of the gratings DC and the thickness of the dielectric spacer h_s, on the transmission properties of the structure under TM-polarized light and the results are shown in Fig. 4.20a, 4.20b and 4.20c, respectively.

The results shown in Fig. 4.20a – 4.20c, and that in Fig. 4.19, reveal that the spectral position and amplitude of the peak 1 are strongly affected by the geometry of the nano-cavities formed by the metallic lines of the gratings and the planar metal films underneath, as well as the optical properties of the filling material in the cavities. The thickness of the grating layer also modifies the characteristics of this peak moderately. Furthermore, we observe (results not shown here) that while a small (< 5 degrees) variation in the angle of incidence can dramatically modify the shapes of peak 2 and peak 3 in TM-spectrum, the change has little effect on the position and amplitude of the peak 1. Based on these observation, we consider the peak 1 is caused

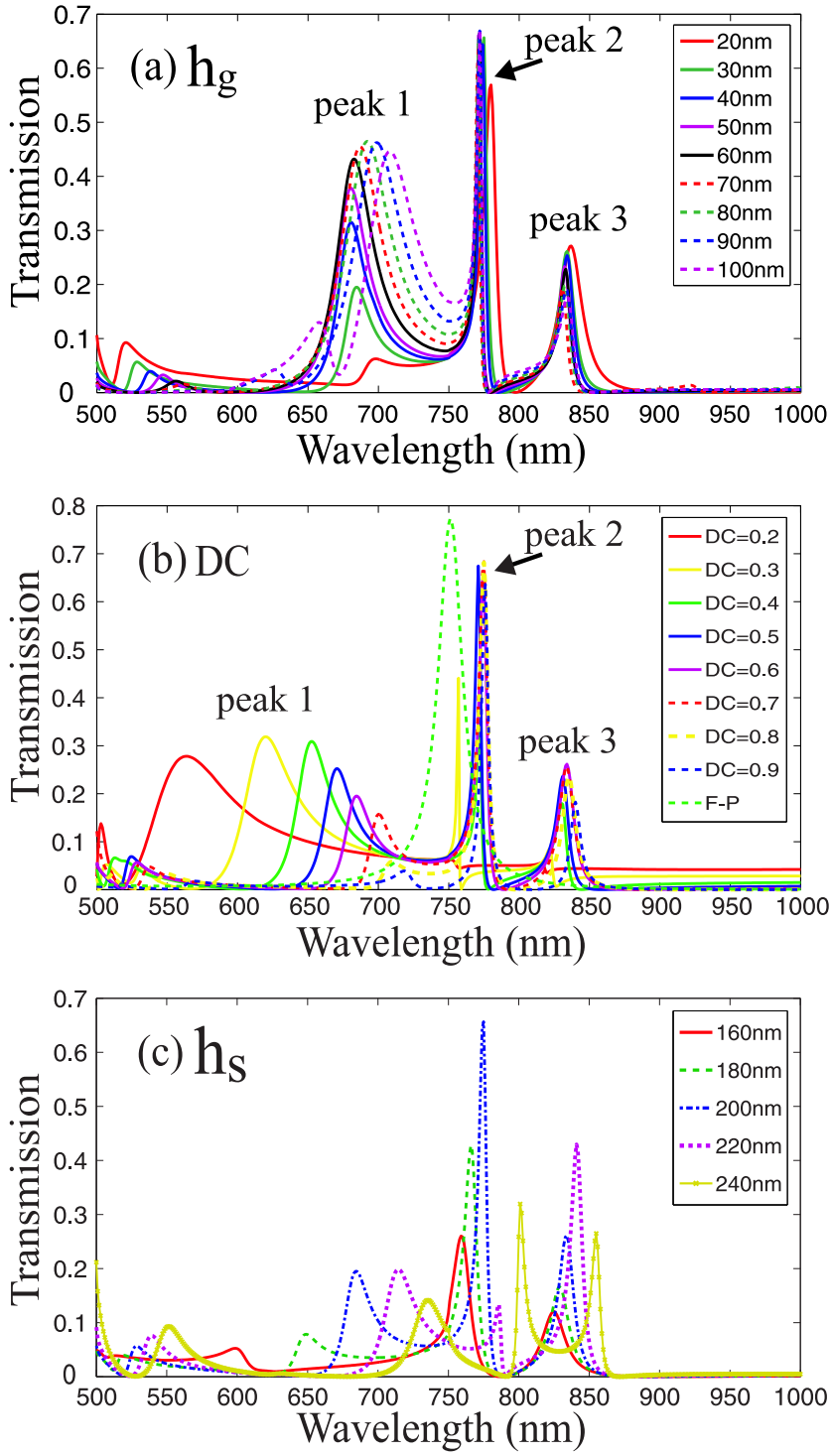

Figure 4.20: Effects of (a) grating layer thickness h_g, (b) duty cycle DC and (c) dielectric spacer thickness h_s on the zeroth order transmission spectra of the structure at normal incidence. The values of the parameters used in these simulations are the same as those in Fig. 4.14 except the variable used for each series of simulations.

by the excitation of a waveguide-cavity resonance within the opening of the gratings and the dielectric spacer. Fig. 4.20c also shows that adjusting the thickness of the dielectric spacer modifies both the amplitudes and the wavelengths of the peak 2 and peak 3. In particular, this adjustment has an significant impact on the amplitudes of these two peaks, which reveals the possible influence of the cavity resonance to the SPP transmission peaks.

4.5 Near-field Simulation

The far-field spectral responses of the structure to the variations of the geometries and the material properties of the elements under TM-polarized light suggest that the overall transmission properties of the structure arise from the co-existence of the waveguide-cavity resonance and SPP resonance within the structure. To obtain insight into the effects of different resonances hence to gain understanding of the physics behind the unusual transmission properties of the structure, we model the field distribution at different resonances using the *Finite Element Method*.

4.5.1 The Finite Element Method

The Finite Element Method (FEM) is a computational method for solving partial differential equations. The method has its origin in solving complex problems in the field of structural analysis. Owing to its ability to handle arbitrary shapes and realistic materials, the method has become a general tool for electromagnetic analysis since 1968 [153]. The FEM is based on subdividing the domains of a geometric object into a finite number of discrete elements of simple shapes (e.g., triangular or quadrilateral in 2D and tetrahedral or hexahedral in 3D) that are easy to analyze. As illustrated

in Fig. 4.21, the dimensions of the elements can be smaller in the regions containing geometric details and larger elsewhere so that the object can be modelled with greater accuracy without unnecessarily increasing the number of elements in the domains with large-scale features.

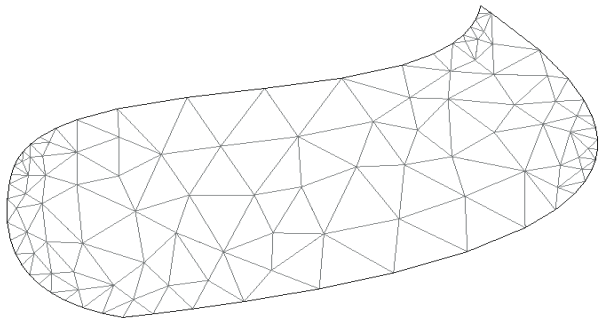

Figure 4.21: Finite element discretization of an irregular 2D object.

In the analysis of electromagnetic problems using FEM, each element is assumed to have an unknown elementary field variable ϕ that satisfies the differential Maxwell's equations. ϕ_i is nonzero within the element i but zero outside it. At any point (x, y, z) within the element, $\phi_i(x, y, z)$ can be approximated with a function $\tilde{\phi}_i(x, y, z)$ that is governed by the geometric shape of the element, as well as the values of ϕ_i at the nodes (vertices) of the element. The field distributions in various elements are linked through the boundary conditions at the inter-element boundaries and the entire field in the modelling region, Φ, is approximated as

$$\Phi(x, y, z) \simeq \sum_{i=1}^{N} \tilde{\phi}_i(x, y, z) \; . \tag{4.4}$$

When Φ is substituted into the wave equation

$$\nabla \cdot q_1 \nabla \Phi + \frac{\omega^2}{c^2} q_2 \Phi = 0 \; , \tag{4.5}$$

where q_1 and q_2 are scalars related to polarization of the waves and the ε_r and μ_r of the medium, an error or *residual* will exist due to the above approximation in the solution. By minimizing the residual over the simulation domain, the unknown nodal values of $\tilde{\phi}_i$ can be found, and subsequently, electromagnetic response can be predicted.

In this work, a commercial FEM program called FEMLAB (COMSOL) [154] is used to model the field distributions within the multilayer structure. It is also possible to retrieve the complex E-field amplitude of every diffraction order from RCWA-based G-Solver program, and subsequently, reconstruct the overall field distribution in the structure. However, RCWA method involves only finite Fourier series expansion of the field. In contrast, FEM technique calculates the entire field in the structure without any approximation in the order of the fields involved. Further more, the modelling process involved in FEMLAB is rather straightforward. We therefore employed FEMLAB for near-field analysis in this thesis.

4.5.2 Simulation Results

To clarify the character of the transmission peaks that occurred under TM-excitation, we simulate the near-field distributions within the structure whose transmission properties are displayed in Fig. 4.14. In the simulations, perfectly matched layers (PMLs) were placed at the top of the air superstrate and the bottom of the glass substrate for absorbing propagating waves; the distances between the top (bottom) PML and the upper (lower) boundary of the multilayer structure is 1.4μm. Perfect electric conductors (PEC) were assigned to two side boundaries (direction: perpendicular to E-field). A surface current boundary placed at 400nm distance away from the grating surfaces is used as excitation. The mesh elements were created by using free

mesh function in FEMLAB, in which the predefined "normal" mesh sizes were selected for global mesh parameters and a maximum element size of 5×10^{-9} was chosen for the domains containing Ag grating and planar Ag film. Fig. 4.22 shows the E-field distributions at $\lambda = 687$ nm, 775 nm and 834 nm, which corresponds to the wavelength of the transmission maximum of peak 1, peak 2 and peak 3 in Fig. 4.14, respectively. The E_x component is a superposition of the incident field and the scattered field, and the E_z component is the fields scattered by the metallic gratings.

Figure 4.22a shows that at $\lambda = 687$ nm (T_{max} of peak 1), the incident field (x-polarized) is highly reflected by the subwavelength metallic gratings. The amplitude of the E_x component is rather large in the dielectric spacer layer (more specially, in the space under the metallic lines), and the E_x shows the sinusoidal profiles below the planar Ag film, which reveal the waveguide-cavity resonance nature of the peak 1. On the other hand, in addition to the first order scattering process, the contributions from the second order scattering process at this wavelength is not negligible, as the G-Solver simulation (results not shown here) reveals that in the first order transmission spectrum (related to the second order scattering process), there exists a transmission peak ($T_{max} = 15\%$) at the wavelengths range between 650 nm to 700 nm. At this wavelength, E_z fields related to the first and second scattering processes are both free propagating in nature; the interference between these two leads to the standing wave pattern shown in E_z of Fig. 4.22a.

Figure 4.22b illustrates the field distributions at $\lambda = 775$ nm (T_{max} of peak 2). The maximum amplitude of E_x component occurs in the space between the metallic lines and the planar metal film, which indicates the excitation of the waveguide-cavity resonance within the structure at this wavelength. The

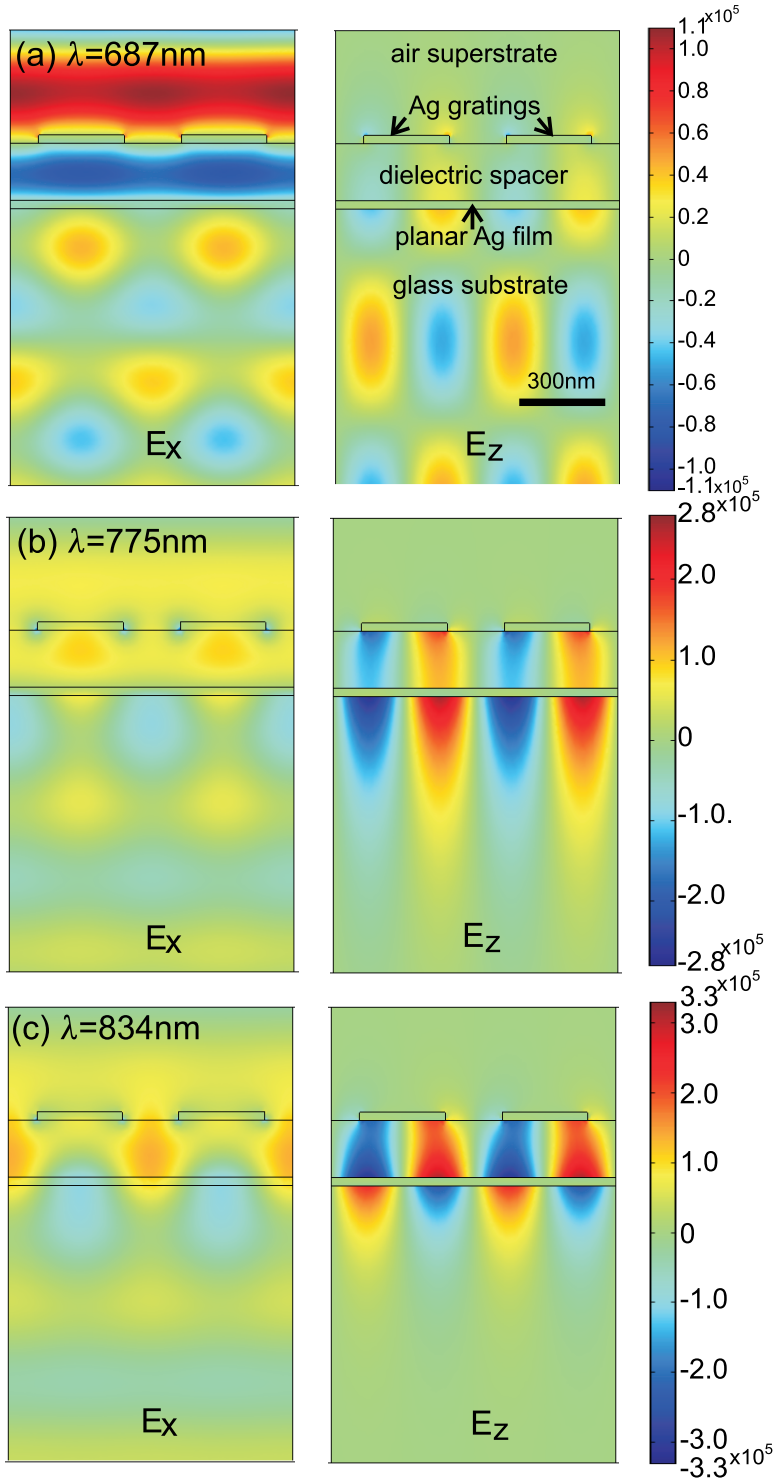

Figure 4.22: E-field distributions of the three peaks in the TM-spectrum in Fig. 4.14. Note the scale difference at three different wavelengths.

strength of this waveguide-cavity mode is slightly larger than that at $\lambda =$ 687 nm. At $\lambda = 775$ nm, the contributions from the higher order scattering process becomes negligible (in the first order far-field transmission spectrum, the transmission coefficient approaches zero); E_z is predominantly caused by the first order scattering process. On the exit side of the planar Ag film, E_z shows the character of the SPP excitation, that is, the field amplitude has its maximum value on the interface and decays exponentially away from the interface. In contrast to the E_z profile shown in Fig. 4.22a, Fig. 4.22b reveals that at $\lambda = 775$ nm, E_z is highly concentrated at edges of the metallic lines, and the electrical charge distributions on the opposite edges of the grating line have different signs. On account of the fact that the width of the metallic lines is considerably smaller than the wavelength of the incident light, we consider the field localization is due to the excitation of LSPs on the metallic gratings.

The field distribution at $\lambda = 834$ nm (T_{max} of peak 3) is shown in Fig. 4.22c. Here the E_x maximum occurs in the space between the slit of the grating and the planar metal film, the amplitude of the E_x is relative smaller in the cavity formed by the metallic lines and the planar metal film. Yet again, the E_z component exhibits the SPP resonance character on the surfaces of the planar Ag film. The surface charge distribution is asymmetric on two surfaces of the planar Ag film at this wavelength, which is quite the opposite to the E_z at $\lambda = 775$ nm, where the surface charge distribution is symmetric on two surfaces of the planar Ag film. These results confirm that the peak 2 and peak 3, respectively, is due to the excitation of the ω^+ and ω^- SPP mode on the planar Ag film.

In conclusion, the calculated near-field distributions at three transmission peaks of the TM-spectrum in Fig. 4.14 confirm that the peak 1 originates

from the excitation of the waveguide-cavity resonance within the dielectric spacer, whereas the peak 2 and peak 3 arise from the coupling between the cavity modes, LSP mode and the SPP modes within the structure. The latter leads to the deviation of the spectral position of peak 2 and peak 3 from the theoretical curves, as observed in Fig. 4.16.

4.6 Summary

The optical transmission properties of the planar metallic films closely coupled to subwavelength metallic gratings have been investigated. The results reveal that surface-plasmon-assisted extraordinary light transmission can be achieved through such configuration. Transmission resonances with peak transmission of $\sim 20\%$ have been measured, and simulations suggest that transmission of $> 65\%$ with FWHM < 10 nm should be possible. By analyzing the effects of geometric factors and the material parameters on the transmission properties of the structure, the excitation of waveguide-cavity resonance, LSP and SPP resonances within the structure has been identified, and the overall optical response of the structure is a result of the couplings between these modes. In particular, the unusual grating-period-dominated transmission peaks are attributable to the excitation of surface plasmon polaritons on two surfaces of the planar metal films.

§ 5. EOT Through Planar Metal Films Coupled to Metallic Hole Arrays

5.1 Introduction

A topic of dispute in the physical origins of the EOT through single-layer subwavelength metallic channels is the different EM resonances that subwavelength gratings and hole arrays can support. For example, in addition to SPs excitation, the *slits* of the metallic gratings can support the fundamental waveguide resonance (TEM mode) with no cut-off frequency, which could lead to the EOT [110] [114] [115]; whereas such mode does not exist in the hole-array structures [116] [117]. Furthermore, regardless the SPs excitation, a thin metallic grating layer can also act as a wire-grid polarizer which produces a strong absorption of TE polarized light (E-field is parallel to the wires) while being essentially transparent to TM one (E-field is perpendicular to the wires) [7]. In contrast, a thin hole-array layer does not show such behavior.

Owing to the difference between EM response of the subwavelength metallic gratings and hole arrays, it is also worthwhile to analyze the optical

properties of the planar metal films closely coupled to metallic subwavelength hole-array layers, even though in this thesis work the primary role of the patterned layer is to provide a coupling mechanism for light-SP interaction on the planar metal/dielectric interfaces underneath.

5.2 Structure Design, Fabrication and Optical Characterization

A schematic of the structures studied in this chapter is shown in Fig. 5.1. It consists of a glass substrate, a planar metal (Ag) film and a metallic (Ag) hole-array layer separated by a dielectric spacer. The variable parameters are: the refractive index of the dielectric spacer n_d and that of the substrate n_s; the thickness of the hole-array layer h_g; the thickness of the dielectric spacer h_s; the thickness of the planar Ag film h_{Ag}; the lattice constants of the hole arrays along the x- and y-direction are P_x and P_y, respectively; the axis length of the holes along the x- and y-direction: D_x and D_y, respectively.

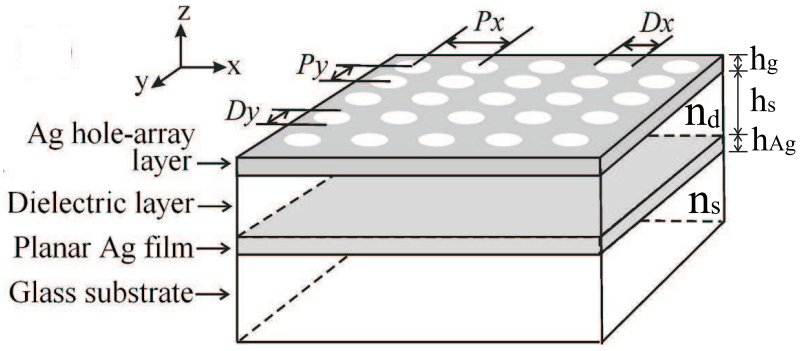

Figure 5.1: A schematic diagram of the multilayer structure studied in this chapter.

The sample fabrication follows similar procedures to those outlined in

Section 4.2.1. Hole arrays were initially defined as dot arrays in the photoresist layer, which were generated by double exposure in an IL process with the sample rotated by 90 degrees; the dot-array patterns were converted to metallic hole arrays after final lift-off step. Fig. 5.2 shows a SEM image of a hole arrays on top of a fabricated sample.

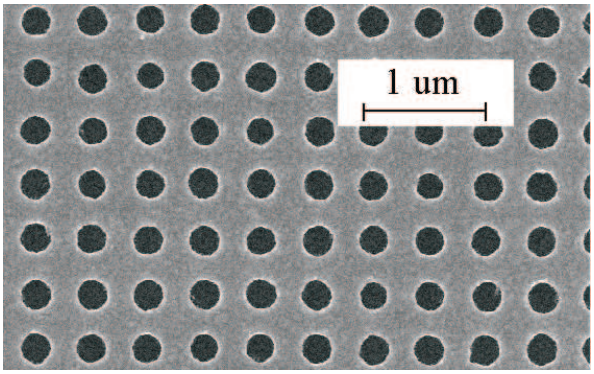

Figure 5.2: A SEM image of a hole arrays on top of a fabricated sample.

We fabricated a series of samples on BK7 glass and fused silica substrates. The lattice constants of these samples range from 460 nm to 560 nm; and P_x and P_y are slightly ($\sim$ 10 nm) mismatched by design on each individual sample. For all the samples, h_g, h_s and h_{Ag} were fixed to 35 nm, 195 nm and 33 nm, respectively, in order to provide some comparison with the grating samples.

The transmission and reflection spectra of the fabricated samples under linear polarized light at different angle of incidence were recorded in the high accuracy spectrophotometer system available at the Measurement Standards Laboratory of New Zealand, as shown in Fig. 4.9. The measurements were made over the wavelength range from 550 nm to 1000 nm at 1 nm intervals with a bandwidth of 0.5 nm, with samples fixed at the required angle to

the collimated monochromatic beam. The transmission measurements were performed at 0 degree and 5 degrees incidence; the reflection measurements were performed at 5 degrees incidence. The reflectance measurements were made relative to the known reflectance from one surface of a wedged fused quartz sample as a reference.

5.3 Transmission Spectrum and Near-field Distributions

5.3.1 Far-field Transmission Spectrum of the Structure

Figure 5.3a shows the measured transmission spectra of a typical sample at normal incidence. The sample is fabricated on BK7 glass substrate with $P_x = 460$ nm and $P_y = 470$ nm, on which the holes have an elliptic shape with axis lengths $D_x = 238$ nm and $D_y = 216$ nm. The dashed and solid lines represent the transmissions under which the E-field of the incident light oscillates parallel with P_x and P_y, respectively. The corresponding simulation results obtained from G-Solver are shown in Fig.5.3b. In the simulation, the elliptic holes were replaced with rectangular holes of the same surface area to reduce computation time. The complex refractive indices of Ag are attained from linear interpolation of the tabulated data in Ref. [41]; the refractive indices of the SiO_2 and BK7 glass are set to 1.454 and 1.512, respectively.

As shown in Fig. 5.3, the transmission spectrum of the multilayer system studied here is similar to that in the previous chapter, except that there is an additional peak (peak 4) appearing at the longer wavelength side of the spectrum. Again, here we observe a very sharp, transmission peak (peak 2) in the transmission spectrum, and the measured transmission maximum

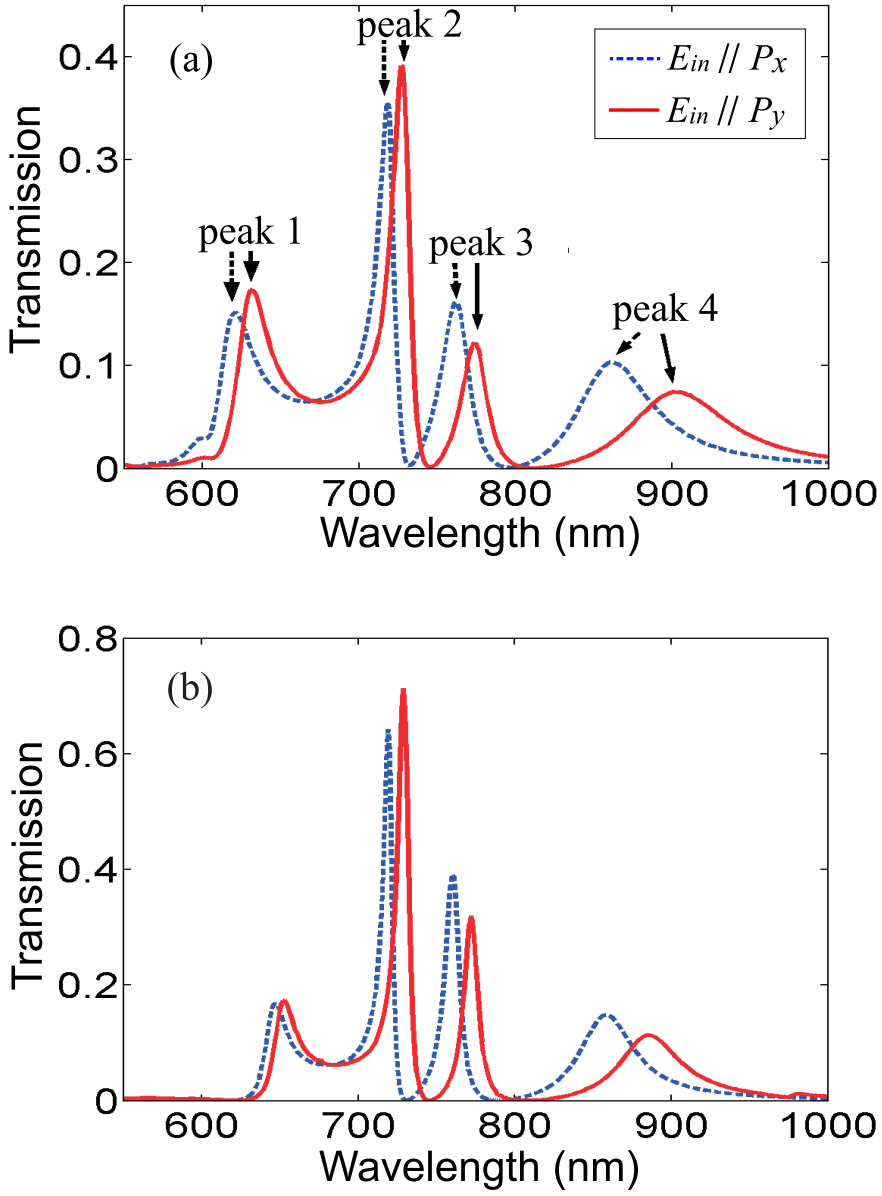

Figure 5.3: Transmission spectra of a fabricated sample at normal incidence with the E-field parallel to P_x (dashed line) and P_y (solid line), where P_x = 460 nm and P_y = 470 nm. (a) measurements and (b) the corresponding simulation results.

reaches 39% for the $E_{in}//P_y$ spectrum in Fig 5.3a.

We also notice that change polarization state of the incident light from $E_{in}//P_x$ to $E_{in}//P_y$ increases the wavelength of all the peaks. Note that on this fabricated sample, not only P_x and P_y, but also D_x and D_y, are different. We therefore performed a set of simulations where the asymmetric holes on top of the sample were replaced with square holes of the same surface area, and the results are shown in Fig. 5.4 (dashed lines). For comparison, the simulation results for the structure with rectangular holes (as shown in Fig.5.3b) are also displayed in Fig. 5.4 as thin solid lines. Clearly, for structure with square holes, peak 1 under two different polarizations become overlapping, so does the peak 4. However, the spectral positions of the peak 2 and peak 3 remain untouched while changing the shape of the holes, which suggests that the wavelengths of the peak 2 and peak 3 are solely governed by the lattice constants of the hole arrays on the sample, whereas peaks 1 and 4 are determined by the detailed geometry of the holes themselves.

5.3.2 Near-field Distributions at Transmission Peaks

We simulated the near-field distributions within the structures at the transmission maxima of the four peaks in the $E_{in}//P_y$ spectrum shown in Fig. 5.3b (the solid line). The wavelengths of peak 1 through 4 are $\lambda_1 = 654$ nm, $\lambda_2 = 729$ nm, $\lambda_3 = 772$ nm and $\lambda_4 = 887$ nm, respectively. The results obtained from FEMLAB are displayed in Fig. 5.5, where the E_y component is a superposition of the incident field and the scattered field, and the E_z component is the fields scattered by the metallic hole arrays.

Figures 5.5a – 5.5c reveal that the E-field distribution of peak 1, peak 2 and peak 3 in the transmission spectrum of the hole array/planar film structure closely resembles that of the grating/planar film structure, as

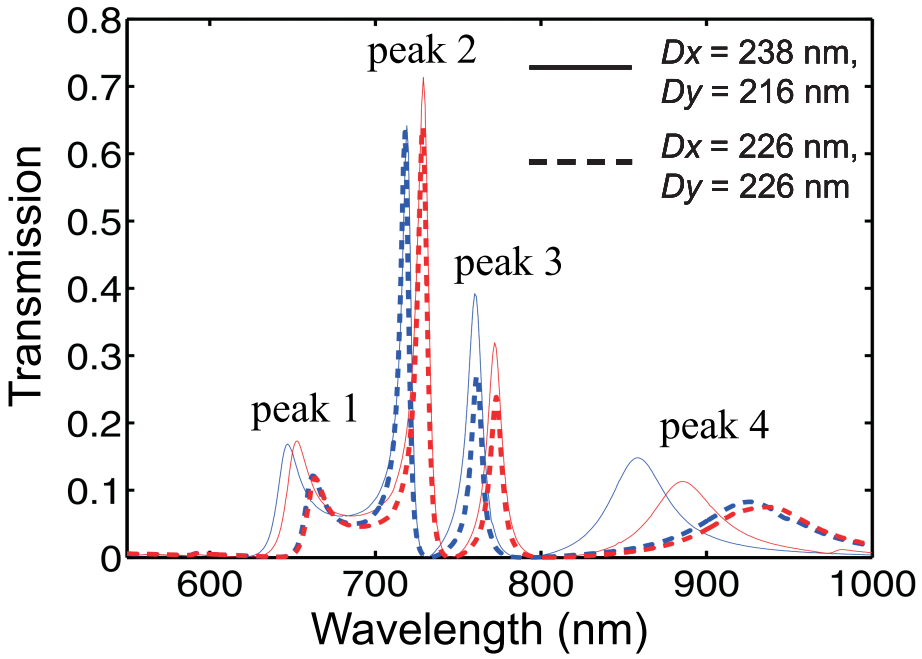

Figure 5.4: Simulated transmission spectra of the multilayer system having same structural arrangement as the sample in Fig. 5.3, except that the asymmetric holes are replaced with square holes of the same surface area. Thin solid lines: transmission of the structure with rectangular holes; dashed lines: transmission of the structure with square holes. The use of red and blue is the same as Fig. 5.3.

illustrated in Fig. 4.22. This suggests that the nature of peak 1, peak 2 and peak 3 are related to the waveguide-cavity resonance, high frequency SPP mode and low frequency SPP mode, respectively. Additionally, we notice that at these transmission peaks, the relative strength of the LSPs excited at the edges of the metallic subwavelength element is larger in the hole-array structure than in the grating structure.

Figure 5.5d shows that E_y component of peak 4 is mainly confined in the void of the metallic hole-array layer. While there exists the significant field enhancement at the edges of the hole (E_z component), the strength of

the E-field near the vicinity of the planar metal film is relatively low. This indicates that the nature of peak 4 is dominated by the excitation of the LSP mode within the structures. In fact, this resonance can lead to the artificial magnetic activity at optical frequencies; an in depth analysis of this phenomenon will be presented in Chapter 7.

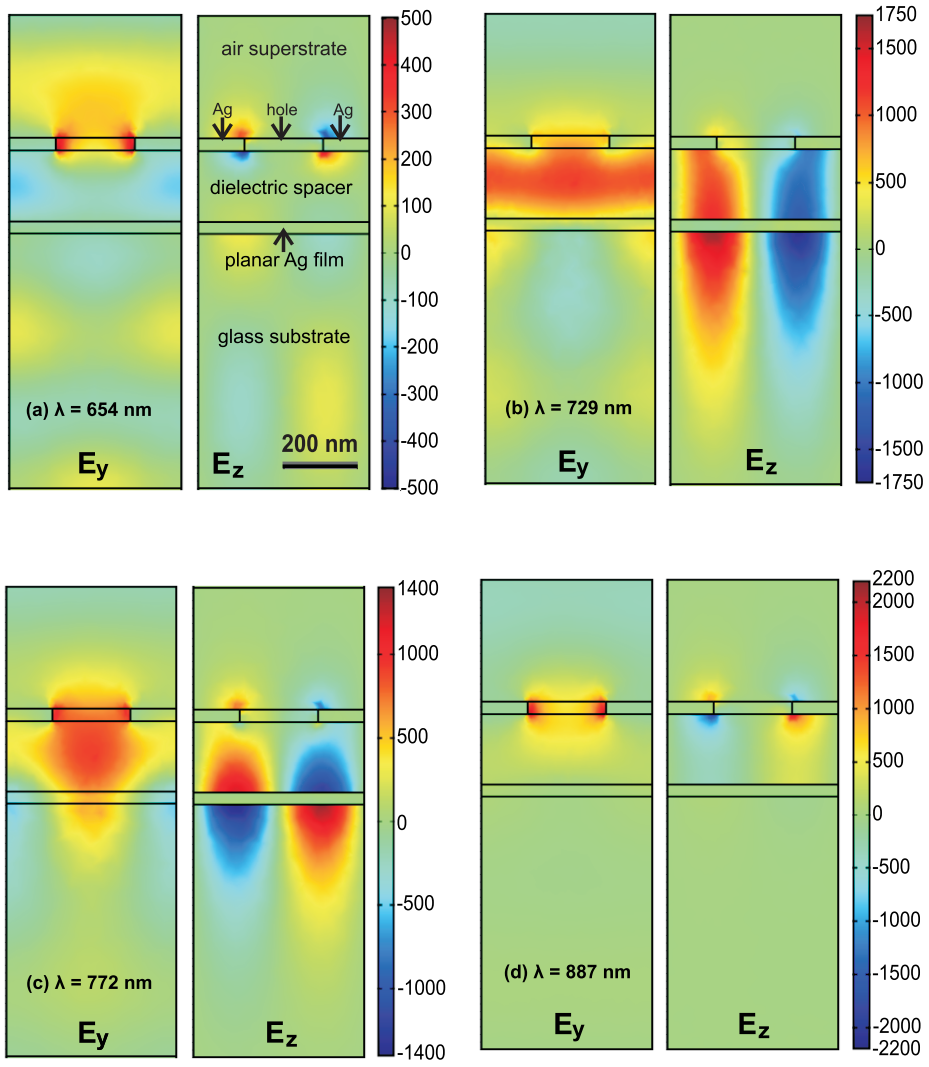

Figure 5.5: E-field distributions of the four peaks in $E_{in}//P_y$ spectrum (solid line) of Fig. 5.3b. Note the scale difference at four different wavelengths.

5.4 Spectral Response of the Structure

In this section, a detailed far-field spectral responses of the hole-array/planar structures to the variations of the lattice constants of the hole arrays, excitation conditions and dimensions of the holes, are analyzed through the experimental investigation and RCWA based simulations. The spectral responses of the structures to the variations of the thicknesses of the planar film and dielectric spacer, and dielectric constants of the spacer and substrate, follow the similar trends as that of the grating/planar structures and these will be omitted in this section.

5.4.1 Effects of Lattice Constants of Hole Arrays

To investigate the relationship between the spectral positions of peaks 2 and 3, and the lattice constant of the hole arrays, we fabricated a set of samples with various lattice constants along two orthogonal directions on fused silica substrates. Using the fused silica minimizes the unwanted effects caused by the asymmetric arrangement of materials surrounding the Ag film, even though both experiments and simulations show that a slight mismatch between the dielectric constants of substrate and spacer (e.g., BK7 glass and fused silica) produces higher transmission than the symmetric arrangement. Fig. 5.6 shows the measured zeroth order transmission spectra of six fabricated samples under linear polarized light, in which the dotted lines and the solid lines represent the spectrum under $E_{in}//P_x$ and $E_{in}//P_y$ excitation, respectively. All the samples have $h_g = 35$ nm, $h_s = 195$ nm and $h_{Ag} = 33$ nm; the values of P_x and P_y on each individual sample are shown in the key of the associated graph.

Figure 5.7 shows the spectral positions of the second and the third peaks

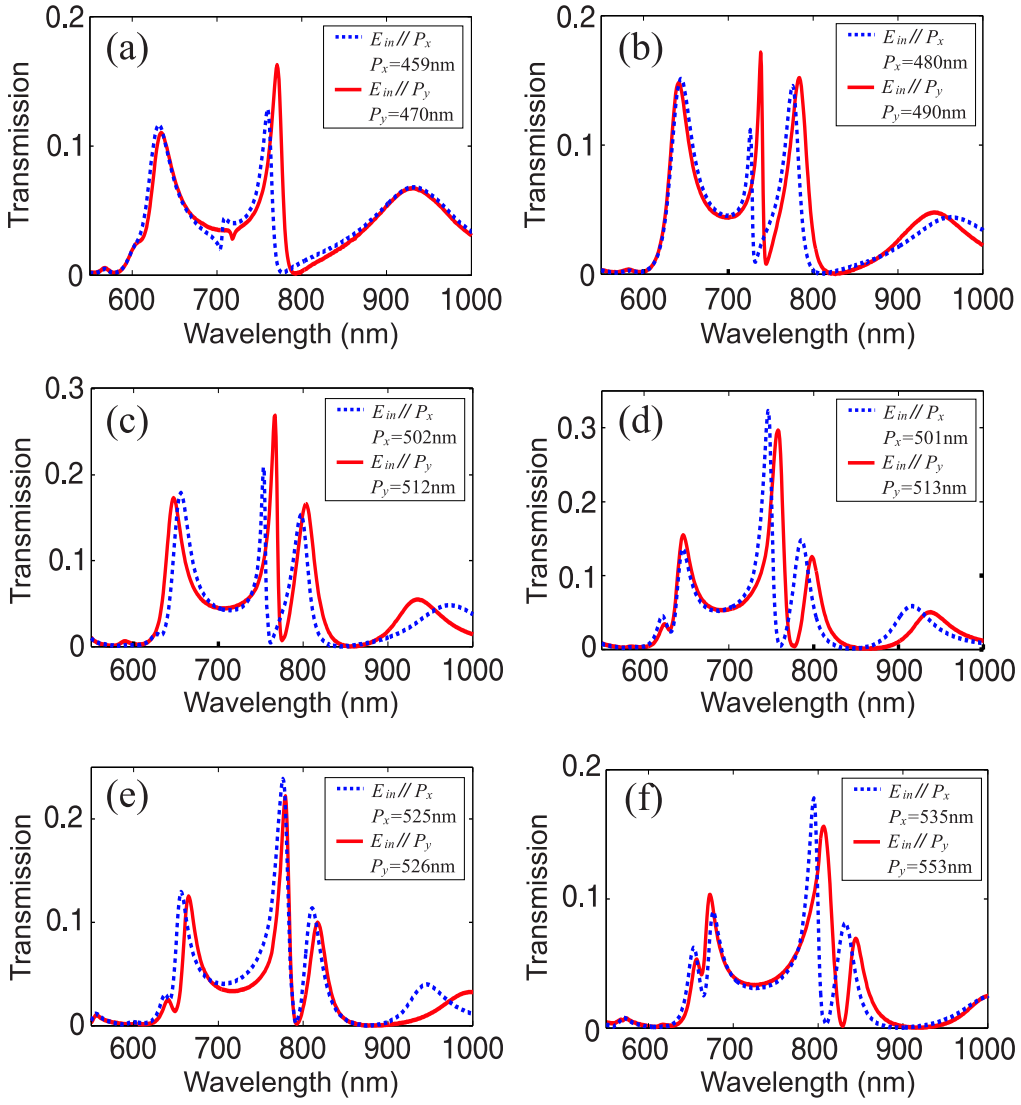

Figure 5.6: Measured zeroth order transmission spectra of six fabricated samples under linear polarized light. All the samples have $h_g = 35$ nm, $h_s = 195$ nm and $h_{Ag} = 33$ nm; the lattice constants of the hole arrays along x- and y-direction are shown on the key of corresponding graph.

extracted from Fig. 5.6, versus the lattice constants of the hole arrays, where $k_{sp} = \frac{2\pi}{P}$ (P is the lattice constant of the hole array) and $\omega = \frac{2\pi}{\lambda}$ (λ is the wavelength at transmission maximum of each peak) Also shown are the theoretical values of the SPP mode on a Ag/SiO_2 single-interface (dotted line), and the ω^+ (dashed line) and ω^- (solid line) modes on a 33-nm-thick Ag film surrounded by fused silica ($n = 1.454$).

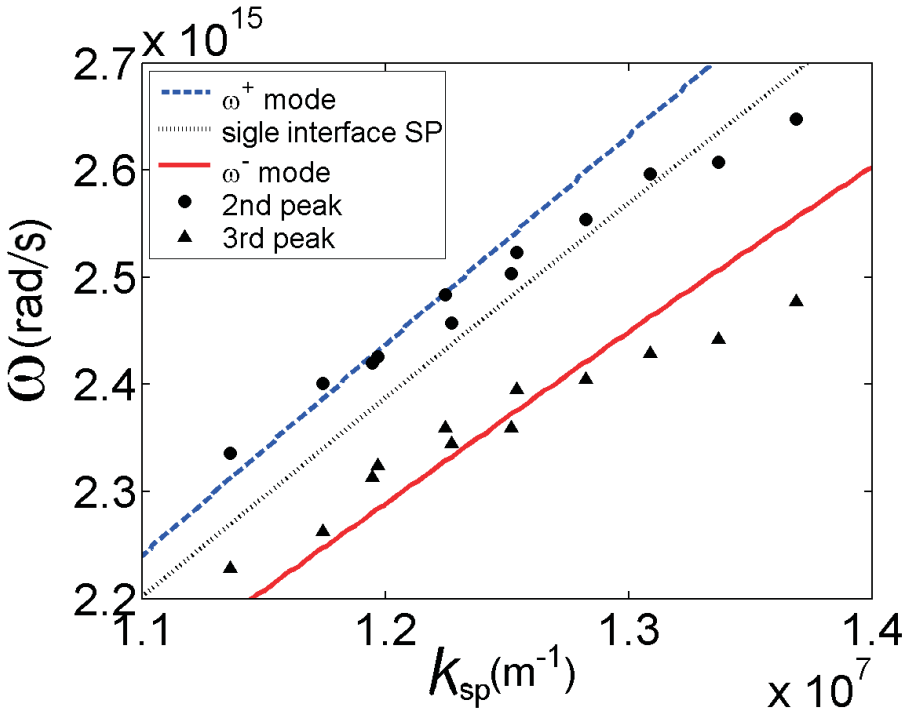

Figure 5.7: Dispersion relations of the 2nd and the 3rd peaks for samples with hole-array periods varying from 450 to 560 nm. Also shown are the theoretical single-interface SPP line and the ω^+ and ω^- lines.

We observe that for samples with higher transmissions (lattice constants 490 – 530 nm, where transmission of the second peak is $> 15\%$), the measured spectral positions agree well with the theoretical calculations. This strongly suggests that the second and the third peaks in the transmission spectra are attributable to the excitation of ω^+ and ω^- modes on the planar Ag

film. For those samples with low transmission (lattice constants are less than 490 nm and peak transmission $< 15\%$), the SPP-related modes show red shifts in the measured frequencies and they exhibit an opposite trend while the lattice constants become larger than the optimal values. This is due to the fact that the calculation above includes only interaction between two SPP modes on the surfaces of the planar Ag films; it does not consider any other coupling effects, such as coupling between the SPP modes, LSP modes and the waveguide-cavity mode, that might exist within the structure. The effects of different modes on the spectral response of the structures will be revealed in Section 5.6.

5.4.2 Effects of Excitation Condition

To closely examine the optical properties of the structure, the spectral response of the sample under different illumination conditions were investigated experimentally. Fig. 5.8 shows the measured zeroth order transmission spectra of the sample used in Fig. 5.6d (which we will call Sample d) under TE- (solid line, E_{in} is perpendicular to the plane of incidence) and TM-polarized (dashed line, E_{in} is parallel to the plane of incidence) light at 5 degrees of incidence; the plane of incidence is parallel to x-z plane shown in Fig. 5.1.

Under TM-polarized incident light, the shape of the spectrum at the wavelengths range between 700 nm to 900 nm (where SPP related transmission peaks occur at normal incidence) undergoes noticeable changes. This observation agrees with the characteristics of the SPP modes, as at oblique incidence SPPs can obtain extra momentum from the incident light. On the other hand, under TE-polarized light the SPP-related transmission peaks remain in the spectrum while varying the angle of incidence. While

this seems to contradict the nature of SPP resonance at the first sight, it can be explained by considering the excitation of the LSPs by the incident light at the edges of the metallic holes, as revealed in Fig. 5.5. The strong near-field enhancement of LSPs extends to the planar Ag film underneath and induces the required surface charges to launch SPP waves on the planar film. Since the wave vector of the incident light and the oscillations of the E-field are out of phase for TE-polarized light, the wavelengths of the SPP modes are unaffected by the incident light and solely depend on the lattice constant of the hole arrays along E_{in} direction – P_y. Indeed, the TE-spectrum here coincides the $E_{in}//P_y$ spectrum shown in Fig. 5.6d.

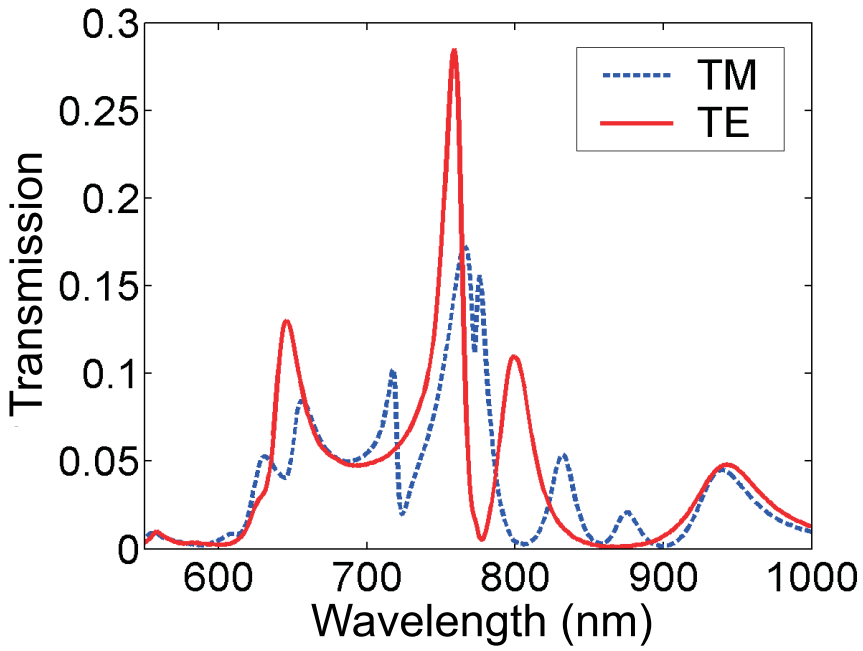

Figure 5.8: Transmission spectra of Sample (d) in Fig. 5.6 under TE- and TM-polarized light at 5 degrees angle of incidence.

The unique response of the structure under TE-polarized light provides us a useful tool to analyze the reflection and absorption response of the sample since in practice it is difficult to measure the reflection spectrum at

normal incidence. Fig. 5.9a and Fig. 5.9b, respectively, shows the measured transmission and reflection spectra of Sample d while illuminating from the hole-array side (dashed lines) and the substrate side (solid lines) under TE-polarized light at 5 degrees angle of incidence. The corresponding absorption spectra of the sample obtained via $A = 1-T-R$ are shown in Fig. 5.9c, where A, T and R are the absorption, transmission and reflection, respectively.

Figure 5.9 reveals that the transmission of the structure is independent of which side the sample is illuminated, as would be expected; in contrast, the reflection and the absorption spectra are rather different for light incident from the hole-array side or from the substrate side. This observation agrees with that reported by Barnes and Gerard [117] [125]. Owing to internal damping of the SPs inside the metal in the process of SP-enhanced transmission, enhanced absorption also exists; the absorption is related to the SPP excitation efficiency and hence, is sensitive to the illumination condition. While illuminating from the hole-array side, the reflectance of both ω^+ and ω^- modes is very low, which indicates excellent excitation efficiency of the SPPs on the planar Ag film under this arrangement. While illuminating from the substrate side, the reflectance of both ω^+ and ω^- modes increases, particularly the ω^- mode. This suggests that the excitation of SPPs on the interfaces of the planar film are weaker under this arrangement. As discussed in Section 2.3.2.2, the field amplitude of the ω^+ (ω^-) mode inside the metal film decreases (increases) as the film thickness reduces. For the thickness of the planar film studied here, the rate of the internal damping of the ω^+ mode is smaller than that of the ω^- mode [10], therefore, the ω^+ mode has lower absorption and narrower linewidth than the ω^- mode.

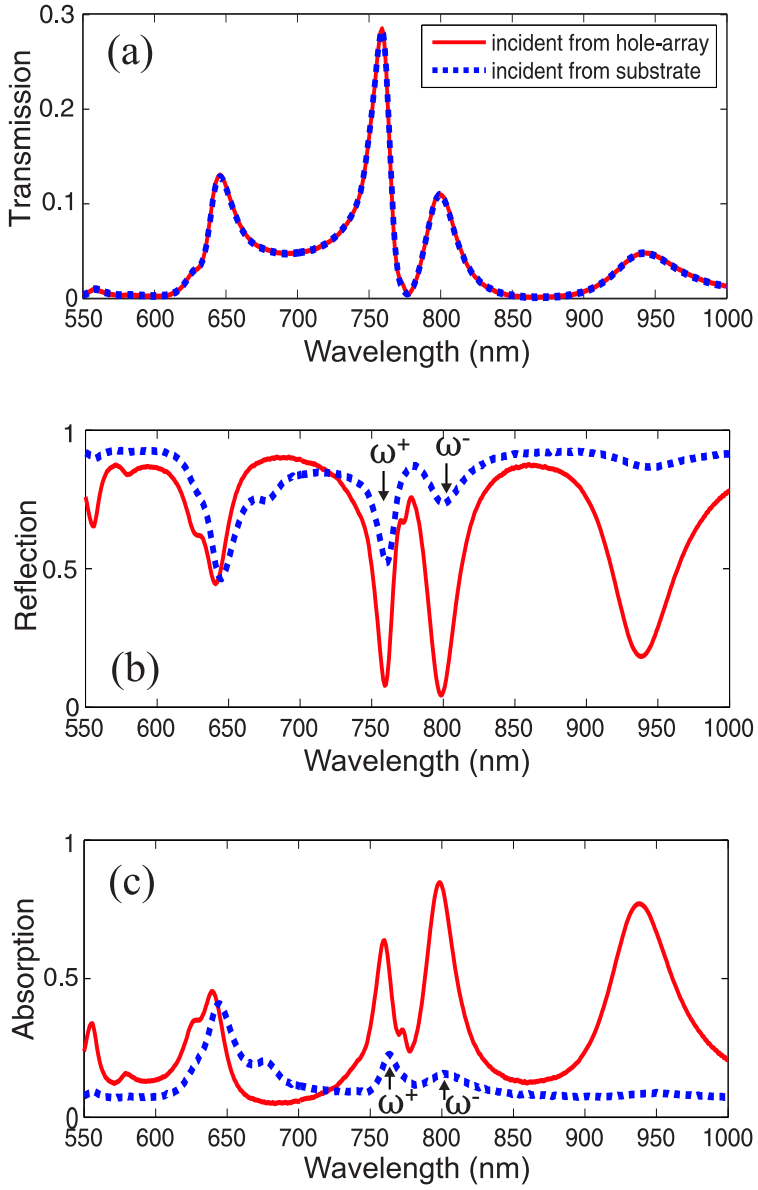

Figure 5.9: (a) Transmission, (b) reflection, and (c) absorption spectra of Sample (d) in Fig. 5.6 while illuminated by TE-polarized light at 5 degrees of incidence. Dotted line represents light incident on the hole-array side; solid line represents light incident on substrate side.

5.4.3 Effects of the Hole Dimensions on the Optical Response of the Structure

The effects of the hole dimensions on the transmission spectra of the structure were briefly discussed in Section 5.3, in which Fig. 5.4 shows that replacing the rectangular hole with the square hole of *same* surface area, the position and the amplitude of both peak 1 and peak 4 are changed; in contrast, the modification has less impact on the peak 2 and peak 3.

Here we examine the effects of varying surface area of the hole on the optical response of the structure. The simulation results obtained from G-Solver are shown in Fig. 5.10. All three structures have $h_g = 35$ nm, $h_s = 195$ nm and $h_{Ag} = 33$ nm, and SiO_2 is used as the substrate and the dielectric spacer. The rest parameters are as follows. In Fig. 5.10a, $P_x = P_y = 490$ nm, $D_x = 0.35P_x$ and $D_y = 0.35P_y$; in Fig. 5.10b, $P_x = P_y = 490$ nm, $D_x = 0.5P_x$ and $D_y = 0.5P_y$; in Fig. 5.10c, $P_x = 400$ nm, $P_y = 490$ nm, $D_x = 0.5P_x$ and $D_y = 0.5P_y$. The E-field of the normally incident light is along y-direction.

Figure 5.10 reveals that reducing the surface area of the hole boosts the strength of SPP-related transmission peaks (peaks 2 and 3); however, this also broadens their linewidth and introduces blue shifts in their spectral positions. We regard this as a consequence of coupling between the LSP mode and the SPP modes within the structure. In periodic subwavelength structures, the observed LSP excitation is indeed a result of the interaction between LSPs on the individual elements of the structure [25]. Therefore, varying the geometry of holes modifies both the frequencies and the strength of the LSP mode. As reported by Degiron *et al.* [128], in the region where the frequencies of the LSP mode and the SPP mode are close together, coupling between the two modes can bring about extraordinary optical transmission for metallic films perforated with periodic subwavelength structures. A

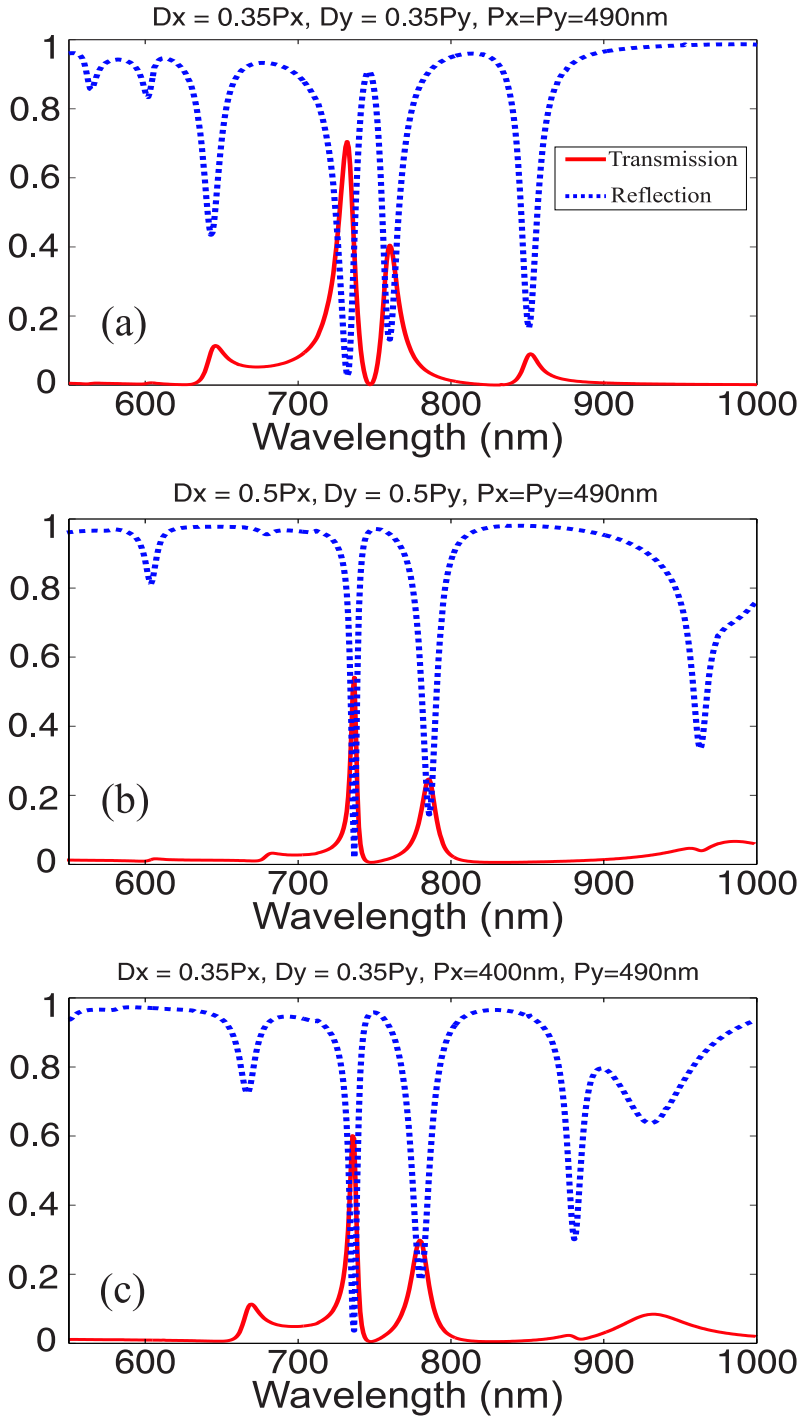

Figure 5.10: Simulation results showing the effects of the hole surface area on the transmission (solid line) and reflection (dotted line) spectra of the structures. Details of the structures are given in the headings of each plot.

similar effect is observed here for our planar metal film structures.

5.5 Comparison of EOT Through Planar Metal Films by Grating Coupling and Hole-array Coupling

Both grating and hole-array structures show the ability to produce SP-assisted extraordinary optical transmission and the overall characteristics of the transmission properties of these two devices are somewhat similar: peak 1, peak 2 and peak 3, respectively, arises from the excitation of the waveguide-cavity mode, the high frequency SPP mode (ω^+) and the low frequency SPP mode (ω^-). There is an additional peak (peak 4) appears in the transmission spectra of the hole-array structures. Simulations (results not shown here) reveal that the characteristics of this peak are closely related to the thickness of the dielectric spacer, as well as the geometries of the hole arrays. However, as opposed to peak 1, peak 4 is mainly affected by the metallic parts of the hole-arrays rather than the voids of the hole arrays.

For SPP-related peaks (peak 2 and peak 3 in the transmission spectra), there are also subtle differences between the spectral features (mainly in the aspects of the amplitude and the linewidth) of two arrangements. This is due to the fact that the excitation of LSPs in the subwavelength structure layer also plays an important role in the extraordinary transmission, as reflected in the Fig 5.8 (TE-spectrum) and Fig. 5.10. Because the LSPs are non-propagating modes and confined to the subwavelength structure, the strength of the excitation and its frequency are determined by the geometries of the subwavelength structure. The field intensity of LSPs is higher in hole arrays

than that in gratings due to the former being a two-dimensional arrangement. This results in enhanced coupling between SPPs and LSPs in the structure with hole-array layer on top; therefore, the transmission efficiencies of the planar metal films coupled to the metallic hole arrays are generally higher than that coupled to the metallic gratings. To further explore this feature, we simulated the transmission spectra of systems consisting of hole-array couplers and grating couplers, the results are shown in Fig. 5.11. The hole-array/planar system (solid line) has the same arrangement as that in Fig. 5.10a; for the grating/planar system (dotted line), the hole-array layer is replaced by a grating layer with duty cycle (metallic line width/period) of 0.65.

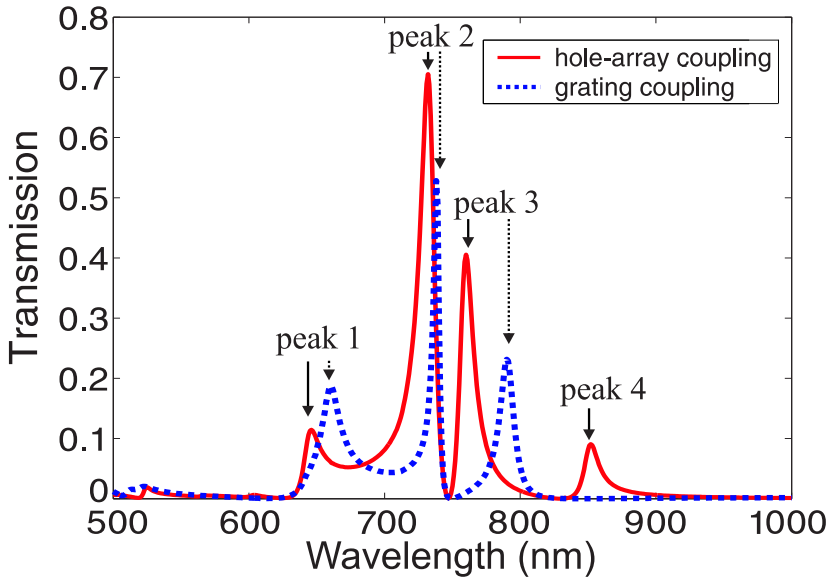

Figure 5.11: Transmission spectra of the systems consist of hole-array coupler (solid line) and grating coupler (dotted line). The hole-array/planar system has the same arrangement as that in Fig. 5.10a and its hole-array layer was replaced by the Ag gratings with DC = 0.65 to form the grating/planar system.

While the transmission efficiency of the high-frequency SPP related peak

is higher for the structure with hole-array layer on top, the linewidth of this mode is broader in such an arrangement. This is due to the additional damping introduced to the system by the two-dimensional metallic layer. There are two damping processes that exist in the structure: the internal damping and radiation damping. The former is due to the finite electrical conductivity of the metal at optical frequencies, its strength increases with the rising intensity of the electric field; the latter is due to scattering agents (surface roughness, subwavelength structures) in the system and its intensity is proportional to the scatterer number. Therefore, the total damping in the structure with the hole-array layer is higher than that in the structure with a grating layer, resulting in the broader linewidth.

5.6 Dispersion Relations of the Structures

To further investigate the mechanism behind the exceptional transmission observed in the multilayer structures studied in this thesis, we systematically analyzed the expected transmission and the absorption of the multilayer structures at normal incidence using G-Solver, in which the periodicity of the patterned layer varies from 300 nm to 900 nm with a step size of 10 nm. In the simulations, all the structures have $h_g = 35$ nm, $h_s = 195$ nm and $h_{Ag} = 33$ nm; $n_d = n_s = 1.454$. For hole-array/planar system, P_y ranges from 300 nm to 900 nm and $D_y = 0.5P_y$; P_x and D_x are fixed to 400 nm and 200 nm, respectively. The E-field of the incident light oscillates along the y-direction ($E_{in}//P_y$). Fixing D_x to 200 nm is to suppresses the waveguide-cavity mode while maintaining the excitation efficiency of SPP modes for the incident light with wavelengths larger than 400 nm, as the critical value for excitation of the waveguide mode through the holes is $D > \lambda/2n^2$ (n=1 for

air here) in the direction perpendicular to the E-field. For grating/planar system, P varies from from 300 nm to 900 nm and $DC = 0.5P$ for all structures.

Figures 5.12 and 5.13, respectively, shows the simulation results for the hole-array/planar system and the grating/planar system. The sub-figures (a), (b) and (c) in each figure corresponds to the transmission, reflection and absorption of the structures, respectively. In these graphs, the calculated dispersion relation of the ω^+ and ω^- modes on the thin Ag films via Equations (2.33) and (2.34) are also shown as the dashed and the solid lines, respectively. The measured spectral position of the peak 2 (circle) and peak 3 (triangle) from the fabricated hole array/planar film samples (as in Fig. 5.7) are highlighted in Fig. 5.12a, and a closer look of this is shown in Fig. 5.14.

We notice that in both Fig. 5.12 and Fig. 5.13, the spectral positions of two transmission (and absorption) peaks in each individual simulation closely follow closely follow ω^+ and ω^- lines, which further confirms the observed peaks derived from excitation of the SPPs modes on the planar Ag film. In Fig. 5.12, there are two hole-array-lattice-constant independent modes at $\omega_1 = 2.75 \times 10^{15}$ rad/s ($\lambda_1 = 685$ nm) and $\omega_2 = 4.10 \times 10^{15}$ rad/s ($\lambda_2 = 460$ nm), whereas in Fig. 5.13 only the low frequency one (ω_1) appears. For both systems, the transmission and absorption of the structures at ω_1 are relatively low compared with its neighborhood, whereas the reflection approaches unity at this frequency. The phase shift of the ω_1 mode after it travels a round trip within the dielectric spacer, which can be calculated via $\theta = 4\pi n_d h_s/\lambda$ [7] (n_d and h_s are the refractive index and the thickness of the dielectric spacer respectively), is $\theta_1 \approx 1\frac{1}{2}\pi$. Considering there is an additional $\frac{1}{2}\pi$ phase different between the propagating waves and the evanescent waves, it is clear that ω_1 is a destructive cavity mode existing in the Fabry-Perot resonator

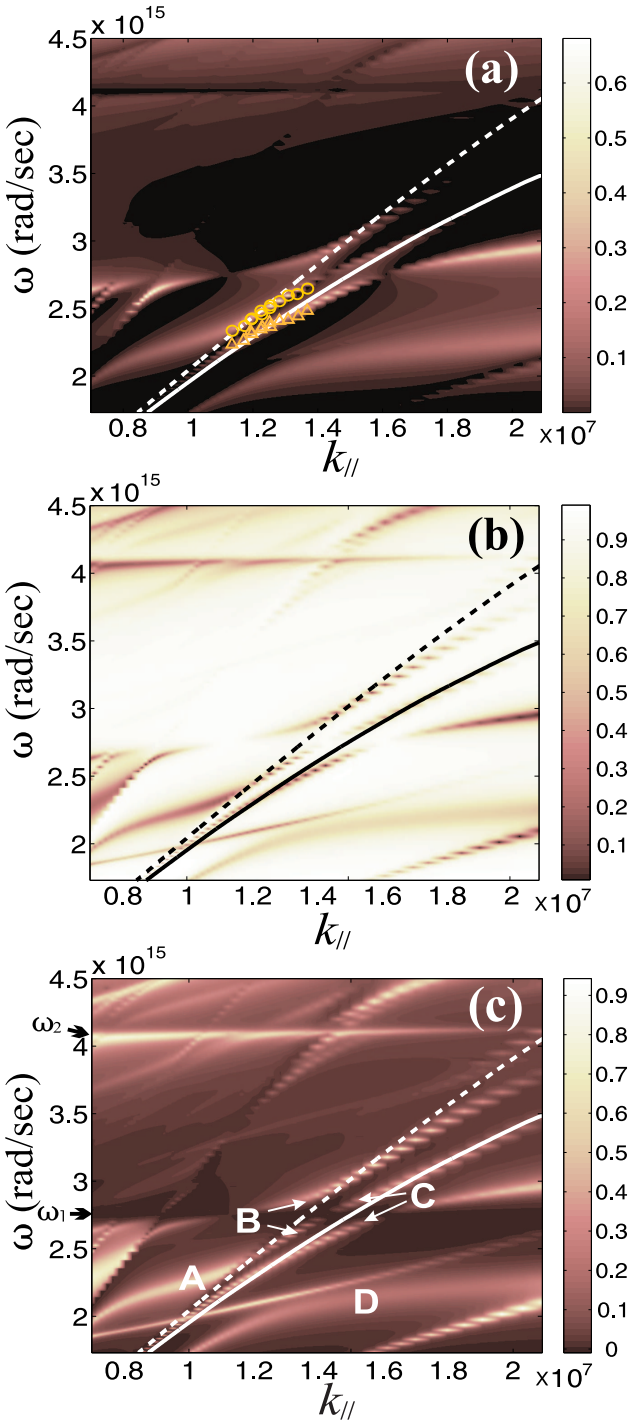

Figure 5.12: (a) Transmission, (b) reflection and (c) absorption spectra simulated for hole array/planar film structures with P_y ranging from 300 nm to 900 nm and $D_y = 0.5P_y$ ($E_{in}//P_y$); P_x and D_x are fixed to 400 nm and 200 nm, respectively. Also shown are the theoretical ω^+ (dotted line) and ω^- line (solid line), and the measured spectral position of the peak 2 (circle) and peak 3 (diamond) from the fabricated samples.

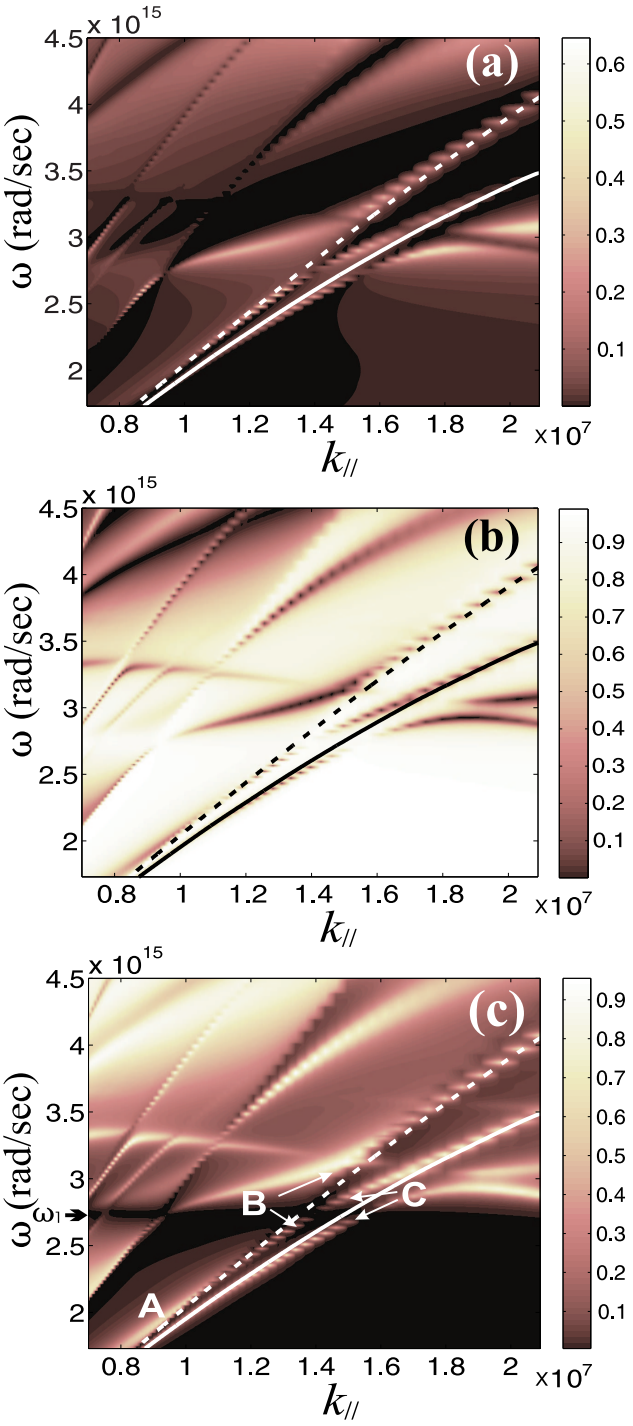

Figure 5.13: (a) Transmission, (b) reflection and (c) absorption spectra simulated for grating/planar film structures with P ranging from 300 nm to 900 nm and $DC = 0.5P$. Also shown are the theoretical ω^+ (dotted line) and ω^- line (solid line).

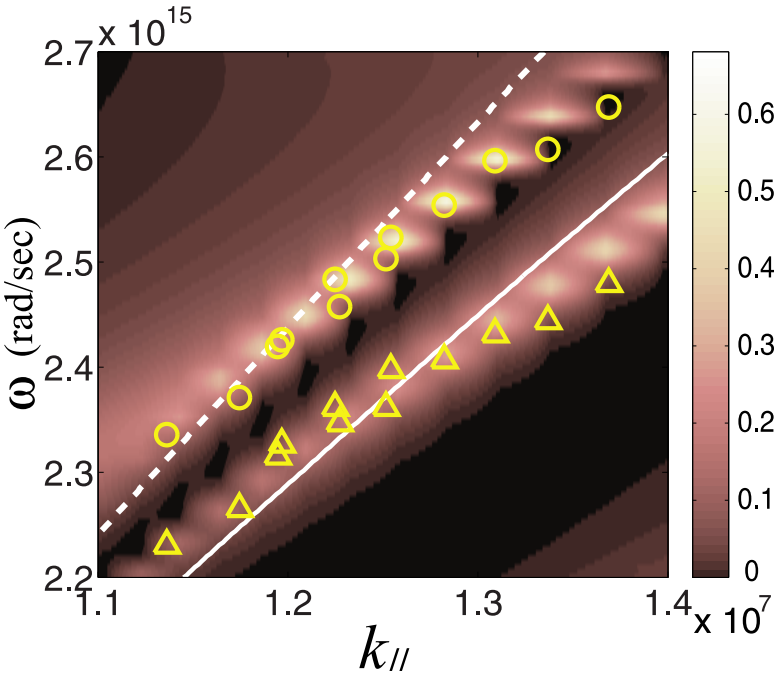

Figure 5.14: A closer look of the measured spectral positions of the peak 2 (circle) and peak 3 (triangle) from the fabricated hole array/planar film samples (as in Fig. 5.7) that are highlighted in Fig. 5.12a.

formed by the patterned metallic layer and the planar film. In the vicinity where this cavity mode intersects the SPP modes, the interaction between them causes the bending of the ω^+ and ω^- modes, as highlighted by "B" and "C" in Fig. 5.12c and Fig. 5.13c. This explains the discrepancy between the measured and calculated spectral positions of ω^+ and ω^- in Fig. 5.7 for samples with smaller lattice constants ($P : 460 - 480$ nm, $k_{sp} :\sim 1.3 \times 10^{-7}$ m^{-1}), as well as the divergence observed in Fig. 4.16 in Chapter 4.

On the other hand, the high-frequency period-independent mode (ω_2 in Fig. 5.12c) does not appear in grating/planar system. In fact, this mode only emerges when P_x and D_x are fixed (e.g., $P_x = 400$ nm and $D_x = 200$ nm here). Simulations (results not shown here) revealed that if the P_x and D_x were increased simultaneously as P_y and D_y (e.g., set $P_x = P_y$ and $D_x =$

$D_y = 0.5P_x$ in the simulations), this mode varnished in the dispersion map. Fig. 5.12 shows that ω_2 mode exhibits very low transmission and reflection, and very high absorption. The above observations suggest that ω_2 mode is related to the excitation of LSPs on the metallic elements between the neighboring holes along the x-direction.

The LSPs can also be excited on the edges of the subwavelength metallic elements – the holes and the gratings. The modes labelled "A" in Fig. 5.12c and Fig. 5.13c are those LSPs generated at the interface of the patterned layer and the SiO_2 spacer. This mode also appears on the dispersion map of the structures that consist of a hole-array-only layer and its spectral response shows high absorption, low reflection and moderate transmission. The shape of this mode in the dispersion diagram is governed by the dimensions of the subwavelength structures, such as dimensions of the holes and the duty cycle of the gratings.

A major difference between the EM responses of the hole-array/planar system and the grating/planar system is that the former supports the artificial magnetic resonance within the structure [155]. This occurs in the region with label "D" in Fig. 5.12c. We will discuss this in detail in Chapter 7.

From Fig. 5.12 and Fig. 5.13, we notice that high transmission efficiencies through planar metal films occur in the vicinity where the mode "A" intersects the SPP modes. This observation agrees with the suggestion of extraordinary transmission being the result of resonant SP-assisted light tunnelling through metal films [123] [125]. The resultant spectra of the multilayer structures are subject to the strength of each mode. If SPP modes dominate the interaction we have very sharp, lattice-constant-dependent transmission peaks with their spectral positions well matching the dispersion relation of SPPs on the planar metal films. Intensifying the effects of the

LSP mode will broaden the linewidth of the SPP peaks, reducing their amplitude and moving them to the high-frequency side of the spectrum. This gives the explanation for the blue shifts observed in the measured spectral position of peak 2 and peak 3 for hole-array/planar samples with larger lattice constants ($P > 530$ nm), as shown in Fig. 5.7. The strength of this LSP mode is strongly dependent on the subwavelength structure topology, which is generally higher in 2D structures (hole arrays) than in 1D structures (gratings). Therefore, it has less impact on the spectral positions of the SPP modes in grating/planar system.

5.7 Summary

The optical properties of the multilayer system consisting of a planar metal film closely coupled to a subwavelength metallic hole-array layer have been investigated. The results further confirm that it is not necessary to have surface modulation on or through the metal film to achieve the extraordinary light transmission; the planar films can also give rise to the exceptional transmission as long as there is some means of generating the necessary SP modes.

The co-existence of the LSP resonance on the metallic subwavelength structures (gratings and holes), and the SPP modes on the planar metal films, are attributable to the unusual transmission properties of the multilayer system studied in this thesis. The structures show high transmission efficiency only in the spectral region where the LSP mode intersects the SPP modes, and the resultant spectra are subject to the strength of each mode. The strength of the LSP resonance excited in subwavelength metallic hole arrays is higher than in metallic gratings, therefore, the hole-array-coupled

planar metal films generally yield higher transmission efficiencies when compared to grating-coupled films. The measured transmission maximum through the hole-array-coupled planar metal film reaches 39% whereas the simulation suggests that the potential transmission could be greater than 70%. The transmission of the multilayer structure fades away in the region where the LSP and the SPP modes become isolated. In this case, the spectral response of the structure shows low transmission, low reflection and high absorption.

We also noted that the influence of the separation between the patterned layer and the planar film on the amplitudes, and the spectral positions, of the period-dependent transmission peaks (peak 2 and peak 3 in the transmission spectra of the structures), even though the latter is mainly dominated by the periodicity of the patterned layer. This implies that the extraordinary transmission through planar films is a result of resonant SP-assisted light tunnelling through metal films, as suggested by several research groups [120] [121] [122] [123].

The crucial difference between SP-assisted transmission observed in the structure studied in this thesis and that in metal films perforated with subwavelength hole arrays [9] lays in the characteristics of the SPP peaks. For the structure studied here, the linewidth of the transmission peak is much narrower (FWHM $<$ 10 nm for both grating and hole-array coupling arrangement) and its center wavelength can be precisely controlled by adjusting the geometric arrangement of the structure, which offers great potential in developing surface-plasmon based optical devices. In fact, the hole-array/planar system not only exhibits extraordinary optical transmission characteristics, but could also produce artificial magnetic resonance at optical frequencies. The metallic and the dielectric elements

along two orthogonal direction within the structure respond to the incident E- and H-field, which act as nano-scale L-C oscillators and give magnetic properties when the incident field is coupled to the L-C resonance. This has opened up a new opportunity to construct the artificial materials having EM properties that can not be accessed in natural materials. After a brief review of recent research activities in engineering artificial EM materials in next chapter, a detailed analysis of achieving optical magnetism utilizing hole-array/planar film system will be presented in Chapter 7.

§ 6. Recent Research Activities in Left-handed Metamaterials

6.1 Introduction

Back in the 1960s, Russian physicist Vector Veselago theoretically investigated the feasibility of substances with simultaneously negative permittivity ε and permeability μ and revealed that such materials are allowed by Maxwell's equations [156]. However, when plane waves propagate inside those hypothetical materials, the orientation of the Poynting vector $\mathbf{S}$, wavevector $\mathbf{k}$, electric field vector $\mathbf{E}$ and magnetic field vector $\mathbf{H}$ are somewhat different from that in the conventional, naturally occurring materials: in the conventional media, both $\mathbf{S}$ and $\mathbf{k}$ are parallel to the right-handed cross-product of $\mathbf{E}$ and $\mathbf{H}$ ($\mathbf{E}\times\mathbf{H}$); in contrast, in those hypothetical media, $\mathbf{S}$ remains parallel to the right-handed $\mathbf{E}\times\mathbf{H}$ while $\mathbf{k}$ becomes parallel to the *left-handed* $\mathbf{E}\times\mathbf{H}$, as illustrated in Fig. 6.1. Veselago therefore referred these hypothetical media as "left-handed" and predicted that they would exhibit some unusual EM properties not existing in any known materials, such as the reversed Snell's law, Doppler shift and Cherenkov radiation.

While a negative ε can be found in some materials, such as metals at the frequencies below plasma frequency, there are no natural materials that

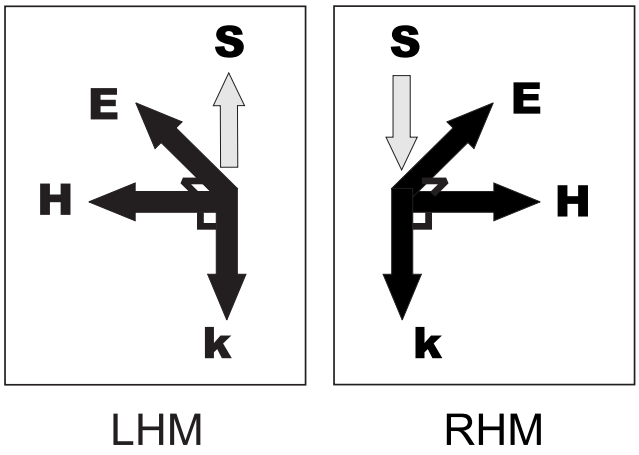

Figure 6.1: Orientation of electric field vector (**E**), magnetic field vector (**H**), wavevector (**k**) and Poynting vector (**S**) in the left-handed media (LHM) and the conventional (right-handed) media (RHM). The wavevector and the Poynting vector are antiparallel in LHM.

exhibit a negative μ at the frequencies above the GHz range. Consequently, Veselago's work received little attention for over 30 years. This changed in 2000, when Smith and co-workers, inspired by the theoretical works of Pendry *et al.* [157] [158], constructed a composite medium – formed by subwavelength arrays of conducting rings and wire – showing simultaneously negative ε and μ in the microwave regime [22]. Smith *et al.* subsequently demonstrated negative refraction at the boundary of this composite [159], which is a result of the double negative behavior as predicted by Veselago, who suggested that one has to choose the negative branch of the square root to properly define the refractive index, i.e., $n = -\sqrt{\varepsilon_r \mu_r}$ [156].

The pioneering work of Smith *et al.* has stimulated great scientific interest in developing so-called *left-handed metamaterials* (LHMs). The term "metamaterials" refers to artificial media consisting of subwavelength details and having EM properties that are impossible or difficult to find in natural materials. Their anomalous functionalities, such as negative refraction, back-

wave propagation, wavefront reshaping, cloaking, etc., open up the possibility to develop new electronic and optical devices which perform beyond the physical limit of the natural materials [160] [161] [162] [163] [164].

The structural scale of metamaterials is generally much smaller than the wavelengths of the impinging EM waves. Consequently, the entire structures act as homogeneous media in which constituent unit cells function as "artificial atoms" to give the effective values of ε and μ. This is the primary factor that differentiates metamaterials from another well-known class of artificial EM media – photonic crystals (PhCs). The periods of PhCs usually are comparable with the wavelength of the incident EM radiation; its underlying physical principles are based on the complex Bragg scattering, which leads to the band formation in the EM spectrum for controlling wave propagation. That is to say, no effective ε and μ can be defined in PhCs, even though they also produce negative refraction like LHMs [165] [166].

It is also worth noting that the conception of utilizing periodic arrays of metallic structures as artificial dielectric media to provide EM properties not easily being accessed in ordinary dielectrics is not a recent phenomenon. In the late 1940s, Kock made lightweight microwave lenses by arranging conducting spheres, disk and stripes periodically to tailor the effective refractive index [167]; his work motivated much research on artificial dielectrics in the microwave region in the 1950s to 1960s [168] [169] [170] [171]. Undoubtedly, these classic works are intimately connected to the recent interest in metamaterials, in which the composites are often based on periodically positioned conducting inclusions and the EM properties are described with homogenized material parameters.

6.2 Homogenization Techniques and Electromagnetic Parameter Retrieval Methods

The notion of an effective medium is intuitively related to the transition from microscopic to macroscopic fields in ordinary homogeneous media. There are two key parameters that describe the EM properties of a material: the electric permittivity ε and the magnetic permeability μ. In natural materials, ε and μ arise from the averaging of the local responding EM fields and current distributions at the atomic or molecular level, where the lattice spacing is much smaller than the wavelength of the impressed field. Correspondingly, in composite media if the applied fields are static or having spatial variation in a degree considerably greater than the scale of the local inhomogeneity, the EM response of the composite can also be determined by the local field averaging, much like a homogeneous material formed by the atoms and molecules [172]. In this sense, the composite is considered as an *effective medium* whose behavior is like a uniaxially anisotropic homogeneous material with effective tensor permittivity ε_{eff} and permeability μ_{eff}:

$$\varepsilon_{eff} = \begin{pmatrix} \varepsilon_{xx} & 0 & 0 \\ 0 & \varepsilon_{yy} & 0 \\ 0 & 0 & \varepsilon_{zz} \end{pmatrix}, \qquad \mu_{eff} = \begin{pmatrix} \mu_{xx} & 0 & 0 \\ 0 & \mu_{yy} & 0 \\ 0 & 0 & \mu_{zz} \end{pmatrix}.$$

If the characterization of the composite is restricted to one of the principal axes under linearly polarized incident EM waves then ε_{eff} and μ_{eff} can be further reduced to scalar numbers.

6.2.1 Conventional Analytical Approach in Composite Homogenization

The conventional analytical approach in homogenizing composites consisting of inclusions embedded in a host medium generally involves the following steps: first, the scattered and the internal fields, respectively, about and within an inclusion are determined by solving Maxwell's equations with appropriate boundary conditions; second, the local fields, charge, and current distribution are averaged over a unit volume containing the inclusion, which yields the effective parameters [173] [174].

The analytical approach can provide the important physical insight into the nature of the EM response of the composite, however, the technique usually becomes increasingly difficult to apply if the inclusion has a complex geometry. Therefore, there exist many well-known effective medium approximations with different forms of mixing formulas, such as Clausius-Mossotti relation, Maxwell-Garnett formula and Bruggeman theory. Each of these formulas is valid under certain preconditions [173]. Furthermore, as metamaterials often involve resonant elements and in general the periodicity is no longer negligible relative to the wavelength of the incident EM waves at IR/optical region, the practice is considered as unreliable or not applicable for characterizing metamaterials [175].

6.2.2 Field-averaging Method

The recent advances in computing capability and EM simulation techniques allow the Maxwell's equations to be solved in virtually any kind of structures without the limitations endured by the classic analytic method, which has greatly benefited our understanding of metamaterials.

The numerical data obtained from the simulation can be used to obtained ε_{eff} and μ_{eff} by averaging of local fields.

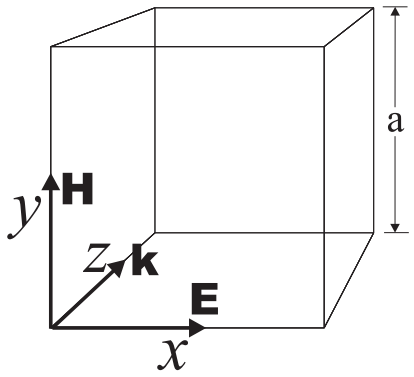

Figure 6.2: Schematic of field orientation in a single cubic unit cell for material parameter retrieval using field-averaging technique.

Consider an incident plane wave which propagates along the z-direction with its **E**- and **H**-fields orient along x- and y-direction, respectively, as illustrated in Fig. (6.2). The material parameters can be calculated from [158] [175]:

$$\begin{aligned} (\varepsilon_{eff})_x &= \frac{\langle D_x \rangle_{yz}}{\varepsilon_o \langle E_x \rangle_x} \cdot \frac{k_y a}{2sin(k_y(a/2))} \\ (\mu_{eff})_y &= \frac{\langle B_y \rangle_{xz}}{\mu_o \langle H_y \rangle_y} \cdot \frac{k_y a}{2sin(k_y(a/2))}. \end{aligned} \tag{6.1}$$

where k_y is the propagation constant of the wave inside the metamaterial, which has to be extracted from the EM simulation software; a is the length of one edge of the cubic unit cell; $\langle D_x \rangle_{yz}$ ($\langle B_y \rangle_{xz}$) corresponds to the averaging of D_x (B_y) over one face of the unit cell in the y-z (x-z) plane; and $\langle E_x \rangle_x$ ($\langle H_y \rangle_y$) corresponds to the averaging of E_x (H_y) over one edge of the cell in the x- (y-) direction.

In addition to the above Surface/Line averaging method, the "field summation" approach which is based on volume and surface averaging, has

also been suggested by some authors [176] [177]. In this case, the effective material parameters can be obtained from:

$$\begin{aligned} (\varepsilon_{eff})_x &= \frac{\langle D_x \rangle_{yz}}{\varepsilon_o \langle E_x \rangle_{xyz}} \\ (\mu_{eff})_y &= \frac{\langle B_y \rangle_{xyz}}{\mu_o \langle H_y \rangle_{yz}} . \end{aligned} \tag{6.2}$$

where $\langle E_x \rangle_{xyz}$ ($\langle B_y \rangle_{xyz}$) is the volume averaging of E_x (B_y) over one unit cell.

Care must be taken when applying surface averaging if the metamaterial has continuous conducting elements passing through that surface. To take account of the contribution of the current flowing between the unit cells in the flux averaging, one could insert a semi-infinite thin dielectric slice in the conductor at the surface of the unit cell so that the current is no longer continuous. In this case, the field averaging would include the depolarized fields within the gap which effectively add in the contribution of the current in the conductor [175].

6.2.3 Inversion Method

Although resolving effective material parameters by field-averaging is feasible for simulations, the technique does not extend to experimental measurements. Since experiments generally reveal only extrinsic quantities (e.g., angle of refraction, transmission and reflection through the metamaterials) rather than give a comprehensive picture of the field distributions within the media. As an alternative to the field-averaging approach, the inversion method retrieves the effective material parameters from complex transmission and reflection coefficients (t and r) of the EM waves propagating through a finite slab of metamaterials at normal incidence [178], which is practicable for both simulations and measurements.

The inversion method is derived from scattering parameter retrieval [178] [179] – an established technique for the experimental characterization of material parameters at microwave frequencies [180]. Scattering parameters (also called S-parameters) are two-port network parameters describing the waves transmission and reflection by a linear two-port network. Fig. 6.3 schematically illustrates a S-parameter measurement. When waves incident perpendicularly on Port 1, S_{11} is equivalent to the input complex reflection coefficient and S_{21} is equivalent to the forward complex transmission coefficient; likewise, by placing the source at Port 2, S_{22} is equivalent to the output complex reflection coefficient and S_{12} is equivalent to the reverse complex transmission coefficient. For a slab of homogeneous material in vacuum, $S_{11} = S_{22} = r$ and $S_{21} = S_{12} = t' = te^{ik_o d}$, where t' is the normalized transmission coefficient taking into account the additional vacuum-phase compensation, through distance d, $k_0 d$.

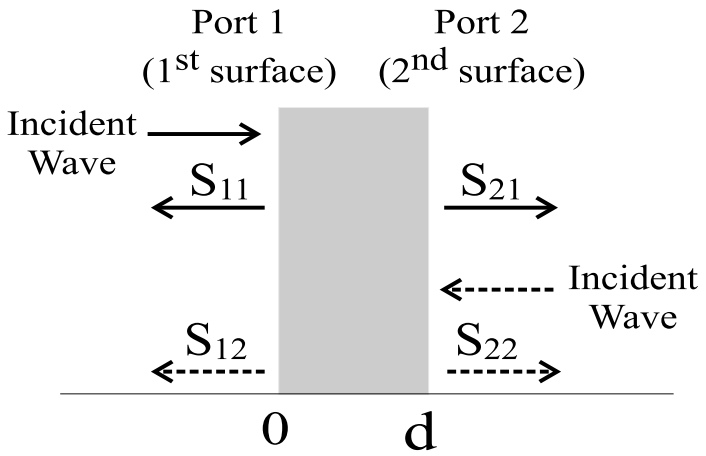

Figure 6.3: S-parameters for a 2-port network consists of a slab of homogeneous materials of thickness d in vacuum. For a plane wave incident perpendicularly on the slab, $S_{11} = S_{22} = r$ and $S_{21} = S_{12} = te^{ik_o d} = t'$, where $k_o = \omega/c$ is the wavenumber of the incident wave.

Assuming the wave incident on the first surface (Port 1) of the slab in

Fig. 6.3, the fields on either side of the slab are related by the transfer matrix **T** via:

$$\begin{pmatrix} E_2 \\ H_2 \end{pmatrix} = \mathbf{T} \begin{pmatrix} E_1 \\ H_1 \end{pmatrix} = \begin{pmatrix} \cos(nk_o d) & -iZ\sin(nk_o d) \\ -iZ^{-1}\sin(nk_o d) & \cos(nk_o d) \end{pmatrix} \begin{pmatrix} E_1 \\ H_1 \end{pmatrix}, \quad (6.3)$$

where n and Z is the refractive index and the wave impedance of the slab, respectively. Using the interrelation between the S-parameter matrix and the transfer matrix [181], S-parameters can be expressed in terms of the elements in the **T**-matrix, which can be inverted to find n and Z through the relations [178]:

$$\cos(nk_o d) = \frac{1 - r^2 + t'^2}{2t'} \quad (6.4)$$

and

$$Z = \sqrt{\frac{(1+r)^2 - t'^2}{(1-r)^2 - t'^2}}\,, \quad (6.5)$$

with the requirement that $\mathrm{Im}(n) > 0$ and $\mathrm{Re}(Z) > 0$ for passive and absorptive media. If the wavelength within the metamaterial is not much larger than the slab thickness, there may exist an ambiguity in determining $\mathrm{Re}(n)$ from the inversion of the cosine function in Equation (6.4), which could be resolved by measuring more than one thickness of the samples to find the consistent value of n [178]. Alternatively, some authors [182] have suggested to use a Taylor expansion approach together with the fact that the n is a continuous function of frequency to accurately determine the value of $\mathrm{Re}(n)$.

Once the values of n and Z are obtained, the ε_{eff} and the μ_{eff} can be calculated by using:

$$\varepsilon_{eff} = \frac{n}{Z} \quad (6.6)$$

and

$$\mu_{eff} = nZ\,. \quad (6.7)$$

Owing to its versatility and simplicity, the inversion method has been extensively used in the study of LHMs, even though it provides limited physical insight into the nature of the LHMs. In particular, the approach is considered to be a rigorous method for the retrieval of constitutive effective parameters from experimental data, and has been employed by different groups [183] [184] in the experimental demonstration of negative-index metamaterials at optical region.

6.2.4 Phase Velocity Calculation

Phase velocity calculation provides another means of analyzing the negative refraction behavior of the metamaterials [185] [175] [186], it can be applied for both simulation and measurement data. The technique is rather straightforward: if the phase change $\Delta\phi$ of the waves propagating through a slab of an effective homogeneous material of thickness d is known, the real part of the effective refractive index, n', can then be determined from

$$n' = \frac{\Delta\phi}{k_o d}\,. \tag{6.8}$$

If the field distribution within the metamaterial can be obtained from the simulations, the wave impedance can be calculated through

$$Z = \frac{\langle E\rangle}{\langle H\rangle}\,, \tag{6.9}$$

where $\langle\ \rangle$ denotes the volume averaging of the relevant field.

Applying the results from Equations (6.8) and (6.9) to Equations (6.6) and (6.7) yields the real part of the ε_{eff} and μ_{eff}.

6.2.5 Validity of the Effective Parameters

The techniques for the retrieval of the constitutive parameters of the metamaterials discussed above are based on the assumption that they can

be treated as effective homogeneous materials. The constitutive parameters of causal materials are generally complex functions of the frequency, that is, it is necessary that the effect permittivity and permeability of the LHM has the form $\varepsilon_{eff}(\omega) = \varepsilon'_{eff}(\omega) + i\varepsilon''_{eff}(\omega)$ and $\mu_{eff}(\omega) = \mu'_{eff}(\omega) + i\mu''_{eff}(\omega)$, respectively [174].

The principle of the causality (i.e., no effect precedes its cause) requires that the real and the imaginary parts of the constitutive parameters must satisfy Kramers-Kronig relations [187]. Therefore, while there is no fundamental objection to ε'_{eff} and μ'_{eff} being negative, it is a common belief that ε''_{eff} and μ''_{eff} should be positive in passive media as these components are associated with transmission loss within the media. Nevertheless, the retrieval process from simulation data can also uncover some unexpected effects, such as the imaginary part of either ε''_{eff} or μ''_{eff} being negative in certain frequency regions [188] [189] [190].

Some authors [190] have proposed that this is an intrinsic property of a metamaterial which originate from the finite spatial periodicity of the medium. Because the dissipated energy is given as a sum

$$W = \frac{1}{4\pi} \int d\omega\omega[\varepsilon''_{eff}(\omega)|E(\omega)|^2 + \mu''_{eff}(\omega)|H(\omega)|^2] \,, \tag{6.10}$$

the condition $W > 0$ does not require that ε''_{eff} and μ''_{eff} must be simultaneously positive. However, not all agree with this suggestion [191] [192]. More recently, it has been suggested [185] that the anomalous signs in the imaginary part of the effective material parameters are caused when the contribution from higher order evanescent modes outweighs the fundamental propagation mode within the periodic metamaterial. Therefore, in these frequency regions the metamaterial can not be described by the complex transmission and reflection coefficients based approach.

The existence of both conductive and capacitive elements (metals and

dielectrics) within the metamaterials can give rise to strong resonance to the incident EM-fields, hence one needs to be very careful when applying the homogenization approach to characterize the EM properties of the metamaterial, particularly in the region where the periodicity becomes not negligible to the free-space wavelength. Recently, it has been suggested [193] that effective behavior of metamaterials can be decomposed into an effective behavior of the constituents of the metamaterials and an explicit contribution of the periodicity. Homogeneous media approaches can only be justified in the low-frequency limit; at the frequencies where the vacuum wavelength becomes comparable to the size of the unit cell, one should use the periodic effective medium approach for the description and interpretation of real metamaterials.

6.3 Single-negative and Double-negative Left-handed Metamaterials

The effective refractive index of the metamaterials is defined as

$$n_{eff}(\omega) = n'_{eff} + in''_{eff} \tag{6.11}$$

$$= \pm\sqrt{(\varepsilon'_{eff} + i\varepsilon''_{eff})(\mu'_{eff} + i\mu''_{eff})}\,. \tag{6.12}$$

To achieve a negative refractive index in a passive medium, the values of ε_{eff} and μ_{eff} must satisfy [194]:

$$\mu''_{eff}\varepsilon'_{eff} + \mu'_{eff}\varepsilon''_{eff} < 0 \tag{6.13}$$

and

$$\varepsilon'_{eff}|\mu_{eff}| + \mu'_{eff}|\varepsilon_{eff}| < 0\,, \tag{6.14}$$

in which the first inequality ensures the sign on the right-hand-side of Equation (6.12) obeys the principle of causality, i.e., $n''_{eff} > 0$, and the second inequality warrants $n'_{eff} < 0$.

Equations (6.13) and (6.14) imply that it is possible to have $n'_{eff} < 0$ without ε'_{eff} and μ'_{eff} being simultaneously negative. LHMs with such property are termed "single-negative LHMs" (SN-LHMs) to distinguish them from those having simultaneously $\varepsilon'_{eff} < 0$ and $\mu'_{eff} < 0$ – also called "double-negative LHMs" (DN-LHMs). The existence of SN-LHMs has been experimentally observed in the microwave [195], near-infrared [183] and visible [196] regions. They generally occur when ε''_{eff} and μ''_{eff} are sufficiently large. Consequently, SN-LHM are relatively lossy when compared with DN-LHMs.

The complex natural of ε_{eff} and μ_{eff} implies that the resulting n_{eff} of LHMs is generally complex as well. To realize the potential of LHMs (e.g., perfect lensing) it is necessary to have $n'_{eff} \gg n''_{eff}$. Therefore, the figure of merit (FOM), which is defined as

$$\text{FOM} = -\frac{n'_{eff}}{n''_{eff}}\,, \tag{6.15}$$

has been introduced to characterize the performance of the LHMs.

6.4 Left-handed Metamaterials at Optical Frequencies

Perhaps for researchers in the field of optics, the most appealing feature of the LHMs is the negative refraction. This offers the potential of focusing light below the diffraction limit [21], which will have great impacts on future optical lithography, optical storage, optical communications, photonic

circuits, etc.

While some noble metals have negative ε at optical/IR frequencies, there are no natural materials that exhibit magnetic resonance, let alone negative μ, at frequencies above the GHz range. This is because the physical origin of the magnetic activity – microscopic magnetic dipoles – requires either the flow of orbital currents or the unpaired electron spins, which generally are weakly present in natural materials at higher frequencies. Therefore, a key aspect in developing optical LHMs is to achieve optical magnetism.

6.4.1 Downsizing Split Ring Resonators

Utilizing artificially patterned metallic subwavelength-structures to achieve strong magnetic resonance at GHz frequencies was initially suggested by Pendry *et al.* in 1999 [158]. Among the several designs proposed in this paper, arrays of double-split-ring resonators (DSRRs) were adopted by Smith *et al.* in the first experimental demonstration of LHMs in the microwave region [22].

A DSRR consists of two subwavelength concentric split-rings facing in opposite directions, as illustrated in Fig. 6.4. The structure can be considered as an effective electronic circuit, in which the metallic rings act as the inductive element and the two slits as well as the gap between the rings serve as the capacitive element. When a time-varying magnetic field incident perpendicular to the plane of the rings, electric current flow can be induced in the metallic rings. The combination of the inductive element and the capacitive element introduces a resonance into the effective circuit, resulting in an increased current at the resonant frequency ω_o, and subsequently, an enhanced magnetic dipole moment. By patterning DSRRs in a periodic fashion, the entire structure acts as an effective magnetic medium. At

frequencies well below ω_o, the magnetic dipole response is in phase with the applied the H-field with its strength increasing with frequency, resulting in $\mu'_{eff} > 1$. The phase of the magnetic dipole response begins to lag as the frequency of the incident field approaches ω_o and its will eventually become completely out of the phase with the incident field at the frequencies above ω_o, resulting in $\mu'_{eff} < 1$ (which may include $\mu'_{eff} < 0$).

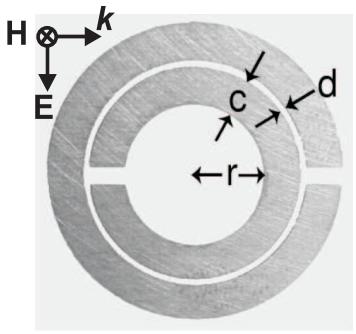

Figure 6.4: A single copper DSRR created on a circuit board as a magnetic atom for realizing negative μ_{eff} in a left-handed composite. The DSRR has its resonance at about 4.845 GHz with $c = 0.8$ mm, $d = 0.2$ mm and $r = 1.5$ mm [22].

The resonant frequency of a LC circuit is given by [197]

$$\omega_{LC} = \frac{1}{\sqrt{LC}} \propto \frac{1}{\text{size of SRR}} . \tag{6.16}$$

Therefore, a straightforward method to increase magnetic resonant frequency is to decrease the size of the DSRRs. Using the array of microscaled DSRRs, Yen *et al.* [198] demonstrated the magnetic resonance at the frequency around 1THz ($\lambda = 300$ μm). By simplifying the geometry of the split-ring resonator (SRR) from DSRRs to single-split-ring resonators (SSRRs) [199] to cut-wire pairs [200], as shown in Fig. 6.5, Linden *et al.* pushed the magnetic resonance from infrared region ($\lambda = 3$ μm) down to the optical communication wavelength ($\lambda = 1.5$ μm).

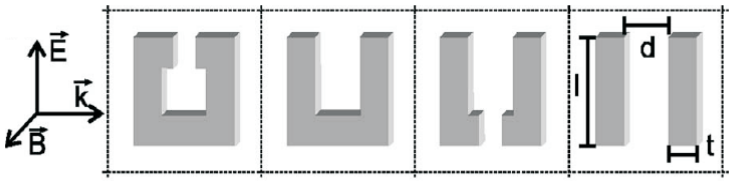

Figure 6.5: Schematic of the adiabatic transition of magnetic atoms of optical metamaterials from SSRRs (left) to cut-wire pairs (right) [200]. Using 150-nm-thick cut-wires with t = 20 nm, d = 80 nm, l =150 nm, and periods of 500 nm and 1050 nm along E- and H-field, respectively, $\mu'_{eff} < 0$ has been realized at $\lambda = 1.5$ μm.

Equation (6.16) indicates that the magnetic resonant frequency scales reciprocally with the structural size. However, this holds only on condition that the metal acts as an ideal metal. As the incident EM waves approach high frequencies (e.g.optical frequencies), the kinetic energy of the electrons in the metallic components of the SRRs cannot be neglected anymore in comparison with the magnetic energy. As a result, there exists an additional inductance, called kinetic inductance L_{kin}, at high frequencies. L_{kin} has the form [201]

$$L_{kin} = \frac{l'}{S'\omega_p^2\varepsilon_o} \tag{6.17}$$

where l' is a constant related to the dimensions of the SRR; S' is the effective cross-section of the ring, which is smaller than the geometric cross-section due to the skin effect of the metal at high frequencies; ω_p is the plasma frequency of the metal. Consequently, the resonant frequency of the SRRs becomes

$$\omega_{LC} = \frac{1}{\sqrt{(L + L_{kin})C}} \propto \frac{1}{\sqrt{(\text{size of SRR})^2 + constant}}\,. \tag{6.18}$$

The constant term in the denominator of Equation (6.18) arises from L_{kin}. It implies the existence of the saturation in the magnetic response of the SRRs due to the skin depth and the plasmon resonances of the metal. Although one

could increase the value of the capacitance in the LC circuit through adding more capacitative gaps to the SRR design to increase the resonance frequency, the scaling-down approach would eventually break down [201] and it has been reported that this limit is at around 900 nm incident wavelength [202].

6.4.2 LSP Resonance Based LC Resonators

At optical frequencies metallic nanostructures are often referred to as plasmonic structures owing to their ability of supporting surface plasmon excitation. This feature indeed opens up a new means of realizing optical LHMs.

It has been suggested by Podolskiy *et al.* [203] [204] that a composite of metal nanowires arranged into parallel pairs, as shown in Fig. 6.6, can have negative effective permeability and permittivity. In such a system, the excitation of the symmetric and asymmetric localized surface plasmon (LSP) resonances, respectively, in the nanorod pairs give rise to the electric and magnetic responses of the structure. An alternative way of looking at this is to consider the directions of the currents generated by the incident EM-waves in the rods [205]. The time-varying E-field parallel to both rods induces parallel currents (black arrows in Fig. 6.6a) in both rods and the generated dipole moment gives rise to the ε_{eff}. The time-varying H-field perpendicular to the pair induces antiparallel currents in the rods (black arrows in Fig. 6.6b), which is closed through the displacement current at the end of the two rods (red arrows in Fig. 6.6b). The inductance (current loop) and the capacitance (dielectric gap between the rods) in the nanorod pairs will lead to LC resonance at certain frequencies and yield a strong magnetic response.

Figure 6.7a shows a field-emission scanning electron microscope image

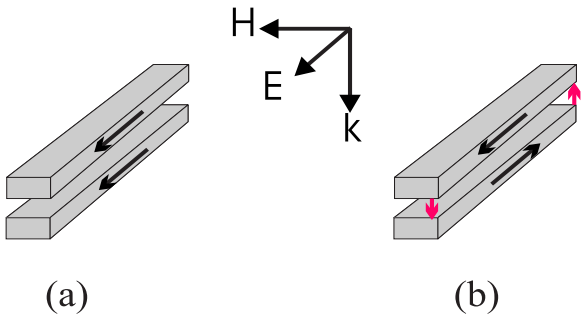

Figure 6.6: EM response in a paired metallic nanorods. (a) electric response, (b) magnetic response. The arrows represent the direction of the induced currents in the rods.

of a double-periodic array of gold nanorods pairs fabricated by Shalaev *et al.* to achieve negative refractive index in 2005 [184]. The structure shows $n'_{eff} = -0.3$ with FOM = 0.1 at the optical communication wavelength of 1.5 μm. At the same time, S. Zhang *et al.* reported the experimental observation of negative refractive index using transversely structured metal-dielectric-metal multilayer system (Fig. 6.7b) [183]. They obtained $n'_{eff} = -2$ with FOM = 0.5 at the 2 μm wavelength. Zhang's structure can be thought as a reversed system of the array of paired nanorods, which can be roughly divided into two functional parts: the elements along the incident E-field give the electric response and that along the incident H-field provide the magnetic response. Zhang and co-workers subsequently suggested an optical impedance matching design to improve the transmission of LHMs [206], which was adopted by Dolling *et al.* to construct a DN-LHM with FOM of 3 at $\lambda = 1.4$ μm wavelength (Fig. 6.7c) [207]; and more recently, $n'_{eff} = -0.6$ at the red end of the visible spectrum ($\lambda = 780$ nm) has been demonstrated by further miniaturizing this structure [208].

As an alternative to the stacked elements, Grigorenko and co-workers used pairs of in-plane gold nanopillars (Fig. 6.7d) with plasmon resonance

at visible part of spectrum to achieve $\mu'_{eff} < 0$ [209], and $n'_{eff} = -0.7$ with FOM = 0.4 [210], at green-light wavelengths. However, these results were questioned by others [211], as they were obtained from the reflection intensity measurements only rather than from the complex transmission and reflection coefficient measurements, in which the latter is considered to be a rigorous method for retrieving effective material parameters.

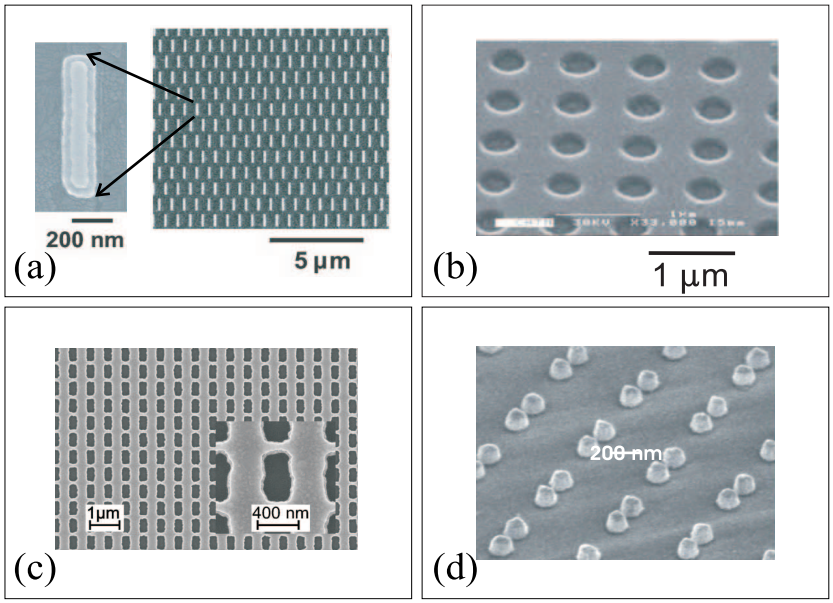

Figure 6.7: Varies geometries presented in the experimental demonstration of optical LHMs. (a) Double-periodic array of paired gold nanorods [184]. (b) Metal-dielectric-metal multilayer consists of transversely structured hole arrays [183]. (c) Structure developed from (b) with an improved FOM due to matched optical impedance [207]. (c) Array of paired gold nanopillars [210].

6.4.3 Coupled Planar/Patterned Multilayer Structures

The resonance frequency and strength of LSP based optical LC resonantors are strongly affected by the geometries of the constituent

units. The requirement of using paired nanoscale elements in the unit cell further raises the complexity involved in fabrication. Therefore, coupled planar/patterned metallic multilayer structures have been considered as a simple alternative to the system consisting of paired elements.

The existence of magnetic activities in the planar/patterned metallic multilayer structures has been revealed by several research groups [212] [204] [53]. This is also one of the topics investigated in the work of this thesis [155]. The magnetic response within such structures is caused by the excitation of LSP resonance in the patterned layer. The strong local field enhancement from LSP excitation induces an "image" of the patterned layer inside the planar metal, the system can therefore be viewed as a pair of patterned layers discussed above.

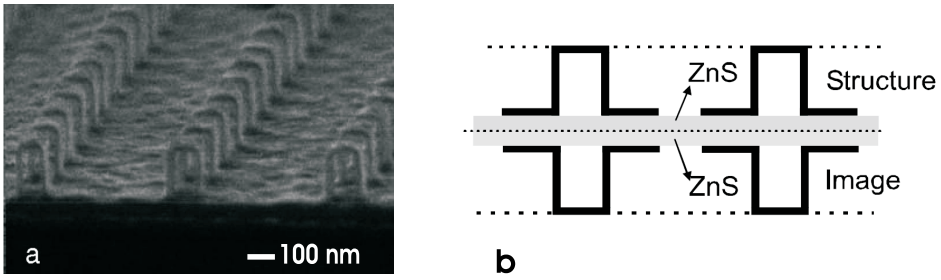

Figure 6.8: (a) SEM image of the arrays of 2D staple-shaped nanostructures shows magnetic response at 65 THz. (b) The equivalent SRR structure formed by the top staple structure and its image in the metal [212].

Achieving magnetic resonance using planar/patterned metallic multilayer was demonstrated experimentally by S. Zhang *et al.* at mid-infrared frequencies [212]. As shown in Fig. 6.8a, the structure consists of an array of Au "staples" and a planar metallic mirror separated by a ZnS dielectric layer. Each staple and its image mirrored in the metal surface can be viewed as a pair of SRRs, which forms an LC circuit (Fig. 6.8b) and gives rise to negative permeability at 65 THz.

6.4.4 Subwavelength Plasmonic Crystals

Subwavelength plasmonic crystals (SPCs) present a rather different approach to the above LC resonator based designs. Their operation is based on the *electrostatic resonances* of periodic arrays of closed spaced metallic elements [213]. As the size of the metallic feature in SPCs can be smaller than the skin depth of the metal in such system, the technique could open interesting venues for realizing left-handed metamaterials at optical frequencies.

Utilizing SPCs to achieve optical magnetism was suggested by Shvets and Urzhumov [213] [214] [215]. As the size of the metallic feature approaches the skin depth of the metal, plasmonic (electrostatic) resonances dominate over the geometric (LC) resonances. When the operation frequency approaches the higher-multipole electrostatic resonances, a non-vanishing magnetic moment will be produced inside each inclusion due to the higher-multipole electrostatic resonances of its neighbours, which gives rise to the magnetic properties of the SPCs.

For regularly shaped inclusions (e.g., nanospheres and nanowires), strong electrostatic resonances occur for $-2 < \varepsilon'_m(\omega) < -1$, where $\varepsilon'_m(\omega)$ is the real part of the relative permittivity of the metal from which the inclusion is made [215]. As the losses of the metals (determined by $\mid \varepsilon''_m(\omega)/\varepsilon'_m(\omega)\mid$) are generally large for the frequencies corresponding to $-2 < \varepsilon'_m(\omega) < -1$, there is a considerable interest to design SPCs that resonate at the frequencies such that $\varepsilon'_m(\omega) \ll 1$, because of the smaller value of $\mid \varepsilon''_m(\omega)/\varepsilon'_m(\omega)\mid$ at these frequencies. To achieve this, various structures have recently been suggested to serve as the elementary building blocks of the SPCs, including: thin metallic stripe pairs [215], horseshoe-shaped nanostructures [216] and nanoparticles arranged in a circular pattern to form a single subwavelength

"ring inclusion" [217]. The work of this thesis also involves the design of optical DN-LHMs using single-layer plasmonic crystals, the details of which are presented in Chapter 7.

6.5 Summary

In this chapter the fundamental concept of LHMs was described, the common techniques for the retrieval of material parameters based on the effective medium theory were presented and the validity of retrieved results, such as anomalous signs in the imaginary part of the effective material parameters, were discussed. The current development of optical LHMs was briefly reviewed. While the existence of localized surface plasmon resonance in metallic nanostructures opens a new means to develop LHMs in optical region, the design, and more importantly the fabrication, of LHMs at high frequency side of spectrum still remain challenging tasks. Therefore, an important aspect in the work of this thesis is to explore simple alternatives for easy fabrication of LHMs at optical frequencies.

§ 7. New Designs for Optical Metamaterials

7.1 Introduction

Surface plasmon resonance is considered to be an effective tool in designing metamaterials operating at optical wavelengths [24]. In this chapter, we direct our understanding of the physics underpinning SP resonance, which were obtained from the investigation of EOT through planar/patterned multilayer structure, towards the design of optical metamaterials.

We present the numerical study of two new structures as optical metamaterials. One is a magnetic metamaterial formed from a planar/patterned multilayer structure, which is a LSP-based optical L-C resonator; another one is a double-negative metamaterial using single layer plasmonic structure, which utilizes the existence of electrostatic (plasmon) resonances within the periodically arranged subwavelength metallic particles. In both cases, structures with only a single patterned layer have been considered to allow for simpler fabrication.

7.2 Optical Magnetism Using Planar/Patterned Multilayers

A major difficulty in realizing optical LHMs is to achieve a strong magnetic response at high frequencies, as some noble metals (e.g. Au and Ag) have negative ϵ in optical region. In moving towards higher frequencies, downsizing the constituent elements of the magnetic resonators becomes inevitable. Because these nano-scale resonators generally require paired elements [183] [184] [200], the complexity involved in fabrication also rises during this process. Some authors have proposed that magnetic resonance could be achieved by coupling a patterned layer, such as nanorods [204] or staples [212], to a planar layer. In parallel to these works, we have investigated the role of SP resonances in the EOT through the hole-array/planar metallic multilayer structures [52] [52], as outlined in the previous chapters. With the aim of exploring simple alternatives for easy fabrication of LHMs at optical frequencies, here we extend our understanding of optical properties of such structures further into the design of magnetic metamaterials, and show that such structures can also exhibit a strong magnetic response and produce negative permeability in the optical region.

7.2.1 Structure Design and Analysis Methods

Figure 7.1 shows a schematic of the structure studied in this section. It consists of a glass substrate with a planar metal film and a metallic hole-array layer separated by a thin dielectric spacer; and is identical in many ways to the hole-arrays samples described in Chapter 5. However, here the design goal is a band of negative magnetism, and possibly even a full negative refractive index.

The physical principle of the hole-array/planar multilayer structures for generating optical magnetism is as follows. When light is incident on the subwavelength metallic hole arrays, LSPs can be generated at the edges of the holes in the direction perpendicular to the E-field of the incident light (y-direction in Fig.7.1). Under appropriate arrangement, the LSP resonance can induce an image charge distribution (with opposite sign to that on the patterned layer) on the planar metal film underneath. Therefore, the system functions in a similar fashion to a pair of patterned metallic layers [183] to provide resonant interactions: each individual unit cell can be considered as a nano-scale L-C oscillator where the top and bottom metallic elements along the direction of the H-field forms the inductor loop and the dielectric between them forms the capacitive element. When the incident field is coupled to the L-C resonance, the system can act as an effective medium with a strong magnetic response.

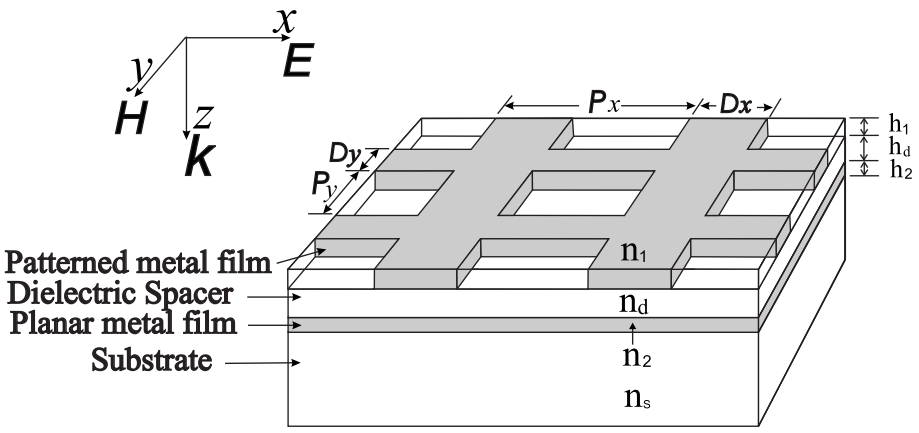

Figure 7.1: A schematic diagram of the structure studied in this chapter.

The complex transmission and reflection coefficients, t and r, of the structure are calculated using the RCWA based commercial grating analysis tool, G-Solver. For all the calculations, light is incident from air superstrate

($n = 1$) onto the hole-array layer at normal incidence. As indicated in Fig. 7.1, the system has following structural parameters. P_x and P_y are the lattice constants of the hole arrays along x- and y-direction, respectively; D_x is the metallic linewidth along the direction of the magnetic field (linewidth along y-direction) and D_y is that along the direction of the electric field (linewidth along x-direction); h_1, h_d and h_2 are the thickness of the hole-array layer, the dielectric spacer and the planar metal film, respectively; n_1, n_d, n_2 and n_s are the refractive indices of the materials used for metallic hole arrays, dielectric spacer, planar metal film and substrate, respectively. In the simulations, the complex dielectric constants of the metals (Ag and Au) were taken from Ref. [41].

Once t and r are found, the effective refractive index n and impedance Z of the multilayer system can be calculated by using Equations (6.4) and (6.5), and subsequently, the effective ε and μ can be retrieved using Equations (6.6) and (6.7).

To obtain an in depth understanding of the EM response of the structure, as well as to verify the nature of the resonances, we also investigated the E- and H-field distributions at resonance wavelengths using finite element method (FEM) based commercial software, FEMLAB (COMSOL).

7.2.2 RCWA Simulation Results

We applied RCWA technique to investigate the negative-magnetic response of hole-array/planar multilayer structures, and subsequently retrieve the effective parameters of the system. The emphasis is on analyzing the effects of varying metallic linewidth of the hole-array layer along the direction of incident H-field (D_x in Fig.7.1) on the EM properties of the structures, as these elements are the primary factor that determines the

magnetic response of LHMs [206].

7.2.2.1 Spectral Response and Retrieved Effective Parameters of the System

We performed series of simulation to investigate the magnetic properties of the structure, which include the resonance wavelength and its strength (evaluated by the difference between the maximum and the minimum value of μ'). Figure 7.2 shows the calculated (a) transmittance T and reflectance R, (b) impedance (c) permittivity and (d) permeability of a designed structure. The structure consists of a 30-nm-thick Ag hole-array layer, a 80-nm-thick dielectric spacer ($n = 1.5$) and a 30-nm-thick planar Ag film; the geometries of the hole arrays are: $P_x = P_y = 400$ nm, $D_x = 300$ nm and $D_y = 120$ nm. The rectangular holes are used here as such arrangement provides the better performance of the system, which coincides with that observed in the paired LHMs [206].

Similar to SPPs on the surfaces of a thin metal film bounded by same dielectric media, SPPs on two interfaces of a thin dielectric film sandwiched between two metallic films can also interact with each other, resulting in a splitting of SPPs into two modes [45]. We observe two sharp dips in the reflection spectrum (Fig. 7.2a) in between 500 nm and 700 nm; these are related to the SPP resonance at the dielectric spacer/Ag interfaces. One the other hand, the reflectance dip at around 880 nm is caused by the excitation of a LSP resonance in the patterned layer, resulting in magnetic activity within the structure. As shown in Fig. 7.2c, the real part of ε oscillates from negative values to positive values and the imaginary part of ε shows a peak around this wavelength, which indicates the existence of the plasmon resonance within the structure. On the other hand, the Z (Fig. 7.2b) and μ

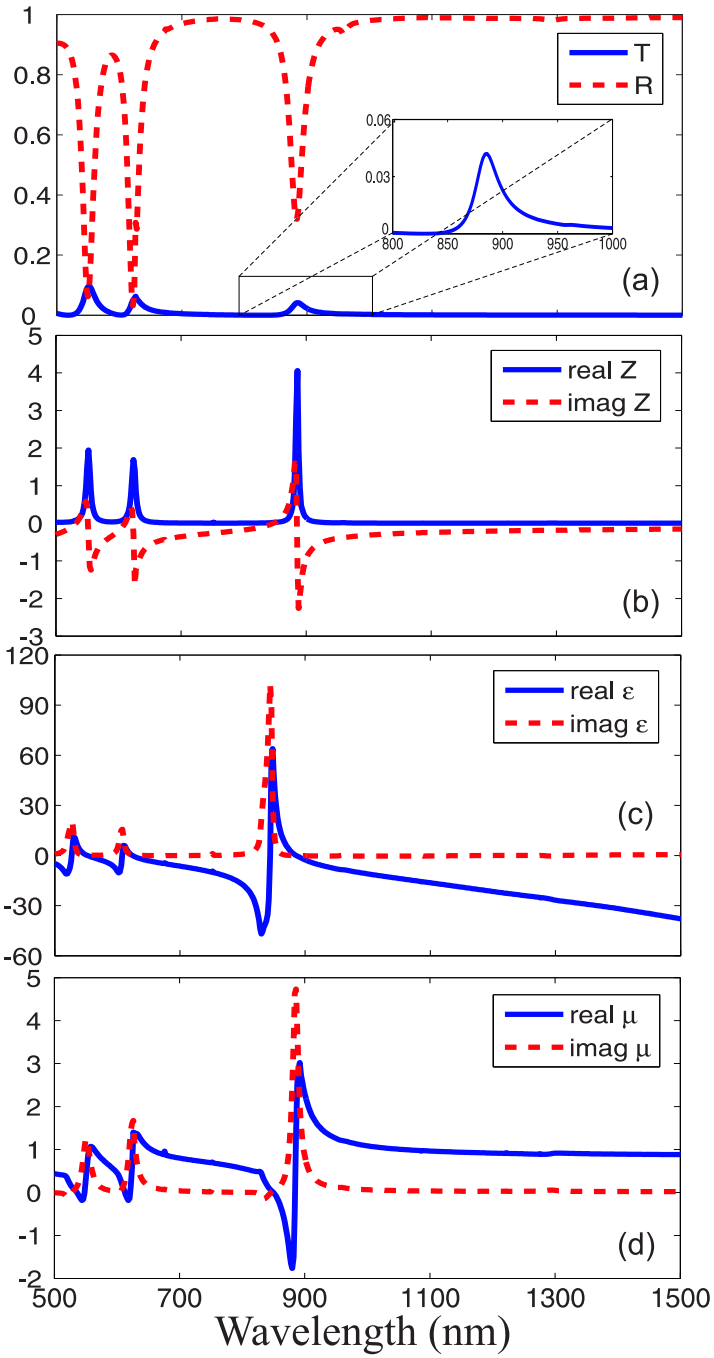

Figure 7.2: Simulation results of a structure consisting of a 30 nm Ag hole-array layer, a 80 nm dielectric spacer ($n = 1.5$) and a 30 nm planar Ag film, with $P_x = P_y = 400$ nm, $D_x = 300$ nm and $D_y = 120$ nm. (a) transmittance T and reflectance R, (b) impedance, (c) permittivity and (d) permeability.

(Fig. 7.2d) spectra show the characteristic of the L-C resonance at around 880 nm, that is, the imaginary part of Z and real part of μ exhibit strong modulations in this wavelength region. The real part of the effective μ retrieved from simulations ranges from -1.8 to 3.0 around this resonance.

The small transmission peak that appears around 880 nm (Fig. 7.2a, insert) is due to the fact that both effective ε and μ are complex. The dispersion relation $\omega^2 = k^2c^2/\varepsilon\mu$ indicates that, if both ε and μ are real and have opposite signs, k must be pure imaginary, i.e. no propagating modes exist at these frequencies [158] [22]. However, if ε and μ become complex then having pure imaginary k is no longer the only option, and waves can propagate through the medium. LHMs with only $\varepsilon < 0$ or $\mu < 0$ are called single-negative LHMs (SN-LHMs) and their existence has been experimentally verified from microwave to visible regions [183] [195] [196].

7.2.2.2 Effects of Varying Pattern Linewidth Along H-field of Incident Light

The magnetic response of LHMs formed by paired hole-array layers is dominated by the metal lines in the direction parallel to the magnetic component of the incident light; the inductance and capacitance of the equivalent L-C circuit in such structures are directly related to the metallic linewidth along this direction [183] [206]. Since the hole-array/planar system studied here is considered as a simplified approach for the paired structure to achieve negative μ at optical wavelengths, we are interested in the effects of varying D_x in Fig.7.1 on the magnetic response of the structure. Fig. 7.3 and Fig. 7.4 show the simulation results of reducing D_x used structure for Fig. 7.2 from 300 nm to 240 nm and 180 nm, respectively.

The transmission and reflection spectra in Fig. 7.2 – 7.4 reveal that

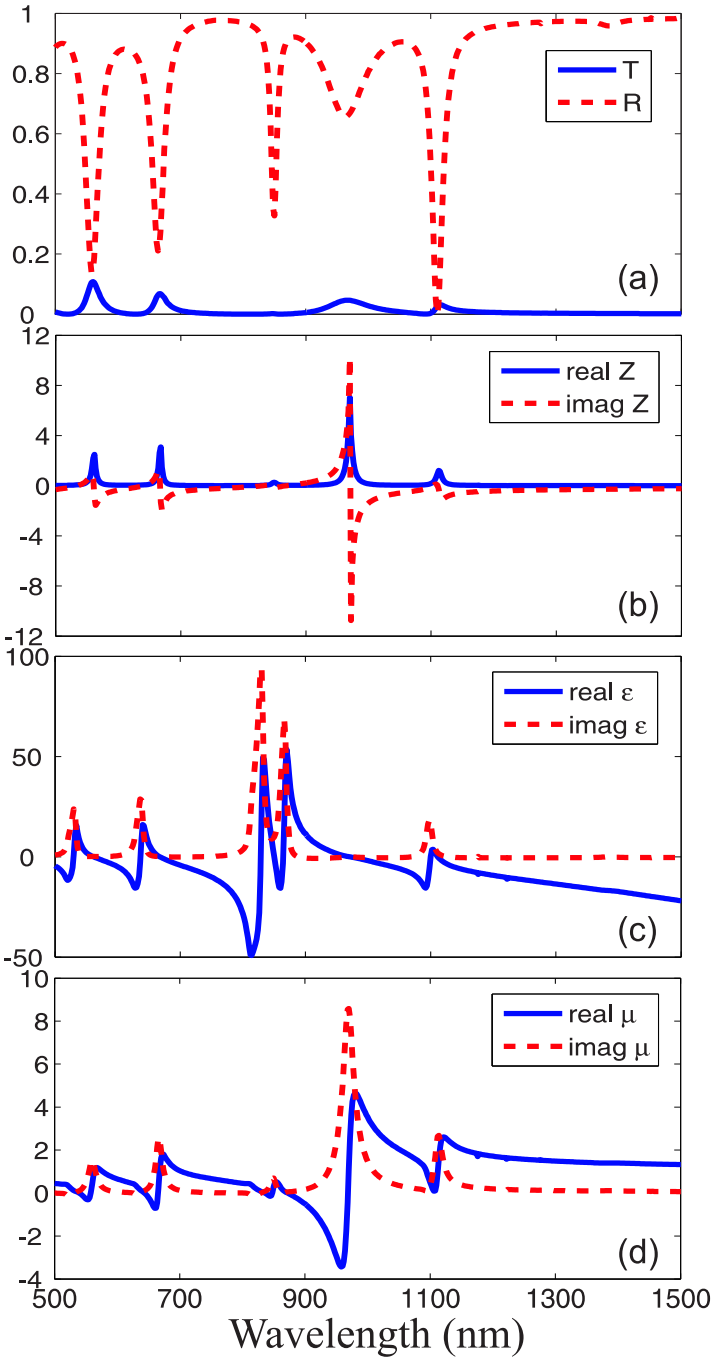

Figure 7.3: Simulation results for the structure with $D_x = 240$ nm. (a) transmittance T and reflectance R, (b) impedance, (c) permittivity and (d) permeability.

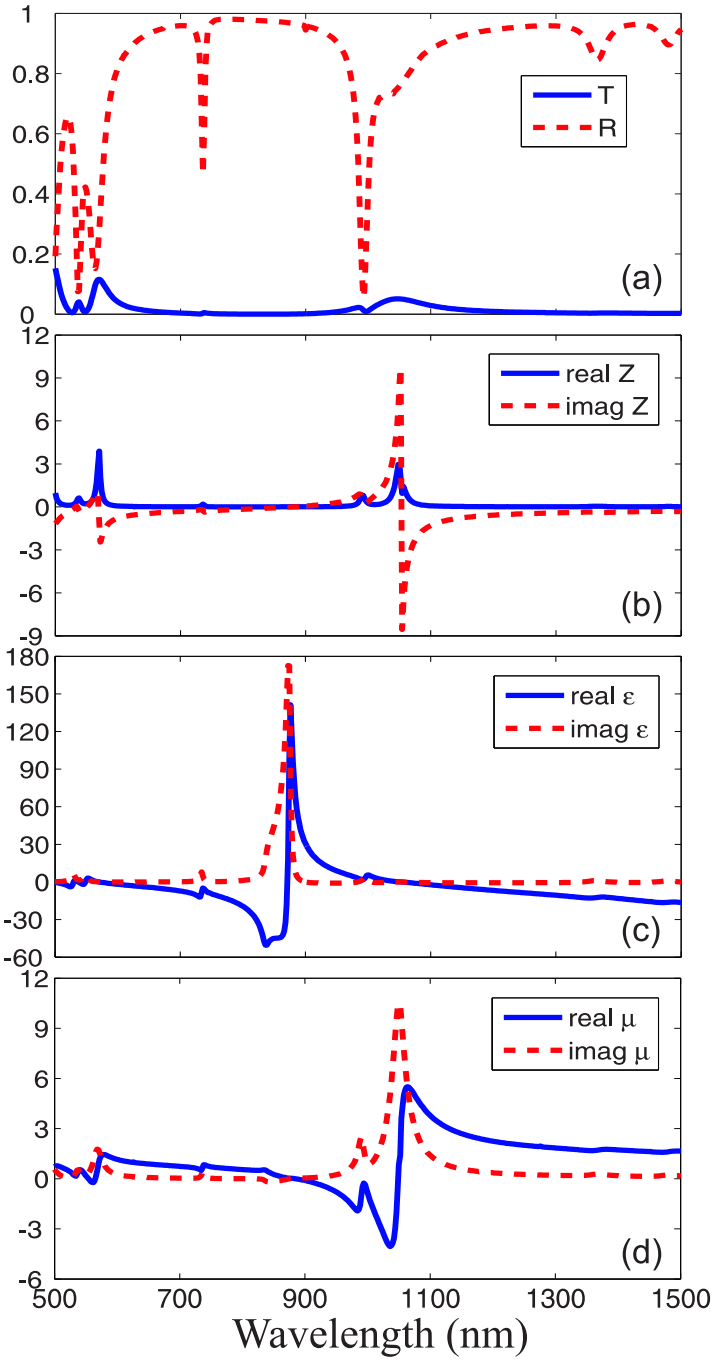

Figure 7.4: Simulation results for the structure with $D_x = 180$ nm. (a) transmittance T and reflectance R, (b) impedance, (c) permittivity and (d) permeability.

decreasing D_x results in the occurrence of additional resonances within the structure, owing to increases the opening area of the holes. On the other hand, the retrieved effective Z, ε and μ show that while the LSP resonance wavelength (indicated by the large oscillation in ε in between 700 nm to 950 nm) decreases with D_x, the magnetic resonance wavelength increases with D_x.

The values of the inductance and capacitance determine the resonant frequency of a L-C circuit. For the magnetic resonant structure consisting of arrays of paired finite-width metal stripes separated by a dielectric layer, narrowing the metallic linewidth along the direction of the magnetic field corresponds to reducing the inductance and capacitance of the L-C circuit, which in turn leads to a smaller resonance wavelength [206]. However, we observed an opposite trend in the hole-array/planar multilayer structures. This is due to the different EM responses in different regions of the 2D hole arrays, which will be discussed in detail in the following section through the investigation of near-field distribution within the structures.

It is worth noting that varying D_x indeed affects both the electric and magnetic resonances of the structure, as illustrated in Fig. 7.2 – 7.4, however, the influence on the former is less noticeable when compared to the latter. Similarly, varying D_y – the metallic linewidth along the direction of the electric field – also affects the characteristics of the magnetic resonance (results not shown here), but the major impact remains on the electric resonance of the structure.

7.2.3 Near-Field Distributions

To investigate the EM properties of the hole-array/planar multilayer system, and subsequently reveal the origin of magnetic activity within

it, we calculated the field distributions within the structures using finite element method (FEM) based commercial software, FEMLAB (COMSOL). We analyzed the amplitudes of E_x, E_z and H_y at the different resonance wavelengths for two structures used in the previous section (D_x = 300 nm and D_y = 180 nm). Fig. 7.5 illustrates the schematic of the top view of an unit cell, where the y = 200 nm and y = 400 nm lines correspond to the x-z planes that are at the centre of the unit cell and at the the centre of the neighboring unit cells, respectively.

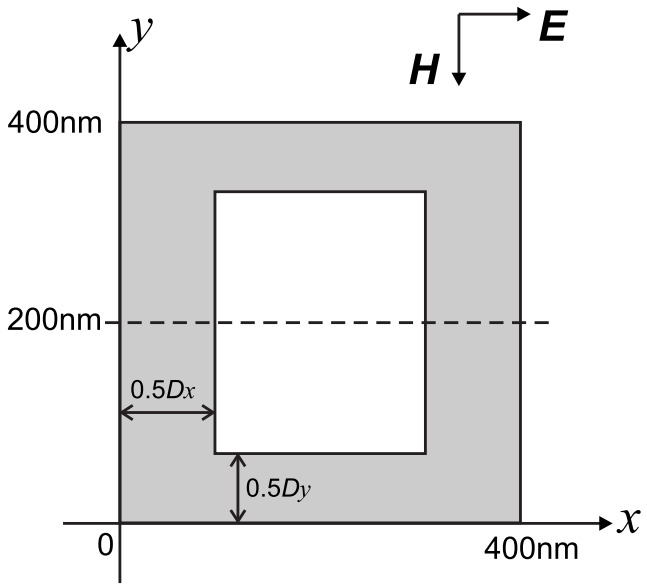

Figure 7.5: Top view of an unit cell.

We first simulated the field distributions within the structure having effective parameters shown in Fig. 7.2 (D_x = 300 nm). The calculated $|E_x|$, $|E_z|$ and $|H_y|$ at λ = 550 nm (the wavelength of the first reflection minimum) and λ = 880 nm (the wavelength of the effective μ minimum) are displayed in Fig. 7.6 and Fig.7.7, respectively. Here $|E_x|$ and H_y are the superposition of the incident field and the reflected field, whereas the $|E_z|$ is due to the reflected field only. The electric displacement vectors within the structure at

two resonances are also presented as arrows in the $|H_y|$ plots.

The $|E_x|$ and $|E_z|$ profiles shown in Fig. 7.6 indicate that the electric response of the structure at $\lambda = 550$ nm is mainly related to the excitation of a SPP resonance on the dielectric spacer/planar Ag interface; whereas $|E_x|$ and $|E_z|$ shown in Fig. 7.7 suggest that the electric response of the structure at $\lambda = 880$ nm is governed by the LSP modes on the edges of the metallic holes near the dielectric spacer/hole-array interface.

The nature of the different plasmon resonances at these two wavelengths can be clearly identified from the E_z profile, since it represents the field scattered by the subwavelength hole arrays. At $\lambda = 550$ nm, the $|E_z|$ maximum occurs on the dielectric spacer/planar Ag film interface near the centre of the unit cell and decays exponentially away from the interface, which is the character of the SPP resonance. Owing to the ohmic loss of the metal, the amplitude of this SPP field decreases rapidly along the y-direction and reaches its minimum near the centre of the neighboring unit cells. There also exists a LSP resonance at this wavelength, which is excited on the air superstrate/Ag interface at the edges of the subwavelength holes. However, the amplitudes of SPP and LSP fields reveal that the SPP resonance is the dominant mode at $\lambda = 500$ nm. The large E_z that is opposite to the SPP field on the other side of the dielectric spacer (dielectric spacer/Ag hole-array interface) is caused by the strong field enhancement from the SPP excitation on the planar Ag film, which induces a charge density redistribution on the patterned layer around that area. Owing to the interaction between the SPP and LSP resonances, the field pattern exhibits an irregular shape within the dielectric spacer.

On the other hand, the LSP resonance becomes the dominant mode at $\lambda = 880$ nm. As illustrated in Fig. 7.7, at this wavelength, the $|E_z|$

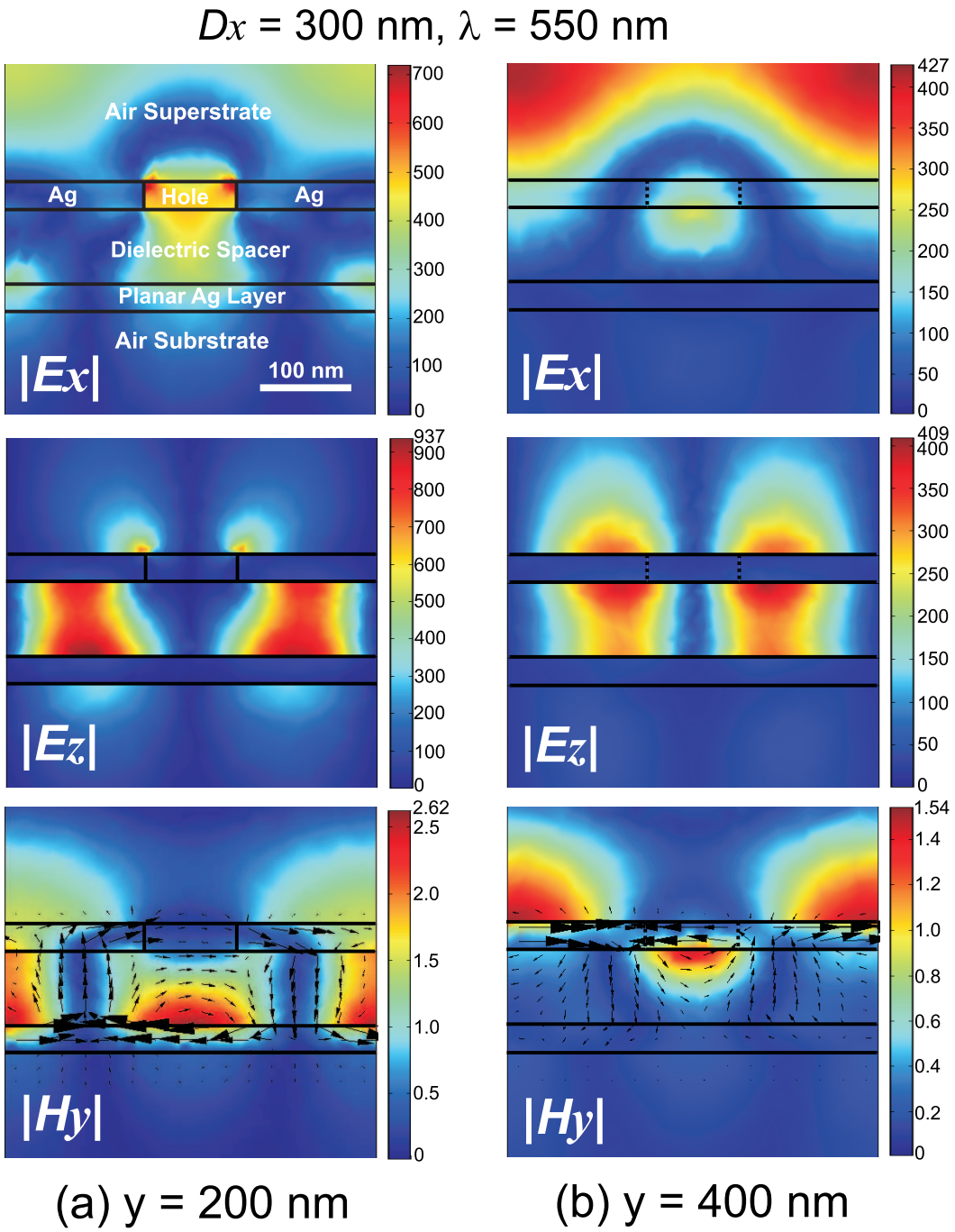

Figure 7.6: Field distributions in the structure of Fig. 7.2 at $\lambda = 550$ nm. The arrows in $|H_y|$ graphs represent the electric displacement.

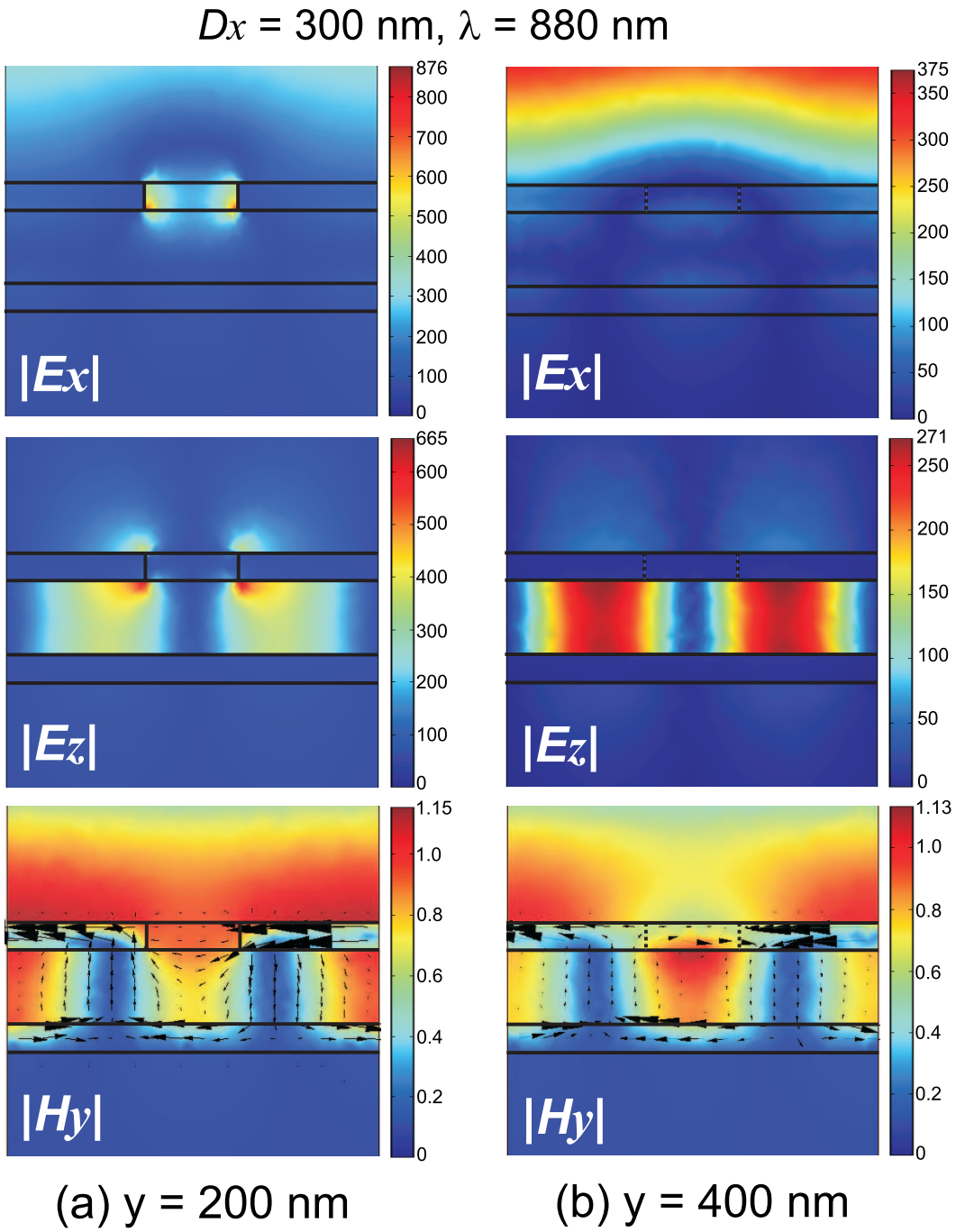

Figure 7.7: Field distributions in the structure of Fig. 7.2 at $\lambda = 880$ nm. The arrows in $|H_y|$ graphs represent the electric displacement.

maximum occurs on the dielectric spacer/Ag hole-array interface at the edges of the metallic hole; the enhanced near-field extends to the planar Ag film underneath, and induces a replica charge distribution with opposite sign near the surface of the Ag film. Therefore, the $|E_z|$ pattern shows a well defined rectangular shape within the spacer layer.

The large $|H_y|$ observed near the interfaces of the planar Ag film at 550 nm is just a subsidiary of the strong electric field enhancement from SP excitation (including both SPPs and LSPs) within the structure. The electric displacement vectors reveal that near the centre of the unit cell ($y = 200$ nm plane), the currents within the metallic components of the hole-array layer and the planar Ag film counterpart underneath are parallel (symmetric mode), whereas near the the centre of the neighboring unit cells ($y = 400$ nm plane), the magnitude of the current is negligible on the planar Ag film. The lack of effective circulating current loops at this wavelength implies that there is no magnetic resonance within the structure. In contrast, the electric displacement vectors shown in Fig. 7.7 clearly indicate the existence of the circular current loops within the structure at $\lambda = 880$ nm. Here the currents in the metallic components of the hole-array layer and their counterparts in the planar Ag film underneath are antiparallel (antisymmetric mode), which are closed through the displacement currents within the dielectric spacer near the edges of the hole. These circular currents generate the magnetic field to counteract the incident magnetic field and subsequently produce negative μ.

In the previous section, we studied the effects of varying pattern linewidth along the magnetic field of incident light (D_x in Fig.7.1) on the magnetic activity of the structure, and observed that magnetic resonance wavelength increases with the decreased linewidth. To understand this phenomenon, we calculated the field distributions within the structure having effective

parameters shown in Fig. 7.4 (D_x = 180 nm). The results of $|E_x|$, $|E_z|$ and $|H_y|$, as well as the electric displacement vectors, at λ = 1040 nm (the wavelength of the effective μ minimum) are displayed in Fig. 7.8.

Figure 7.8 shows that the E_x and E_z component within the structure follow the similar fashion as that in Fig. 7.7, however, the magnetic field distribution within the structure is somewhat different here, particularly near the centre of the neighboring unit cells. At the centre of the unit cell, the magnetic field highly concentrates in the space between the Ag lattice and the planar Ag film ($|H_y|$ in Fig. 7.8a). The electric displacement (arrows) clearly indicates the existence of circular current loops in this region, which leads to the magnetic activity, and subsequently, the negative μ. At the centre of the neighboring unit cells ($|H_y|$ in Fig. 7.8b), the strength of the H_y component is relatively weak within the structure.

The magnetic response of the hole-array/planar multilayer structure involves the contributions from two regions, as shown in Fig. 7.9: one is formed by the continuous metallic lines parallel to H-field and the planar film beneath them; the other is formed by the metallic components between these lines and the planar film beneath them, as labelled by region 1 and region 2 in Fig. 7.9, respectively.

In general the contribution from region 1 is the primary factor that determines the magnetic response of the structures; however, as the width of the region 1 increases (i.e., a large D_x), the role of region 2 also rises. The electric displacement (arrows) in Fig. 7.8b shows that only one current loop is excited for structure with small D_x (D_x = 180 nm here). In contrast, Fig. 7.7b reveals that the excitation of two anti-phase current loops in regions 1 and 2 when D_x of the structure is set to 300 nm. The existence of two inductively coupled circuits with anti-phase currents in such structure results

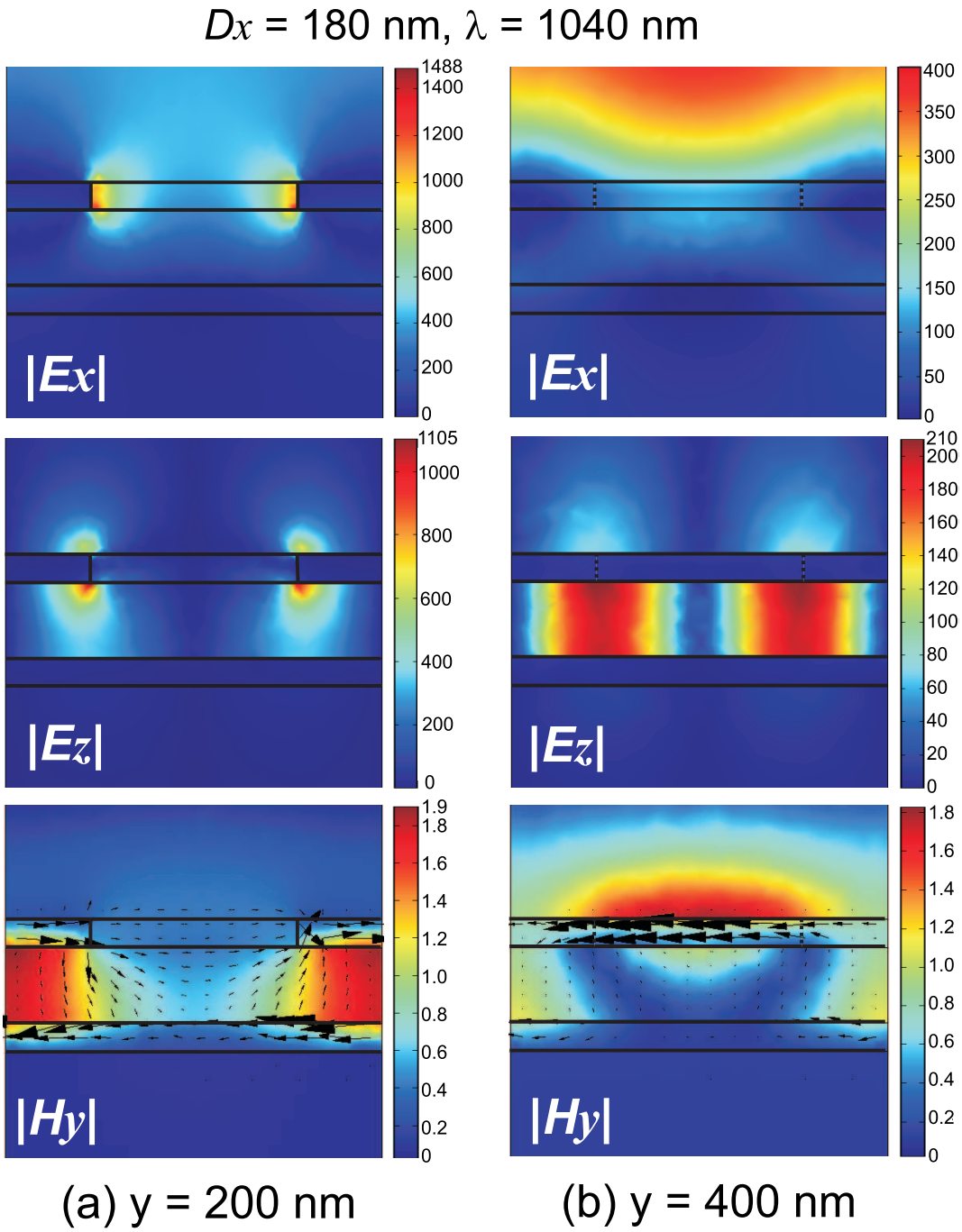

Figure 7.8: Field distributions in the structure for Fig. 7.4 at $\lambda = 1040$ nm. The arrows in $|H_y|$ graphs represent the electric displacement.

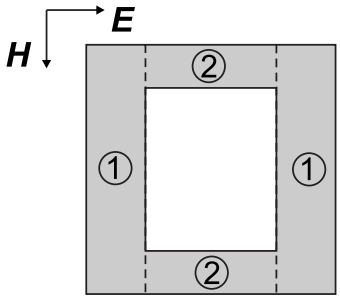

Figure 7.9: Two regions of an unit cell that have different magnetic responses (top view).

in a reduction in the total effective inductance, hence a higher L-C resonance frequency and a shorter resonance wavelength.

To sum up, the near-field distributions and the electric displacement vectors at different resonance wavelengths reveal the existence of SPP and LSP resonance within the the structure, and the latter gives rise to the magnetic resonance and the negative μ. Due to the 2D nature of the hole arrays, the overall magnetic response of the structure is a superposition of the effects from two functional parts of the unit cell, which leads to the unusual trend observed in Section 7.2.2.2, i.e., the magnetic resonance wavelength decreases as the pattern linewidth along incident H-field increases.

7.2.4 Tuning the Magnetic Resonance Wavelength of the Structure

We have studied the general EM properties of the hole-array/planar multilayer system and shown that such an arrangement could lead to a strong magnetic response in near infrared region. For practical implementations, it is necessary to obtain a controllable optical magnetism over the entire optical spectrum for various applications. For instance, extending the optical magnetism into the visible region could pave the way towards the most

prominent possible application of LHMs – perfect imaging. In this section, we investigate the possibility of tuning the magnetic resonance of the structure by studying the dependence of the magnetic resonance wavelength on the size of the unit cell and the material for dielectric spacer.

We firstly performed a series of simulations on varying the dimension of the unit cell in the x-y plane, in which the period of the hole arrays were set to $P_x = P_y = P$, and P increased from 150 nm to 600 nm with a step size of 50 nm; D_x and D_y were fixed to $0.75P$ and $0.3P$, respectively. The thicknesses of three individual layers (dimension of the unit cell in the z-direction were fixed to 30nm/80nm/30nm to keep the practical scaling of the unit cell for future experimental works, as well as to avert the complication introduced by the non-negligible skin effect of the metal, which results in the inhomogeneous distribution of the induced current inside the metal.

Figure 7.10 shows the dependencies of the real and imaginary parts of the effective μ on the unit cell dimensions. Clearly, as the dimension of the unit cell P decreases from 600 nm to 150 nm, the magnetic resonance shifts from $\sim$ 1300 nm to $\sim$ 500nm wavelength; the strength of the resonance, which is evaluated by the difference between the maximum and the minimum value of the real part of the effective μ, initially increases as P decreases and reaches its maximum at $P = 500$ nm, the value then decreases with P, indicating the weaker magnetic response of the structure.

Using the results shown in Fig. 7.10, we obtained the the magnetic resonance frequency of the structure as a function of the inverse of the unit cell size $(1/P)$, as well as the wavelength dependence of the minimum value of real μ, the results are displayed in Fig. 7.11a and Fig. 7.11b, respectively. Fig. 7.11a reveals that the magnetic resonance frequency of the structure closely follows the linear scaling law, i.e., $\omega = 1/\sqrt{LC} \propto 1/P$ when $P > 400$

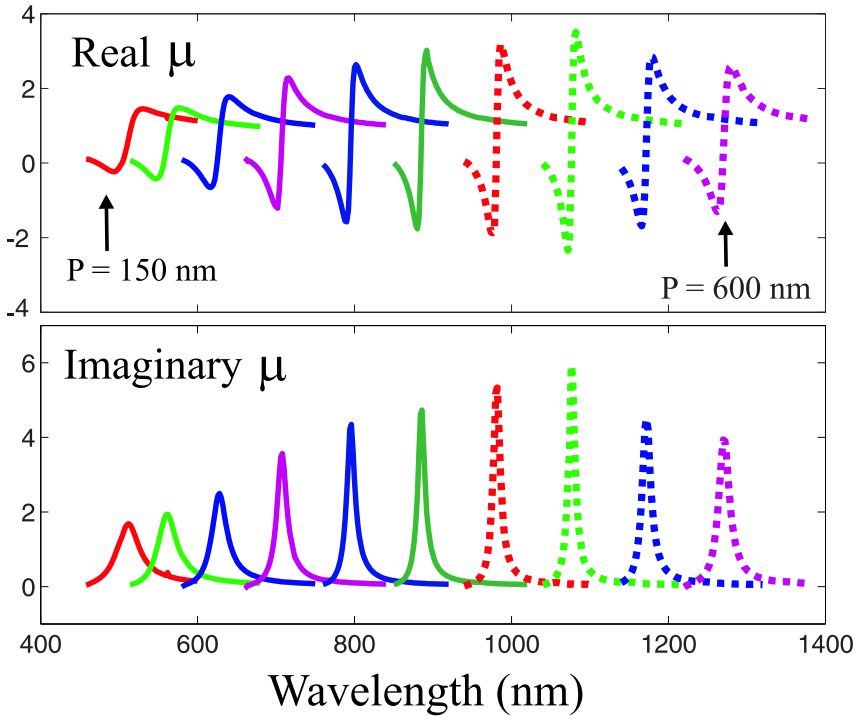

Figure 7.10: Retrieval effective μ for structures with P range from 150 nm to 600 nm.

nm (corresponds to 970 nm resonance wavelength). The linear relationship breaks down if one further decreases the size of the unit cell. On the other hand, Fig. 7.11b shows that the structure is able to produce a negative μ from near infrared (1300 nm) down to the blue light region (500 nm). However, the strength of the magnetic resonance decreases as the wavelength decreases, and real μ would cease to be negative at wavelengths below 420 nm.

As well as the size of the unit cell, the magnetic resonance of the structures can also be controlled by varying the arrangement of the cell, because each individual cell within the structure acts as a nano-scale L-C circuit whose inductance and capacitance are determined by the metallic components and the dielectric material between them. For example, in Section 7.2.2.1, we observed that adjusting the value of D_x (the metallic linewidth along

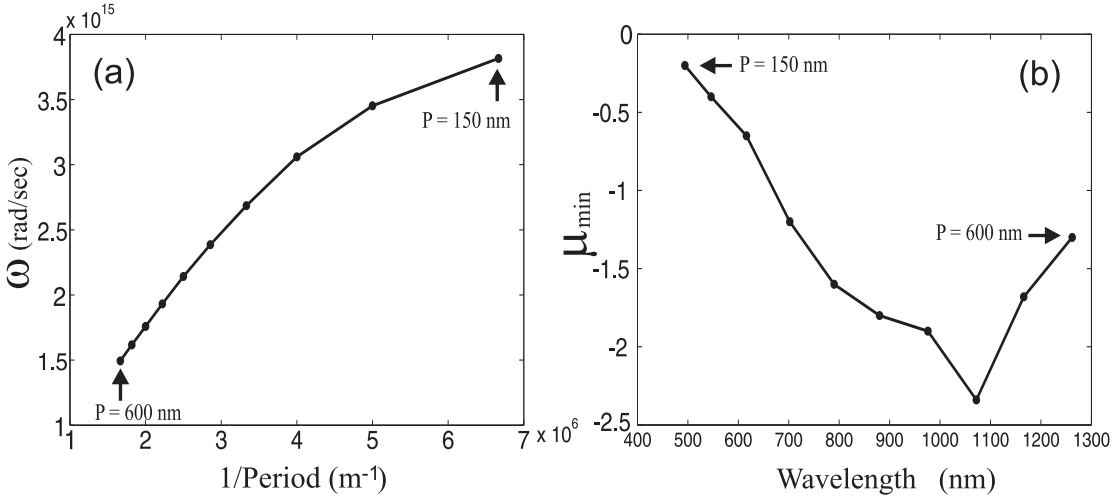

Figure 7.11: (a) The magnetic resonance frequency of the structure as a function of the inverse of the unit cell size, $1/P$; (b) the wavelength dependence of the minimum value of real part of the effective μ.

the direction of the magnetic field) altered both the wavelength and the strength of the magnetic resonance. Here we examine the potential of varying the optical properties of the dielectric spacer for controlling the magnetic resonance of the structures; the simulation results are shown in Fig. 7.12. All the structures consist of a 30-nm-thick Ag hole-array layer, a 80-nm-thick dielectric spacer and a 30-nm-thick planar Ag film; the geometric parameters of the hole arrays are: $P = 400$nm, $D_x = 300$ nm and $D_y = 120$ nm; three different materials were considered as dielectric spacer: MgF_2 ($n = 1.38$), glass ($n = 1.50$) and Al_2O_3 ($n = 1.65$).

Figure 7.12 reveals that reducing the dielectric constants of the spacer material moves both electric and magnetic resonance to the shorter wavelength side of the spectrum; and the amounts of shift are rather similar for the two different resonances. Nevertheless, its effects on the strength of these resonances are less significant when compared with its impacts on the resonance wavelengths. These can be understood by considering the

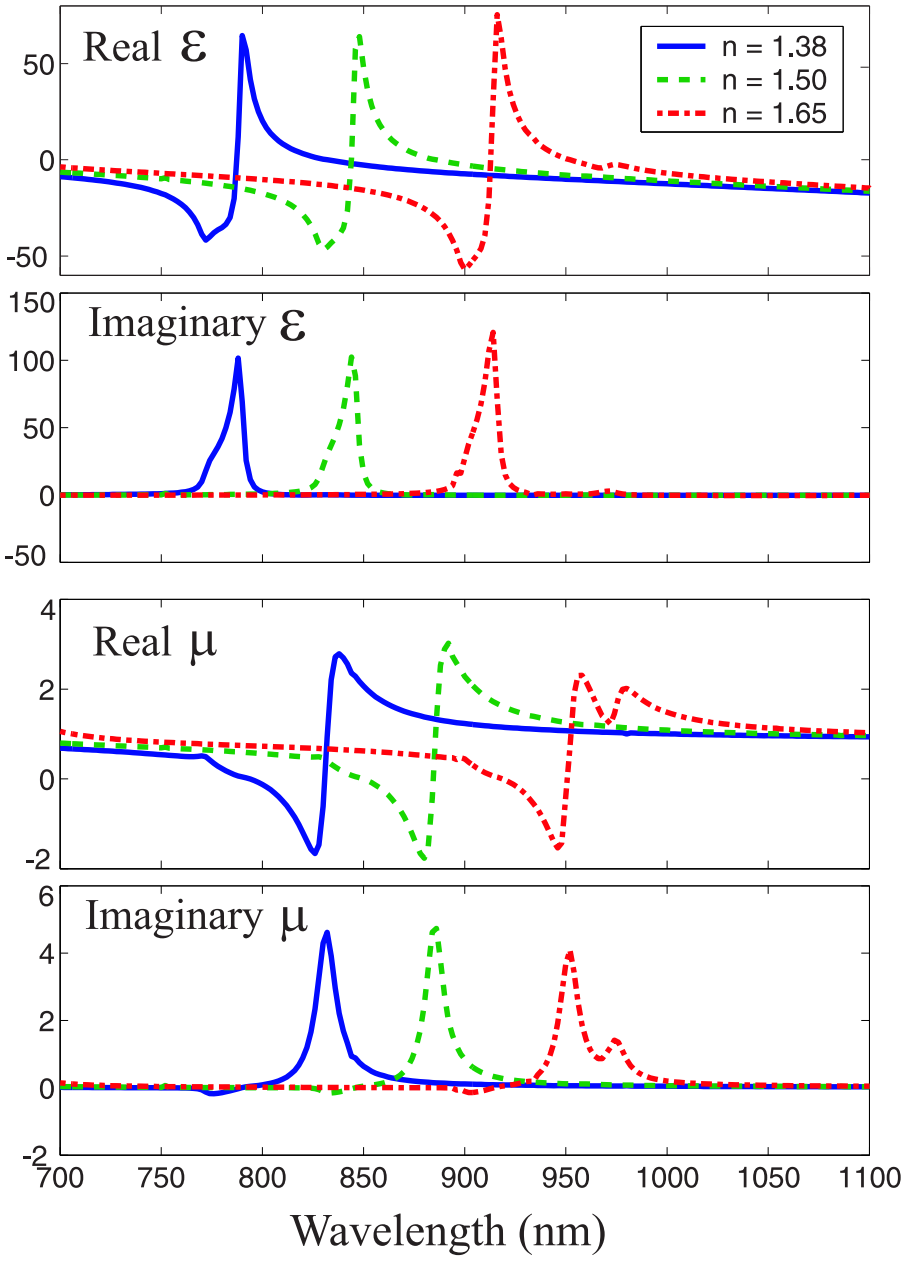

Figure 7.12: Effects of spacer material on the effective ε and μ.

origin of the magnetic resonance – the excitation of LSPs at the edges of the metallic holes on the hole-array/dielectric spacer interface. As discussed in Section 2.3.3, the characteristics of the LSP resonance, such as the spectral position, strength and linewidth, are directly related to the geometries of the metallic nanostructure, as well as the optical properties of the surrounding dielectric material. In the simulations, the geometries of the structures were fixed and the only variable was the optical constants of the surrounding dielectric material, the variation in the resonance wavelength therefore appeared to be more noticeable than that in the LSP (and magnetic) resonance strength(s). From L-C circuit point of view, decreasing the dielectric constants of the filling dielectric material reduces the capacitance of the structure, resulting in a higher resonance frequency (shorter resonance wavelength).

7.2.5 Summary

We have numerically demonstrated that planar/patterned multilayer structures have the potential to produce negative permeability from near infrared to visible wavelengths; the results are supported by two different simulation techniques. In such structures, the magnetic resonance wavelength can be controlled by simply scaling the dimensions of the unit cell; this can be further adjusted by modifying the geometric arrangements of the unit cell, as well as varying the optical properties of the dielectric spacer. This design could provide a simple alternatives for easy fabrication of LHMs at optical frequencies as it requires only a single patterned layer to achieve optical magnetism. Aside from its magnetic response, the structure exhibits negative ε behaviour at different wavelengths, and the challenge is now to find design parameters that will give double-negative behaviour.

7.3 LHMs Using Single Layer Plasmonic Structure

As discussed in Chapter 6, in addition to utilizing optical L-C resonance to achieve the desired EM response, it has been suggested that the excitation of electrostatic resonances within the structure consisting of subwavelength metallic inclusions can also produce strong magnetic activity when its operating frequency approaches the plasma frequency of the particles [213] [215] [217]. In this section, we propose a new design of a single-layer LHM based on this approach.

7.3.1 Structure Design

The designed structure consists of a single layer of 2D periodic metallic inclusions in the x-y plane; its thickness in the z-direction, h, is assumed to be the same as the height of the inclusion and is much smaller ($h < 100$ nm) than the wavelength of the incident light, λ. Fig. 7.13 illustrates the schematic of its unit cell configuration (top view). The basic element of the unit cell is a rectangular prism whose dimensions in the x-y plane are labelled as w_o and l_o; some stepwise modulations, whose dimensions are indicated as w_1, w_2 and w_3 along x-direction and l_1, l_2 and l_3 along y-direction, are then introduced on both sides of this elementary rectangular to function as strong scatters to produce higher-multipole plasmonic resonances for achieving a magnetic response. As these resonances are electrostatic in nature, their characteristics (spectral position and strength) are mainly governed by the shape of the inclusions. It is worth noting that the number of modulation steps can be introduced to the system are not restricted to the three steps shown in Fig. 7.13.

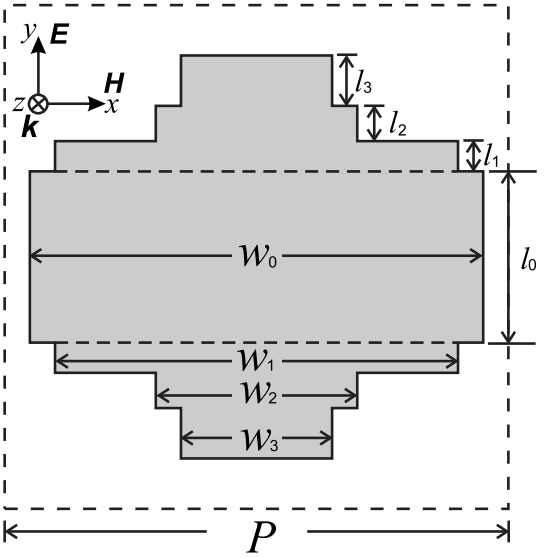

Figure 7.13: A schematic diagram of a single layer LHM unit cell configuration (top view). The unit cell has a finite thickness h in the z-direction.

The effective parameters of the structure were obtained by using the same technique as described in the previous section, i.e., the complex transmission and reflection coefficients were firstly calculated using RCWA technique; the effective parameters were then retrieved from these results by applying Equations (6.4) – (6.7). In the simulations, the incident light has H_x and E_y components and propagates in the z-direction; both the incident and outgoing media are air ($n = 1$) and the complex dielectric constants of the Ag inclusions were taken from Ref. [41].

7.3.2 Simulation Results

The EM properties of the structures were first analyzed by examining the effects of each individual geometric parameter indicated in Fig. 7.13 on the effective n, ε and μ of the system; the results were then used to optimize

the arrangement of the system to obtain a double-negative feature and the highest possible FOM. Fig. 7.14 show the simulation results for one of the optimized designs whose geometric parameters are listed in Table 7.1. The results reveal two key characteristics of the structure: the lowered electron plasma frequency ω_p ($\varepsilon = 0$ at $\sim$ 820 nm wavelength); and simultaneously negative ε and μ at the wavelengths around 1100 nm to 1130 nm.

Table 7.1: Configurations of the structure whose EM properties are shown in Fig.7.14.

P (nm)	h (nm)	w_o	l_o	w_1	l_1	w_2	l_2	w_3	l_3
340	80	0.9P	0.34P	0.8P	0.46P	0.4P	0.6P	0.3P	0.8P

The transmission spectrum of the structure (Fig. 7.14a) shows that the transmission efficiency peaks around the wavelength corresponding to ω_p ($\sim$ 820 nm) and the structure shows the metal-like behaviour (highly reflective) when moving towards the longer wavelength side of the spectrum. On the other hand, there is a shoulder in the transmission curve at the wavelengths between 1100 nm to 1150 nm and the transmission falls rapidly beyond this region. This feature coincides with the double-negative behaviour (hence the negative refractive index) of the structure, as in the spectral region where a medium having negative refractive index, the transmitted light exhibits a negative phase velocity and the destructive interference between the incident and the transmitted light results in a sharp decrease in the transmission around the negative index region. In fact, this phenomenon has been observed experimentally by different groups [183] [208]. We also observe that in between 1100 nm and 1150 nm, the real part of the impedance has a peak whereas the imaginary part shows a modulation (Fig. 7.14b). As a result

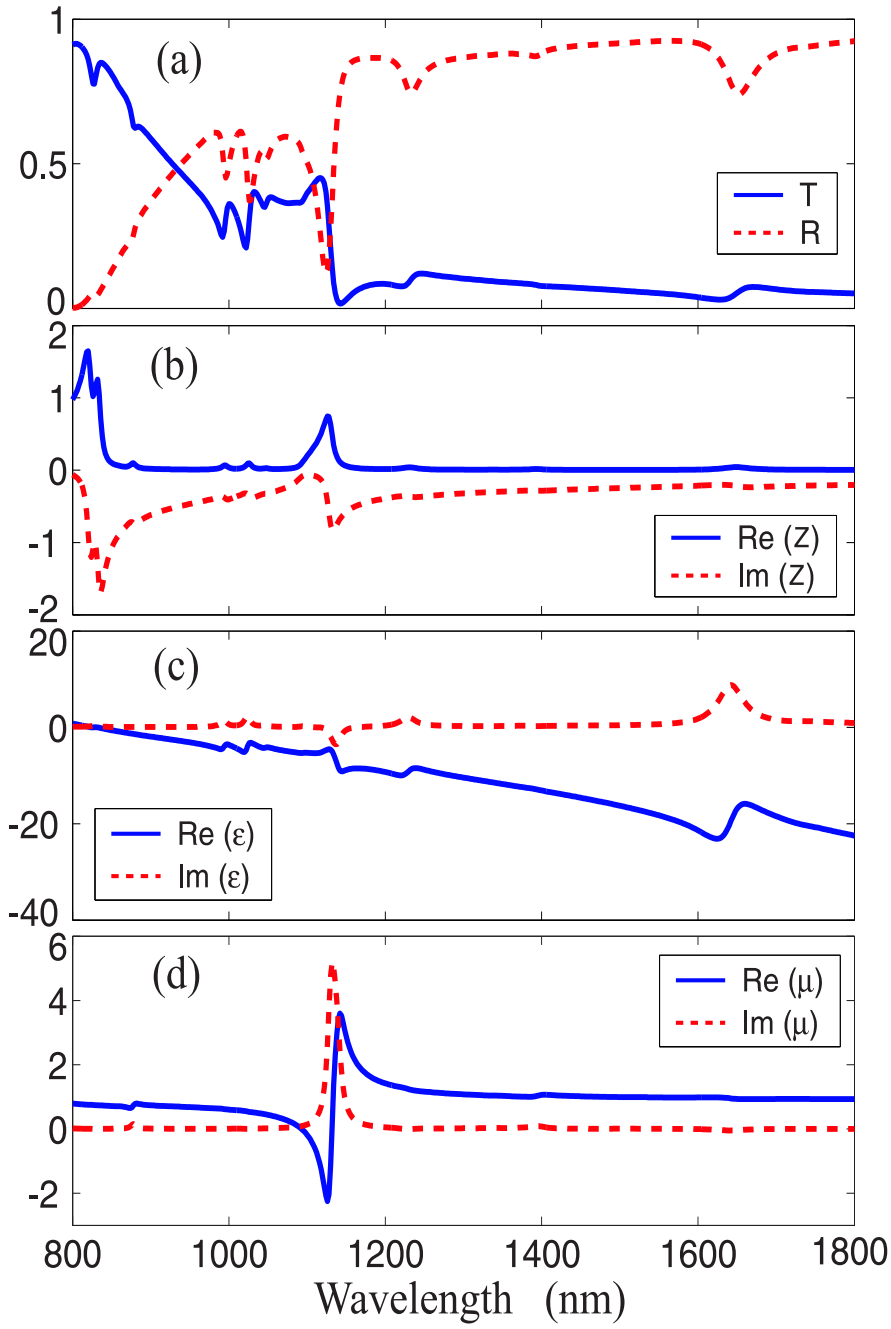

Figure 7.14: Simulation results of a single layer LHMs (a) transmittance T and reflectance R, (b) impedance, (c) permittivity and (d) permeability.

of better impedance matching between the structure and the surrounding medium (air), a sharp dip in the reflection appears.

Figure 7.14c shows that the real part of ε exhibits some oscillations at 1000 nm to 1300 nm, due to the excitation of higher multipole plasmon resonances within the structure, and these resonances are accountable for the magnetic resonance and the negative μ observed in Fig. 7.14d. This was studied further using FEM technique at the resonance wavelengths. As illustrated in Fig. 7.15, at the magnetic resonance, both the electric and magnetic field distributions show quadrupole resonance profile. Furthermore, as reported in other designs of LHMs [188], [189] and [190], in the spectral range where the magnetic resonance occurs, the imaginary part of ε also becomes negative over a narrow spectral region.

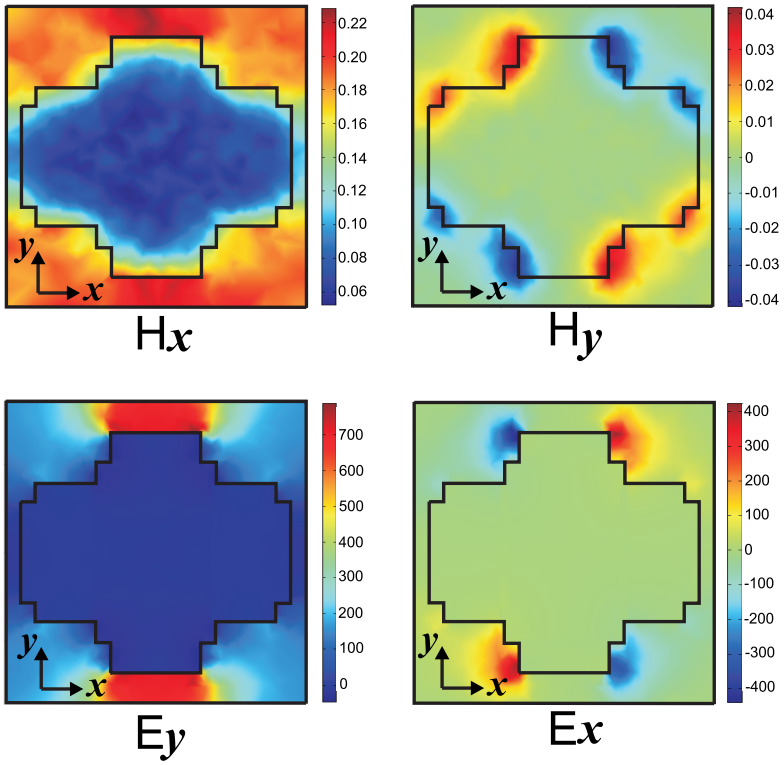

Figure 7.15: Field distributions across $z = \frac{1}{2}h$ plane at $\lambda = 1126$ nm.

The performance of a LHM is characterized by its figure of merit (FOM), which is defined as -Re(n)/Im (n). As displayed in Fig.7.16, owing to the existence of double-negative behaviour, the designed structure has an impressive FOM reaching 4.2 at $\lambda = 1115$ nm, which is rather attractive for future physics experiments and application development.

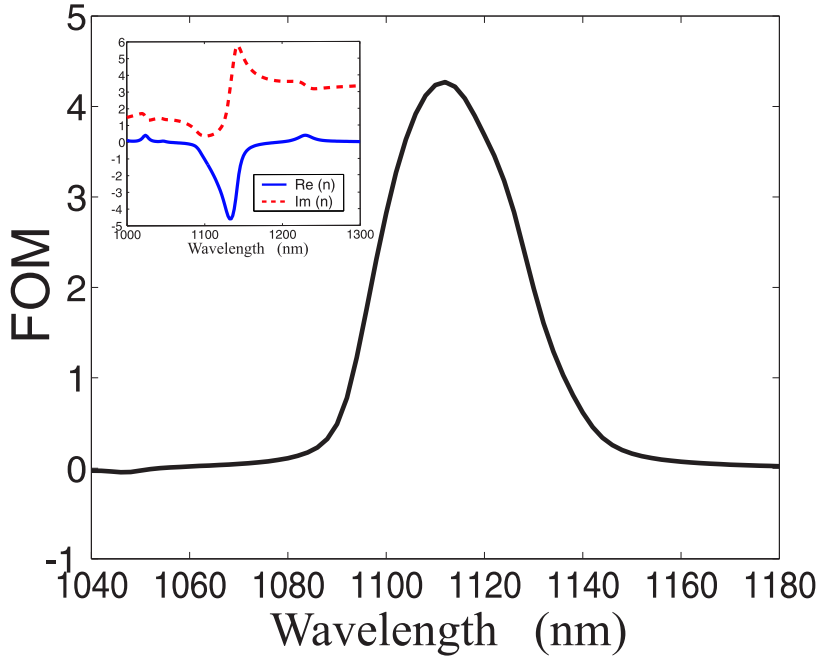

Figure 7.16: The figure of merit (FOM) of the single layer LHMs. The insert shows the effective refractive index of the structure.

7.3.3 Discussion and Conclusion

There are some issues also need to be addressed here. The first one is related to the RCWA based commercial software package (G-Solver) that was used to determine the complex transmission and reflection coefficients of the structure. In RCWA, the EM fields and material permittivities inside the corrugated region are expanded in terms of (finite) Fourier series, which are solutions to Maxwells equations. For highly conducting grating

materials it generally requires a high number of Fourier components to obtain convergence in the calculation [150]. However, for calculations of 2D metallic gratings, G-Solver appears to be highly unstable as the number of orders increases. Therefore, the number of orders retained in the calculation here were restricted to 2 in order to obtain meaningful results. Consequently, the amount of uncertainty existing in these results remain unclear at this stage and more reliable simulation codes need be developed in the near future. However, we note that the physical effects predicted from RCWA simulations have been confirmed independently using FEM techniques, so we have some confidence that the behaviour of these new structures is at least qualitatively correct.

The second issue is connected with the homogenization of the LHMs. Currently it is customary to assume the physical thickness of the structure to be the effective thickness of the metamaterial. However, optical LHMs generally involves large evanescent field component at the spectral region of operation. Therefore, the questions arise in the validity of the complex transmission and reflection coefficients based approach [185]. Furthermore, the practical applications of LHMs usually require left-handed media with thickness in the order of the operating wavelength. The single layer structure can serve as a basic building block to construct a multilayer stack and a detailed investigation on the effects of the subsequential coupling process between layers on the effective parameters of the system is required.

In conclusion, while currently there are certain issues unsolved, the designed structure opens up new possibility to construct optical LHMs with great engineering simplicity. The structure is based on the excitation of higher-multipole electrostatic resonance by the strong scatters presented in the stepped subwavelength metallic inclusions and the double-negative

behaviour occurs in the spectral range where these higher-order modes dominate over the dipole mode. The approach offers great degrees of freedom in controlling of the EM properties of the structure, as the resonances are electrostatic in nature whose properties are dominated by the shape of the inclusions. More important, the structure exhibits very low loss, which is essential for future physics experiments and application development.

§ 8. Conclusions and Future Work

The work of this thesis investigated the interaction of light with materials in/through surface-plasmon-supporting planar/patterned metallo-dielectric multilayer structures in two different aspects: the physical origin of the extraordinary optical transmission through plasmonic structures and the designs of optical magnetic metamaterials.

In the study of the EOT phenomenon, SP-assisted transmission was demonstrated experimentally through two types of multilayer structures, namely planar/grating and planar/hole-array systems. The existence of surface plasmon polariton (SPPs) and localized surface plasmons (LSPs), and their roles in the EOT phenomenon, were revealed from both experiments and simulations.

Based on the findings from the EOT study, the planar/hole-array structure was explored as a simpler approach to obtain artificial magnetic response at optical wavelengths. Simulations suggested that a controllable optical magnetism could be achieved in such structures.

Although this thesis focused on the planar/patterned multilayer structures, a single-layer plasmonic structure as an optical left-handed metamaterial (LHM) was discussed in the final part of the work.

In this chapter, the results presented in this thesis were summarized and the future work and applications that can follow from the work of this thesis are highlighted.

8.1 EOT Through Planar Metal Films

The aim of this research is to obtain an in-depth understanding of the extraordinary light transmission through plasmonic structures; and the multilayer system allows a direct control of the excitation/coupling of different resonances in order to identify the physical origin of EOT phenomenon.

EOT through planar metal films have been observed experimentally in the structures consisting of two different SP-excitation mechanisms, namely subwavelength metallic gratings and hole arrays. The measured transmission maxima through these two arrangements reach 20% and 39%, respectively; whereas the simulations suggest that the potential transmission of the former could be greater than 65% and that of the latter could exceed 70%, with FWHMs being less than 10 nm for both cases. Both the experiments and the rigorous coupled-wave analysis (RCWA) simulations revealed that the unusual transmission peaks observed through planar/patterned multilayer structures were related the excitations of SPPs on the planar metal films as their spectral positions closely follow the dispersion relations SPPs; and the splitting of SPP modes on thin metals were also observed in the transmission spectra of the structures.

The near-field distributions at resonance wavelengths were calculated using finite element method (FEM), and the dispersion relations of the structures were simulated using RCWA. Both results revealed the co-

existence of SPP, LSP and waveguide-cavity resonances within the structures; the coupling between these resonances gave rise to the EOT through the plasmonic structures.

A number of projects could be taken up to explore the findings from the planar/patterned metallo-dielectric multilayer structures for application developments, which include: constructing narrow-band optical filters, improving the performance of the light emitting devices (LEDs), and developing sensitivity of SP-based bio-sensors. Development of immunobiosensor based on the understanding of SP resonances obtained from planar/patterned multilayer structure is currently underway, and the prototype devices have been tested. Fig. 8.1 illustrates the sensing scheme that utilizes the interaction of LSPs and SPPs to enhance the signal level. The device show a noticeable improvement on the detection sensitivity in a proof-of-concept project [218], which opens up the possibility of producing low-cost, portable and robust biosensors.

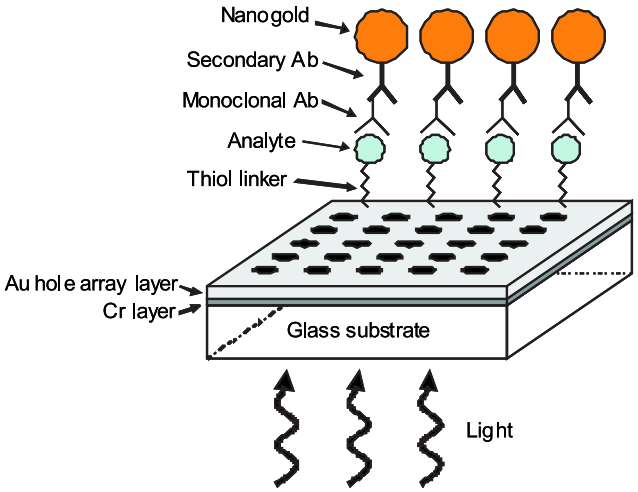

Figure 8.1: An immunobiosensing scheme that utilizes the interaction of the SPPs on the hole-array layer and the LSPs on the gold nanoparticle to enhance the signal level [218].

8.2 Optical Metamaterials

The purpose of this aspect of the work was to investigate simple alternatives for constructing LHMs at optical frequencies. Two new designs of optical metamaterials, both with only a single patterned layer, were proposed and their electromagnetic properties were analyzed numerically using two independent simulation techniques (RCWA and FEM).

The first design was an optical magnetic material formed from a planar/patterned multilayer structure. The LSP resonances existing in such a structure were utilized to produce L-C resonances, and subsequently, to obtain optical magnetism. Simulation results show that with appropriate arrangement a controllable band of negative permeability could be accessed in the spectral range from near infrared (1300 nm) down to blue light (500 nm); and the tuning of the magnetic resonance could be achieved by altering the geometries of the structure. As the structure exhibits negative ε behaviour at different wavelengths, further investigations in design parameters are required in order to achieve a double-negative behaviour (simultaneously $\varepsilon < 0$ and $\mu < 0$) in such structure.

The second design was a optical LHMs consisting of a single-layer of periodic plasmonic inclusions, which was based on the excitation of the high-order multipole electrostatic resonances in the inclusions to achieve simultaneously $\varepsilon < 0$ and $\mu < 0$. As a result of the double-negative behaviour, the structure exhibits very low loss. The simulation results show that the FOM of an optimized structure reached 4.2 at 1115 nm wavelength.

Much about the optical metamaterials is yet to be discovered. The next rational step in the study of this topic is to verify the simulation results experimentally, as there are some concerns over the reliability of commercial simulation tool used to calculate the spectral response of the designed

structures. Meanwhile, it would be worth investigating the possibility of using field-averaging method discussed in Section 6.2.2 to extract the effective parameters of the designed structures. For future practical applications of LHMs, the electromagnetic properties of the bulk metamaterials consisting of stacks of designed metamaterial of small thickness need to be investigated.

Bibliography

[1] R. R. Schaller. Moore's law: past, present and future. *IEEE Spectrum*, 34(6):52–59, 1997.

[2] P. Kapur, J. P. McVittie, and K. C. Saraswat. Technology and reliability constrained future copper interconnects - part i: Resistance modeling. *IEEE Transactions on Electron Devices*, 49(4):590–597, 2002.

[3] P. Kapur, G. Chandra, J. P. McVittie, and K. C. Saraswat. Technology and reliability constrained future copper interconnects - part ii: Performance implications. *IEEE Transactions on Electron Devices*, 49(4):598–604, 2002.

[4] A. V. Krishnamoorthy and D. A. B. Miller. Scaling optoelectronic-vlsi circuits into the 21st century: A technology roadmap. *IEEE Journal of Selected Topics in Quantum Electronics*, 2(1):55–76, 1996.

[5] M. J. Kobrinsky, B. A. Block, J. F. Zheng, B. C. Barnett, E. Mohammed, M. Reshotko, F. Robertson, S. List, I. Yang, and K. Cadien. On-chip optical interconnects. *Intel Technology Journal*, 8(2):129–141, 2004.

[6] E. Cassan, D. Marris, Rouviere, L. M., Vivien, and S. Laval. Comparison between electrical and optical global clock distributions for cmos integrated circuits. *Optical Engineering*, 44(10):Art.No.105402, 2005.

[7] E. Hecht. *Optics*. Addison-Wesley, third edition, 1998.

[8] P. J. Silverman. The intel lithography roadmap. *Intel Technology Journal*, 6(2):55–61, 2002.

[9] T. W. Ebbesen, H. J. Lezec, H. F. Ghaemi, T. Thio, and P. A. Wolff. Extraordinary optical transmission through sub-wavelength hole arrays. *Nature*, 391(6668):667–669, 1998.

[10] H. Raether. *Surface Plasmons on Smoother and Rough Surfaces and on Gratings*. Springer-Verlag, 1988.

[11] J. Homola, S. S. Yee, and G. Gauglitz. Surface plasmon resonance sensors: review. *Sensors and Actuators B*, 54:3–15, 1999.

[12] H. Ditlbacher, J. R. Krenn, G. Schider, A. Leitner, and F. R. Aussenegg. Two-dimensional optics with surface plasmon polaritons. *Applied Physics Letters*, 81(10):1762–1764, 2002.

[13] Z. J. Sun and Kim H. K. Refractive transmission of light and beam shaping with metallic nano-optic lenses. *Applied Physics Letters*, 85(4):642–644, 2004.

[14] S. A. Maier, M. D. Friedman, P. E. Barclay, and O. Painter. Experimental demonstration of fiber-accessible metal nanoparticle plasmon waveguides for planar energy guiding and sensing. *Applied Physics Letters*, 86(7):Art. No. 071103, 2005.

[15] E. Ozbay. Plasmonics: Merging photonics and electronics at nanoscale dimensions. *Science*, 311(5758):189–193, 2006.

[16] R. Zia, J. A. Schuller, A. Chandran, and M. L. Brongersma. Plasmonics: the next chip-scale technology. *Materials Today*, 9(7-8):20–27, 2006.

[17] S. A. Maier. Plasmonics: The promise of highly integrated optical devices. *IEEE Journal of Selected Topics in Quantum Electronics*, 12(6):1671–1677, 2006.

[18] W. L. Barnes, A. Dereux, and T. W. Ebbesen. Surface plasmon subwavelength optics. *Nature*, 424(6950):824–830, 2003.

[19] A. V. Zayats and I. I. Smolyaninov. Near-filed photonics: surface plasmon polaritons and localized surface plasmons. *Journal of Optics A: Pure and Applied Optics*, 5:16–50, 2003.

[20] C. Genet and T. W. Ebbesen. Light in tiny holes. *Nature*, 445(7123):39–46, 2007.

[21] J. B. Pendry. Negative refraction makes a perfect lens. *Physical Review Letters*, 85(18):3966–3969, 2000.

[22] D. R. Smith, W. J. Padilla, D. C. Vier, S. C. Nemat-Nasser, and S. Schultz. Composite medium with simultaneously negative permeability and permittivity. *Physical Review Letters*, 84(18):4184–4187, 2000.

[23] G. V. Eleftheriades and K. G. Balmain, editors. *Negative-Refraction Metamaterials: Fundamental Principles and Applications*. John Wiley & Sons, Inc., Hoboken, New Jersey, 2005.

[24] V. M. Shalaev. Optical negative-index metamaterials. *Nature photonics*, 1:41–48, 2007.

[25] A. V. Zayats, I. I. Smolyaninov, and A. A. Maradudin. Nano-optics of surface plasmon polaritons. *Physics Reports*, 408:131–314, 2005.

[26] G. Mie. Articles on the optical characteristics of turbid tubes, especially colloidal metal solutions. *Annalen der Physik*, 25(3):377–445, 1908.

[27] J. Zenneck. Breeding of even electromagnetic waves along an even conducting surface and its relation to radiotelegraphy. *Annalen der Physik*, 23(10):846–866, 1907.

[28] A. Sommerfeld. The broadening of the waves and the wireless telegraph. *Annalen der Physik*, 28(4):665–736, 1909.

[29] U. Fano. The theory of anomalous diffraction gratings and of quasi-stationary waves on metallic surfaces (Sommerfeld's waves). *Journal of the Optical Society of America*, 31:213–222, 1941.

[30] R. W. Wood. On a remarkable case of uneven distribution of light in a diffraction grating spectrum. *Proceedings of the Physical Society of Lodon*, 18(1):269–275, 1902.

[31] D. Pines and D. Bohm. A collective description of electron interactions:ii. collective vs individual particle aspects of the interactions. *Physical Review*, 85(2):338–353, 1952.

[32] D. Pines. Collective energy losses in solids. *Reviews of Modern Physics*, 28(3):184–198, 1956.

[33] R. H. Ritchie. Plasma losses by fast electrons in thin films. *Physical Review*, 106(5):874–881, 1957.

[34] C. J. Powell and J. B. Swan. Effect of oxidation on the characteristic loss spectra of aluminum and magnesium. *Physical Review*, 118(3):640–643, 1960.

[35] Y. Y. Teng and E. A. Stern. Plasma radiation from metal grating surfaces. *Physical Review Letters*, 19(9):511–514, 1967.

[36] A. Otto. Excitation of nonradiative surface plasma waves in silver by method of frustrated total reflection. *Zeitschrift fur Physik*, 216:398–410, 1968.

[37] E. Kretschmann and H. Raether. Radiative decay of non-radiative surface plasmons excited by light. *Z. Naturforsch*, 23A:2135–2136, 1968.

[38] U. Kreibig and P. Zacharia. Surface plasma resonances in small spherical silver and gold particles. *Zeitschrift fur Physik A Hadrons and Nuclei*, 231(2):128–143, 1970.

[39] A. Otto. Surface enhanced raman-scattering (sers), what do we know. *Applied Surface Science*, 6(3-4):309–355, 1980.

[40] B. Rothenhausler and W. Knoll. Surface-plasmon microscopy. *Nature*, 332(6165):615–617, 1988.

[41] P. B. Johnson and R. W. Christy. Optical constants of the noble metals. *Physical Review B*, 6:4370–4379, 1972.

[42] D. O. S. Melville and R. J. Blaikie. Super-resolution imaging through a planar silver layer. *Optics Express*, 13(6):2127–2134, 2005.

[43] N. Fang, H. Lee, C. Sun, and X. Zhang. Sub-diffraction-limited optical imaging with a silver superlens. *Science*, 308.

[44] R. H. Ritchie and H. B. Eldridge. Optical emission from irradiated foils .1. *Physical Review*, 126(6):1935–1947, 1962.

[45] E. N. Economou. Surface plasmons in thin films. *Physical Review*, 182(2):539–554, 1969.

[46] C. F. Bohren and D. R. Huffman. *Absorption and Scattering of Light by Small Particles*. John Wiley & Sons, Inc., 1983.

[47] J. Prikulis, P. Hanarp, L. Olofsson, D Sutherland, and M. Käll. Optical spectroscopy of nanometric holes in thin gold films. *Nano Letters*, 4(6):1003–1007, 2004.

[48] G. I. Stegeman, R. F. Wallis, and A. A. Maradudin. Excitation of surface-polaritons by end-fire coupling. *Optics Letters*, 8(7):386–388, 1983.

[49] R. Charbonneau, N. Lahoud, G. Mattiussi, and P. Berini. Demonstration of integrated optics elements based on long-ranging surface plasmon polaritons. *Optics Express*, 13(3):977–984.

[50] H. J. Lezec, A. Degiron, E. Devaux, R. A. Linke, L. Martin-Moreno, F. J. Garcia-Vidal, and T. W. Ebbesen. Beaming light from a subwavelength aperture. *Science*, 297(5582):820–822, 2002.

[51] J. M. Steele, C. E. Moran, A. Lee, C. M. Aguirre, and N. J. Halas. Metallodielectric gratings with subwavelength slots: Optical properties. *Physical Review B*, 68(20):Art. No. 205103, 2003.

[52] L. Lin, R. J. Blaikie, and R. J. Reeves. Surface-plasmon-enhanced optical transmission through planar metal films. *Physical Review B*, 74(15):Art. No. 155407, 2006.

[53] A. Christ, T. Zentgraf, S. G. Tikhodeev, N. A. Gippius, J. Kuhl, and H. Giessen. Controlling the interaction between localized and delocalized surface plasmon modes: Experiment and numerical calculations. *Physical Review B*, 74(15):Art. No. 155435, 2006.

[54] P. Berini. Plasmon-polariton waves guided by thin lossy metal films of finite width: Bound modes of symmetric structures. *Physical Review B*, 61(15):Art. No.10484, 2000.

[55] R. Charbonneau, P. Berini, E. Berolo, and E. Lisicka-Shrzek. Experimental observation of plasmon-polariton waves supported by a thin metal film of finite width. *Optics Letters*, 25(11):844–846.

[56] S. I. Bozhevolnyi, V. S. Volkov, E. Devaux, and T. W. Ebbesen. Channel plasmon-polariton guiding by subwavelength metal grooves. *Physical Review Letters*, 95(4):Art. No. 046802, 2005.

[57] J. R. Krenn and J. C. Weeber. Surface plasmon polaritons in metal stripes and wires. *Philosophical Transactions of the Royal Society of London Series A-Mathematical Physical and Engineering Sciences*, 362(1817):739–756, 2004.

[58] R. C. Reddick, R. J. Warmack, and T. L. Ferrell. New form of scanning optical microscopy. *Physical Review B*, 39(1):767–770, 1989.

[59] P. Dawson, F. Defornel, and J. P. Goudonnet. Imaging of surface-plasmon propagation and edge interaction using a photon scanning tunneling microscope. *Physical Review Letters*, 72(18):2927–2930, 1994.

[60] J. R. Krenn, A. Dereux, J. C. Weeber, E. Bourillot, Y. Lacroute, J. P. Goudonnet, G. Schider, W. Gotschy, A. Leitner, F. R. Aussenegg, and

C. Girard. Squeezing the optical near-field zone by plasmon coupling of metallic nanoparticles. *Physical Review Letters*, 82(12):2590–2593, 1999.

[61] S. I. Bozhevolnyi and V. Coello. Elastic scattering of surface plasmon polaritons: Modelling and experimenta. *Physical Review B*, 58(16):Art. No. 108999, 1998.

[62] J. C. Weeber, J. R. Krenn, A. Dereux, B. Lamprecht, Y. Lacroute, and J. P. Goudonnet. Near-field observation of surface plasmon polariton propagation on thin metal stripes. *Physical Review B*, 64(4):Art. No. 045411, 2001.

[63] M. L. Brongersma and P. G. Kik, editors. *Surface Plasmon Nanophotonics*, volume 131 of *Springer Series in Optical Science*.

[64] H. E. de Bruijn and J. Kooyman, R. P. H.and Greve. Determination of dielectric permittivity and thickness of a metal layer from a surface plasmon resonance experiment. *Applied Optics*, 29(13):1974–1978, 1990.

[65] K. Matsubara, S. Kawata, and S. Minami. Optical chemical sensor based on surface plasmon measurement. *Applied Optics*, 27(6):1160–1163, 1988.

[66] U. Jonsson, L. Fagerstam, B. Ivarsson, B. Johnsson, R. Karlsson, K. Lundh, S. Lofas, B. Persson, H. Roos, I. Ronnberg, S. Sjolander, E. Stenberg, R. Stahlberg, C. Urbaniczky, H. Ostlin, and M. Malmqvist. Real-time biospecific interaction analysis using surface-plasmon resonance and a sensor chip technology. *Biotechniques*, 11(5):620–627, 1991.

[67] C. Nylander, B. Liedberg, and T. Lind. Gas detection by means of surface plasmon resonance. *Sensors and Actuators*, 3:79–88, 1982.

[68] B. Liedberg, C. Nylander, and I. Lundström. Surface plasmon resonance gas detection and biosensing. *Sensors and Actuators*, 4:299–304, 1983.

[69] D. R. Shankaran, K. V. Gobi, and N. Miura. Recent advancements in surface plasmon resonance immunosensors for detection of small molecules of biomedical, food and environmental interest. *Sensors and Actuators B*, 121:158–177, 2007.

[70] A. Christ, T. Zentgraf, S. G. Tikhodeev, N. A. Gippius, J. Kuhl, and H. Giessen. Detection of immunocomplex formation via surface plasmon resonance on gold-coated diffraction gratings. *Biosensors*, 3:211–225, 1987.

[71] R. C. Jorgenson and S. S. Yee. A fiberoptic chemical sensor-based on surface-plasmon resonance. *Sensors and Actuators B*, 12(3):213–220, 1993.

[72] C. R. Lavers and J. S. Wilkinson. A wave-guide-coupled surface-plasmon sensor for an aqueous environment. *Sensors and Actuators B*, 22(1):75–81, 1994.

[73] www.biacore.com.

[74] C. L. Baird and D. G. Myszka. Current and emerging commercial optical biosensors. *Journal of Molecular Recognition*, 14:261–268, 2001.

[75] A. G. Brolo, R. Gordon, B. Leathem, and K. L. Kavanagh. Surface plasmon sensor based on the enhanced light transmission through arrays of nanoholes in gold films. *Langmuir*, 20(12):4813–4815, 2004.

[76] A. De Leebeeck, L. K. S. Kumar, V. de Lange, S. Sinton, R. Gordon, and A. G. Brolo. On-chip surface-based detection with nanohole arrays. *Analytical Chemistry*, 79(11):4094–4100, 2007.

[77] Y. S. Jung, Z. Sun, J. Wuenschell, H. K. Kim, P. Kaur, L. Wang, and D. Waldeck. High-sensitivity surface plasmon resonance spectroscopy based on a metal nanoslit array. *Applied Physics Letters*, 88(24):Art. No. 243105, 2006.

[78] M. D. Malinsky, K. L. Kelly, G. C. Schatz, and R. P. Van Duyne. Chain length dependence and sensing capabilities of the localized surface plasmon resonance of silver nanoparticles chemically modified with alkanethiol self-assembled monolayers. *Journal of the American Chemical Society*, 123(7):1471–1482, 2001.

[79] A. D. McFarland and R. P. Van Duyne. Single silver nanoparticles as real-time optical sensors with zeptomole sensitivity. *Nano Letters*, 3(8):1057–1062, 2003.

[80] T. Rindzevicius, Y. Alaverdyan, A. Dahlin, F. Hook, D. S. Sutherland, and M. Käll. Plasmonic sensing characteristics of single nanometric holes. *Nano Letters*, 5(11):2335–2339, 2005.

[81] M Fleischmann, P. J. Hendra, and A. J. Mcquilla. Raman-spectra of pyridine adsorbed at a silver electrode. *Chemical Physics Letters*, 26(2):163–166, 1974.

[82] A. M. Glass, P. F. Liao, J. G. Bergman, and D. H. Olson. Interaction of metal particles with absorbed dye molecules - absorption and luminescence. *Optics Letters*, 5(9):368–370, 1980.

[83] D. A. Weitz, S. Garoff, J. I. Gersten, and A. Nitzan. The enhancement of raman-scattering, resonance raman-scattering, and fluorescence from molecules adsorbed on a rough silver surface. *Journal of Chemical Physics*, 78(9):5324–5338, 1983.

[84] K. Kneipp, H. Kneipp, and J. Kneipp. Surface-enhanced raman scattering in local optical fields of silver and gold nanoaggregatess - from single-molecule raman spectroscopy to ultrasensitive probing in live cells. *Accounts of Chemical Research*, 39(7):443–450, 2006.

[85] K. Aslan, I. Gryczynski, J. Malicka, E. Matveeva, J. R. Lakowicz, and C. D. Geddes. Metal-enhanced fluorescence: an emerging tool in biotechnology. *Current Opinion in Biotechnology*, 16(1):55–62, 2005.

[86] Y. X. Zhang, K. Aslan, S. N. Malyn, and C. D. Geddes. Metal-enhanced phosphorescence (mep). *Chemical Physics Letters*, 427(4-6):432–437, 2006.

[87] M. Ohtsu and K. Kobayashi. *Optical near fields : introduction to classical and quantum theories of electromagnetic phenomena at the nanoscale*. Springer-Verlag Berlin Heidelberg New York, 2004.

[88] J. Takahara, S. Yamagishi, H. Taki, A. Morimoto, and T. Kobayashi. Guiding of a one-dimensional optical beam with nanometer diameter. *Optics Letters*, 22(7):475–477, 1997.

[89] P. Berini, R. Charbonneau, N. Lahoud, and G. Mattiussi. Characterization of long-range surface-plasmon-polariton waveguides. *Journal of Applied Physics*, 98(4):Art. No. 043109, 2005.

[90] T. Yatsui, M. Kourogi, and M. Ohtsu. Plasmon waveguide for optical far/near-field conversion. *Applied Physics Letters*, 79(27):4583–4585, 2001.

[91] D. F. P. Pile, T. Ogawa, D. K. Gramotnev, T. Okamoto, M. Haraguchi, M. Fukui, and S. Matsuo. Theoretical and experimental investigation of strongly localized plasmons on triangular metal wedges for subwavelength waveguiding. *Applied Physics Letters*, 87(6):Art. No. 061106, 2005.

[92] D. F. P. Pile, T. Ogawa, D. K. Gramotnev, Y. Matsuzaki, K. C. Vernon, K. Yamaguchi, T. Okamoto, M. Haraguchi, and M. Fukui. Two-dimensionally localized modes of a nanoscale gap plasmon waveguide. *Applied Physics Letters*, 87(26):Art. No. 261114, 2005.

[93] L. Chen, J. Shakya, and M. Lipson. Subwavelength confinement in an integrated metal slot waveguide on silicon. *Optics Letters*, 31(14):2133–2135, 2006.

[94] R. Charbonneau, C. Scales, I. Breukelaar, S. Fafard, N. Lahoud, G. Mattiussi, and P. Berini. Passive integrated optics elements based on long-ranging surface plasmon polaritons. *Journal of Lightwave Technology*, 24(1):477–494.

[95] M. Quinten, A. Leitner, J. R. Krenn, and Aussenegg. Electromagnetic energy transport via linear chains of silver nanoparticels. *Optics Letters*, 23(17):1331–1333, 1998.

[96] S. A. Maier, P. G. Kik, H. A. Atwater, S. Meltzer, E. Harel, B. E. Koel, and A. A. G. Requicha. Local detection of electromagnetic energy transport below the diffraction limit in metal nanoparticle plasmon waveguides. *Nature Materials*, 2(4):229–232, 2003.

[97] I. I. Smolyaninov, D. L. Mazzoni, J. Mait, and C. C. Davis. Experimental study of surface-plasmon scattering by individual surface defects. *Physical Review B*, 56(3):1601–1611, 1997.

[98] W. Nomura, M. Ohtsu, and T. Yatsui. Nanodot coupler with a surface plasmon polariton condenser for optical far/near-field conversion. *Applied Physics Letters*, 86(18):Art. No. 181108, 2005.

[99] L. L. Yin, V. K. Vlasko-Vlasov, J. Pearson, J. M. Hiller, J. Hua, U. Welp, D. E. Brown, and C. W. Kimball. Subwavelength focusing and guiding of surface plasmons. *Nano Letters*, 5(7):1399–1402, 2005.

[100] T. Nikolajsen, K. Leosson, and S. I. Bozhevolnyi. Surface plasmon polariton based modulators and switches operating at telecom wavelengths. *Applied Physics Letters*, 85(24):5833–5835, 2004.

[101] G. Gagnon, N. Lahoud, G. A. Mattiussi, and P. Berini. Thermally activated variable attenuation of long-range surface plasmon-polariton waves. *Journal of Lightwave Technology*, 24(11):4391–4402, 2006.

[102] A. V. Krasavin, A. V. Zayats, and N. I. Zheludev. Active control of surface plasmon-polariton waves. *Journal of Optics A-Pure and Applied Optics*, 7(2):85–89, 2005.

[103] H. F. Ghaemi, T. Thio, D. E. Grupp, T. W. Ebbesen, and H. J. Lezec. Surface plasmons enhance optical transmission through subwavelength holes. *Physical Review B*, 58(11):6779–6782, 1998.

[104] H. A. Bethe. Theory of diffraction by small holes. *Physical Review*, 66(7 and 8):163–182, 1944.

[105] D. E. Grupp, H. J. Lezec, T. W. Ebbesen, K. M. Pellerin, and T. Thio. Crucial role of metal surface in enhanced transmission through subwavelength apertures. *Applied Physics Letters*, 77(11):1569–1571, 2000.

[106] T. Thio, K. M. Pellerin, R. A. Linke, H. J. Lezec, and T. W. Ebbesen. Enhanced light transmission through a single subwavelength aperture. *Optics Letters*, 26(24):1972–1974, 2001.

[107] F. J. Garcia-Vidal, J. Sanchez-Dehesa, A. Dechelette, E. Bustarret, T. Lopez-Rios, T. Fournier, and B. Pannetier. Localized surface plasmons in lamellar metallic gratings. *Journal of Lightwave Technology*, 17(11):2191–2195, 1999.

[108] I. Avrutsky, Y. Zhao, and V. Kochergin. Surface-plasmon-assisted resonant tunneling of light through a periodically corrugated thin metal film. *Optics Letters*, 25(9):595–597, 2000.

[109] U. Schröter and D. Heitmann. Surface-plasmon-enhanced transmission through metallic gratings. *Physical Review B*, 58(23):15419–15421, 1998.

[110] J. A. Porto, F. J. Garcia-Vidal, and J. B. Pendry. Transmission resonances on metallic gratings with very narrow slits. *Physical Review Letters*, 83(14):2845–2848, 1999.

[111] S. Astilean, P. Lalanne, and M. Palamaru. Light transmission through metallic channels much smaller than the wavelength. *Optics Communications*, 175:265–273, 2000.

[112] Q. Cao and P. Lalanne. Negative role of surface plasmons in the transmission of metallic gratings with very narrow slits. *Physical Review Letters*, 88(5):Art. No. 057403, 2002.

[113] D. C. Skigin and R. A. Depine. Transmission resonance of metallic conpound grating with subwavelength slits. *Physical Review Letters*, 95(21):Art. No. 217402, 2005.

[114] A. Christ, S. G. Tikhodeev, N. A. Gippius, J. Kuhl, and H. Giessen. Waveguide-plasmon polaritons: strong coupling of photonic and electronic resonances in a metallic photonic crystal slab. *Physical Review Letters*, 91(18):Art. No. 183901, 2003.

[115] F. Marquier, J. J. Greffet, S. Collin, F. Pardo, and J. L. Pelouard. Resonant transmission through a metallic film due to coupled modes. *Optics Express*, 13(1):70–76, 2004.

[116] E. Popov, M. Nevière, S. Enoch, and R. Reinisch. Theory of light transmission through subwavelength periodic hole arrays. *Physical Review B*, 62(23):16100–16108, 2000.

[117] W. L. Barnes, W. A. Murray, J. Dintinger, E. Devaux, and T. W. Ebbesen. Surface plasmon polaritons and their role in the enhanced transmission of light through periodic arrays of subwavelength holes in a metal film. *Physical Review Letters*, 92(10):Art. No. 107401, 2004.

[118] M. M. J. Treacy. Dynamical diffraction explanation of the anomalous transmission of light through metallic gratings. *Physical Review B*, 66(19):Art. No. 195105, 2002.

[119] H. J. Lezec and T. Thio. Diffracted evanescent wave model for enhanced and suppressed optical transmission through subwavelength hole arrays. *Optics Express*, 12(16):3629–3651, 2004.

[120] W. C. Tan, T. W. Preist, and R. J. Sambles. Resonant tunneling of light through thin metal films via strongly localized surface plasmons. *Physical Review B*, 62(16):11134–11138, 2000.

[121] L. Salomon, F. D. Grillot, A. V. Zayats, and F. de Fornel. Near-field distribution of optical transmission of periodic subwavelength holes in a metal film. *Physical Review Letters*, 86(6):1110–1113, 2001.

[122] L. Martin-Moreno, F. J. Garcia-Vidal, H. J. Lezec, K. M. Pellerin, T. Thio, J. B. Pendry, and T. W. Ebbesen. Theory of extraordinary optical transmission through subwavelength hole arrays. *Physical Review Letters*, 86(6):1114–1117, 2001.

[123] S. A. Darmanyan and A.V. Zayats. Light tunneling via resonant surface plasmon polariton states and the enhanced transmission of periodically nanostructured metal films: An analytical study. *Physical Review B*, 67(3):Art. No. 035424, 2003.

[124] N Bonod, S. Enoch, L. F. Li, E. Popov, and M. Neviere. Resonant optical transmission through thin metallic films with and without holes. *Optics Express*, 11(5):482–490, 2003.

[125] D. Gerard, L. Salomon, F. de Fornel, and A. V. Zayats. Ridge-enhanced optical transmission through a continuous metal film. *Physical Review B*, 69(11):Art. No. 113405, 2004.

[126] R. Gordon, A. G. Brolo, A. McKinnon, A. Rajora, B. Leathem, and K. L. Kavanagh. Strong polarization in the optical transmission

through elliptical nanohole arrays. *Physical Review Letters*, 92(3):Art. No. 037401, 2004.

[127] K. L. Klein Koerkamp, S. Enoch, F. B. Segerink, N. F. van Hulst, and Kuipers. Strong influence of hole shape on extraordinary transmission through periodic arrays of subwavelength holes. *Physical Review Letters*, 92(18):Art. No. 183901, 2004.

[128] A. Degiron and T. W. Ebbesen. The role of localized surface plasmon modes in the enhanced transmission of periodic subwavelength apertures. *Journal of Optics A: Pure and Applied Optics*, 7:90–96, 2005.

[129] K. L. van der Molen, K. L. Klein Koerkamp, S. Enoch, F. B. Segerink, N. F. van Hulst, and Kuipers. Role of shape and localized resonance in extraordinary transmission through periodic arrays of subwavelength holes: Experiment and theory. *Physical Review B*, 72(4):Art. No. 045421, 2005.

[130] R. Gordon and A. G. Brolo. Increased cut-off wavelength for a subwavelength hole in a real metal. *Optics Express*, 13(6):1933–1938, 2005.

[131] J. Cesario, R. Quidant, G. Badenes, and S. Enoch. Electromagnetic coupling between a metal nanoparticle grating and a metallic surface. *Optics Letters*, 30(24):3404–3406.

[132] G. Lévêque and O. J. F. Martin. Optical interactions in a plasmonic particle coupled to a metallic film. *Optics Express*, 14(21):9971–9981, 2006.

[133] L. Lin, R. J. Reeves, and R. J. Blaikie. Surface-plasmon-enhanced light transmission through planar metallic films. *Journal of Electromagnetic Waves and Applications*, 19(13):1721–1728, 2005.

[134] J. Gómez Rivas, C. Schotsch, P. Haring Bolivar, and H. Kurz. Enhanced transmission of thz radiation through subwavelength holes. *Physical Review B*, 21(20):Art. No. 201306, 2003.

[135] M. J. Lockyear, A. P. Hibbins, J. R. Sambles, and C. R. Lawrence. Surface-topography-induced enhanced transmission and directivity of microwave radiation through a subwavelength circular metal aperture. *Applied Physics Letters*, 84(12):2040–2042, 2004.

[136] D. K. Gifford and D. G. Hall. Extraordinary transmission of organic photoluminescence through an otherwise opaque metal layer via surface plasmon cross coupling. *Applied Physics Letters*, 80(20):3679–3681, 2002.

[137] S. Wedge and W. L. Barnes. Surface plasmon-polariton mediated light emission through thin metal films. *Optics Express*, 12(16):3673–3685, 2004.

[138] C. Liu, V. Kamaev, and Z. V. Vardeny. Efficiency enhancement of an organic light-emitting diode with a cathode forming two-dimensional periodic hole array. *Applied Physics Letters*, 86(14):Art. No. 143501, 2005.

[139] W. Srituravanich, N. Fang, C. Sun, Q. Luo, and X. Zhang. Plasmonic nanolithography. *Nano Letters*, 4(6):1085–1088, 2004.

[140] D. B. Shao and S. C. Chen. Surface-plasmon-assisted nanoscale photolithography by polarized light. *Applied Physics Letters*, 86(25):Art. No. 253107, 2005.

[141] E. Altewischer, M. P. van Exter, and J. P. Woerdman. Plasmon-assisted transmission of entangled photons. *Nature*, 418(6895):304–306, 2002.

[142] S. Fasel, F. Robin, E. Moreno, D. Emi, N. Gisin, and H. Zbinden. Energy-time entanglement preservation in plasmon-assisted light transmission. *Physical Review Letters*, 94(11):Art. No. 110501, 2005.

[143] E. Moreno, A. I. Fernandez-Dominguez, J. I. Cirac, F. J. Garcia-Vidal, and L. Martin-Moreno. Resonant transmission of cold atoms through subwavelength apertures. *Physical Review Letters*, 95(17):Art. No. 170406, 2005.

[144] A. Fernandez, J. Y. Decker, S. M. Herman, D. W. Phillion, D. W. Sweeney, and M. D. Perry. Methods for fabricating arrays of holes using interference lithography. *Journal of Vacuum Science & Technology B: Microelectronics Processing and Phenomena*, 15(6):2439, 1997.

[145] X. Ao and S. He. Three-dimensional photonic crystal of negative refraction achieved by interference lithography. *Optics Letters*, 29(21):2542–2544, 2004.

[146] S. J. Drake. Design of an interference lithography system. Master's thesis, The University of Canterbury, 2005.

[147] M. G. Moharam, E. B. Gran, D. A. Pommet, and T. K. Gaylord. Formulation for stable and efficient implementation of the riourous

coupled-wave analysis of binary gratings. *Journal of the Optical Society of America A*, 12(5):1068–1076, 1995.

[148] www.gsolver.com.

[149] E. G. Loewen and E. Popov. *Diffraction Gratings and Applications*. Marcel Dekker, Inc., 1997.

[150] L. Li and C. W. Haggans. Convergence of the coupled-wave method for metallic lamellar diffraction gratings. *Journal of the Optical Society of America A*, 10(6):1184–1189, 1993.

[151] P. Lalanne and G. M. Morris. Highly improved convergence of the coupled-wave method for tm polarization. *Journal of the Optical Society of America A*, 13(4):779–784, 1996.

[152] A. Giannattasio, I. R. Hooper, and W. L. Barnes. Transmission of light through thin silver films via surface plasmon-polaritons. *Optics Express*, 12(24):5881–5886, 2004.

[153] S. Ahmed. Finite-element method for waveguide problems. *Electronics Letters*, 4(18):387, 1968.

[154] www.comsol.com.

[155] L. Lin and R. J. Blaikie. Negative permeability using planar-patterned metallic multilayer structures. *Journal of Optics A: Pure and Applied Optics*, 9:385–388, 2007.

[156] V. G. Veselago. Electrodynamics of substances with simultaneously negative values of ε and μ. *Soviet Physics Uspekhi-Ussr*, 10(4):509–514, 1968.

[157] J. B. Pendry, A. J. Holden, D. J. Robbins, and W. J. Stewart. Low-frequency plasmons in thin wire structures. *Journal of Physics: Condensed Matter*, 10:4785–4809, 1998.

[158] J. B. Pendry, A. J. Holden, D. J. Robbins, and W. J. Stewart. Magnetism from conductors and enhanced nonlinear phenomena. *IEEE Transactions on Microwave Theory and Techniques*, 47(11):2075–2084, 1999.

[159] A. Shelby, D. R. Smith, and S. Schultz. Experimental verification of a negative index of refraction. *Science*, 292(5514):77–79, 2001.

[160] N. Engheta and R. W Ziolkowski. A positive future for double-negative metamaterials. *IEEE Transactions on Microwave Theory and Techniques*, 53(4):1535–1556, 2005.

[161] A. J. Holden. Towards some real applications for negative materials. *Photonics and Nanostructures Fundamentals and Applications*, 3:96–99, 2005.

[162] P. F. Loschialpo, D. W. Forester, D. L. Smith, F. J. Rachford, and C. Monzon. Optical properties of an ideal homogeneous causal left-handed material slab. *Physical Review E*, 70(3):Art. No. 036605, 2004.

[163] J. B. Pendry, D. Schurig, and D. R. Smith. Controlling electromagnetic fields. *Science*, 312(5781):1780–1782, 2006.

[164] W. S. Cai, U. K. Chettiar, A. V. Kildishev, and V. M. Shalaev. Optical cloaking with metamaterials. *Nature Photonics*, 1(4):224–227, 2007.

[165] C. Luo, S. G. Johnson, J. D. Joannopoulos, and J. B. Pendry. All-angle negative refraction without negative index. *Physical Review B*, 65(20):Art. No. 201104, 2002.

[166] E. Cubukcu, K. Aydin, E. Ozbay, S. Foteinopolou, and C. M. Soukoulis. Electromagnetic waves: Negative refraction by photonic crystals. *Nature*, 423(6940):604–605, 2003.

[167] W. E. Kock. Metallic delay lenses. *Bell System Technical Journal*, 27(1):58–82, 1948.

[168] W. M. Sharpless. Artificial dielectrics for microwaves. *Proceedings of the Institute of Radio Engineers*, 39(11):1389–1393, 1951.

[169] R. W. Corkum. Isotropic artificial dielectric. *Proceedings of the Institute of Radio Engineers*, 40(5):574–587, 1952.

[170] J. Brown. Artificial dielectrics having refractive indices less than unity. *Proceedings of the Institution of Electrical Engineers-London*, 100(5):51–62, 1953.

[171] K. E. Golden. Plasma simulation with an artificial dielectric in a horn geometry. *IEEE Transactions on Antennas and Propagation*, 13(4):587–594, 1965.

[172] L. D. Landau, E. M. Lifshitz, and L. P. Pitaevskii. *Electrodynamics of continuous media*. Butterworth-Heinenann, Oxford, England, 2nd edition, 1984.

[173] D. J. Bergman and D. Stroud. Physical properties of macroscopically inhomogeneous media. *Solid State Physics*, 46:147–269, 1992.

[174] S. A. Ramakrishna. Physics of negative refractive index materials. *Physical Review B*, 68(2):449–521, 2005.

[175] D. R. Smith and J. B. Pendry. Homogenization of metamaterials by field averaging (invited paper). *Journal of the Optical Society of America B*, 23.

[176] Acher. O., J. M. Lerat, and F. Duverger. Fresnel coefficients at an interface with a lamellar composite material. *Physical Review B*, 62(20):Art. No. 13748, 2000.

[177] Acher. O., J. M. Lerat, and N. Mallejac. Evaluation and illustration of the properties of metamaterials using field summation. *Optics Express*, 15(3):1096–1106, 2007.

[178] D. R. Smith, S. Schultz, P. Markoš, and C. M. Soukoulis. Determination of effective permittivity and permeability of metamaterials from reflection and transmission coefficients. *Physical Review B*, 65(19):Art. No. 195104, 2002.

[179] D. R. Smith, D. C. Vier, Th. Koschny, and C. M. Soukoulis. Electromagnetic parameter retrieval from inhomogeneous metamaterials. *Physical Review E*, 71(3):Art. No. 036617, 2005.

[180] W. B. Weir. Automatic measurement of complex dielectric-constant and permeability at microwave-frequencies. *Proceedings of The IEEE*, 62(1):33–36, 1974.

[181] D. M. Pozar. *Microwave engineering*. Hoboken, NJ : J. Wiley, 3rd edition, 2005.

[182] X. Chen, T. M. Grzegorczyk, B. I. Wu, J. Pacheco, Jr., and J. A. Kong. Robust method to retrieve the constitutive effective parameters of metamaterials. *Physical Review E*, 70(1):Art. No. 016608, 2004.

[183] S. Zhang, W. Fan, N. C. Panoiu, K. J. Malloy, R. M. Osgood, and S. R. J. Brueck. Experimental demonstration of near-infrared negative-index metamaterials. *Physical Review Letters*, 95(13):Art. No. 137404, 2005.

[184] V. M. Shalaev, W. Cai, U. K. Chettiar, H. Yuan, A. K. Sarychev, V. P. Drachev, and A. V. Kildishev. Negative index of refraction in optical metamaterials. *Optics Letters*, 30(24):3356–3358, 2005.

[185] D. Seetharamdoo, R. Sauleau, K. Mahdjoubi, and A.-C. Tarot. Effective parameters of resonant negative refractive index metamaterials: Interpretation and validity. *Journal of Applied Physics*, 98(6):063505, 2005.

[186] A. V. Kildishev, W. Cai, U. K. Chettiar, H. K. Yuan, A. K. Sarychev, V. P. Drachev, and V. M. Shalaev. Negative refractive index in optics of metaldielectric composites. *Journal of the Optical Society of America B*, 23.

[187] J. D. Jackson. *Classical Electrodynamics*. Singapore:Wiley, 1999.

[188] S. O'Brien and J. B. Pendry. Magnetic activity at infrared frequencies in structured metallic photonic crystals. *Journal of Physics: Condensed Matter*, 14:63836394, 2002.

[189] P. Markoš and C. M. Soukoulis. Transmission properties and effective electromagnetic parameters of double negative metamaterials. *Optics Express*, 11(7):649–661, 2003.

[190] T. Koschny, P. Markoš, D. R. Smith, and C. M. Soukoulis. Resonant and antiresonant frequency dependence of the efective parameters of metamaterials. *Physical Review E*, 68(6):Art. No. 065602, 2003.

[191] R. A. Depine and A. Lakhtakia. Common i on "resonant and antiresonant frequency dependence of the efective parameters of metamaterials". *Physical Review E*, 70(4):Art. No. 048601, 2004.

[192] A. L. Efros. Common ii on "resonant and antiresonant frequency dependence of the efective parameters of metamaterials". *Physical Review E*, 70(4):Art. No. 048602, 2004.

[193] T. Koschny, P. Markoš, E. N. Economou, D. R. Smith, D. C. Vier, and C. M. Soukoulis. Impact of inherent periodic structure on effective medium description of left-handed and related metamaterials. *Physical Review B*, 71(24):Art. No. 245105, 2005.

[194] R. A. Depine and A. Lakhtakia. A new condition to identify isotropic dielectric-magnetic materials displaying negative phase velocity. *Microwave and Optical Technology Letters*, 41(4):315–316, 2004.

[195] J. Zhou, T. Koschny, L. Zhang, G. Tuttle, and C. M. Soukoulis. Experimental demonstration of negative index of refraction. *Applied Physics Letters*, 88(22):221103, 2006.

[196] U. K. Chettiar, A. V. Kildishev, H. K. Yuan, W. Cai, S. Xiao, V. P. Drachev, and V. M. Shalaev. Dual-band negative index metamaterial: double negative at 813 nm and single negative at 772 nm. *Optics Letters*, 32(12):1671–1673, 2007.

[197] S. Linden, C. Enkrich, G. Dolling, M. W. Klein, J. Zhou, T. Koschny, C. M. Soukoulis, S. Burger, Frank F. Schmidt, and M. Wegener. Photonic metamaterials: Magnetism at optical frequencies. *IEEE Journal of Selected Topics in Quantum Electronics*, 12(6):1097–1105, 2006.

[198] T. J. Yen, W. J. Padilla, N. Fang, D. C. Vier, D. R. Smith, J. B. Pendry, D. N. Basov, and X. Zhang. Terahertz magnetic response from artificial materials. *Science*, 303:1494–1496, 2004.

[199] S. Linden, C. Enkrich, M. Wegener, J. Zhou, T. Koschny, and C. M. Soukoulis. Magnetic response of metamaterials: at 100 terahertz. *Science*, 306:1351–1353, 2004.

[200] G. Dolling, C. Enkrich, M. Wegener, J. F. Zhou, C. M. Soukoulis, and S. Linden. Cut-wire pairs and plate pairs as magnetic atoms for optical metamaterials. *Optics Letters*, 30(23):3198–3200, 2005.

[201] J. Zhou, Th. Koschny, M. Kafesaki, E. N. Economou, J. B. Pendry, and C. M. Soukoulis. Saturation of the magnetic response of split-ring resonators at optical frequencies. *Physical Review Letters*, 95(22):Art. No. 223902, 2005.

[202] M. W. Klein, C. Enkrich, M. Wegener, C. M. Soukoulis, and S. Linden. Single-slit split-ring resonators at optical frequencies: limits of size scaling. *Optics Letters*, 31(9):1259–1261, 2006.

[203] V. A. Podolskiy, A. K. Sarychev, and V. M. Shalaev. Plasmon modes in metal nanowires and left-handed materials. *Journal of Nonlinear Optical Physics & Materials*, 11(1):65–74, 2002.

[204] V. A. Podolskiy, A. K. Sarychev, and V. M. Shalaev. Plasmon modes and negative refraction in metal nanowire composites. *Optics Express*, 11(7):735–745, 2003.

[205] T. A. Klar, V. Kildishev, V. P. Drachev, and V. M. Shalaec. Negative-index metamaterials: Going optical. *IEEE Transactions of Selected Topics in Quantum Electronics*, 12(6):1106–1115, 2006.

[206] S. Zhang, W. Fan, K. J. Malloy, S. R. J. Brueck, N. C. Panoiu, and R. M. Osgood. Near-infrared double negative metamaterials. *Optics Express*, 13:4922–4930, 2005.

[207] G. Dolling, C. Enkrich, M. Wegener, C. M. Soukoulis, and S. Linden. Low-loss negative-index metamaterial at telecommunication wavelengths. *Optics Letters*, 31(12):1800–1802, 2005.

[208] G. Dolling, M. Wegener, C. M. Soukoulis, and S. Linden. Negative-index metamaterial at 780 nm wavelength. *Optics Letters*, 32(1):53–55, 2006.

[209] A. N. Grigorenko, A. K. Geim, H. F. Gleeson, Y. Zhang, A. A. Firsov, I. Y. Khrushchev, and J. Petrovic. Nanofabricated media with negative permeability at visible frequencies. *Nature*, 438(7066):335–338, 2005.

[210] A. N. Grigorenko. Negative refractive index in artificial metamaterials. *Optics Letters*, 31(16):2483–2485, 2006.

[211] A. V. Kildishev, V. P. Drachev, U. K. Chettiar, V. M. Shalaev, D. H. Werner, and D. H. Kwon. Comment on "negative refractive index in artificial metamaterials". *Optics Letters*, 32(11):1510–1511, 2007.

[212] S. Zhang, W. Fan, B. K. Minhas, A. Frauenglass, K. J. Malloy, and S. R. J. Brueck. Midinfrared resonant magnetic nanostructures exhibiting a negative permeability. *Physical Review Letters*, 94(3):Art. No. 037402, 2005.

[213] G. Shvets and Y. A. Urzhumov. Engineering the electromagnetic properties of periodic nanostructures using electrostatic resonances. *Physical Review Letters*, 93(24):Art. No. 243902, 2004.

[214] G. Shvets and Y. A. Urzhumov. Electric and magnetic properties of sub-wavelength plasmonic crystals. *Journal of Optics A - Pure and Applied Optics*, 7:23–31, 2005.

[215] G. Shvets and Y. A. Urzhumov. Negative index meta-materials based on two-dimensional metallic structures. *Journal of Optics A - Pure and Applied Optics*, 8:122–130, 2006.

[216] A. K. Sarychev, G. Shvets, and V. M. Shalaev. Magnetic plasmon resonance. *Physical Review E*, 73(3):Art. No. 036609, 2006.

[217] A. Alu, A. Salandrino, and N. Engheta. Negative effective permeability and left-handed materials at optical frequencies. *Optics Express*, 14(4):1557–1567, 2006.

[218] Mitchell J. S. Lin L. Sedoglavich N. Sharpe, J. C. and R. J. Blaikie. Gold nanohole array substrates as immunobiosensors. *Analytical Chemistry*, (Accepted for publication), 2008.